A Comparative study of nickel molybdate and carbon nanotube supported nickel molybdate catalysts for the oxidative dehydrogenation of *n*-octane

by

SHANTAL SEWSUNKER

BSC (HONS)

Submitted in fulfilment of the academic requirements for the degree of Master of Science in the School of Chemistry, University of KwaZulu-Natal, Durban

June 2011

As the candidate's supervisor I have approved this dissertation for submission.

Name: H.B. Friedrich Signed: _____ Date: ____

Abstract

A comparative study of the activation of *n*-octane over nickel molybdate (α and β-phases), carbon nanotubes and carbon nanotube supported nickel molybdate was carried out in the gas phase in a plug flow fixed bed reactor having air as the oxidant. All four catalysts were found to be catalytically active in the oxidative dehydrogenation reaction. It was found that the higher temperature β-phase molybdate is catalytically more active and selective than the α-phase for the production of valuable oxygenates and C_8 olefins at isoconversion and under isothermal conditions. Carbon nanotubes were found to be catalytically active with a higher selectivity to oxygenates and C_8 olefins and a lower selectivity to COx as compared to α-$NiMoO_4$. Carbon nanotube supported α-nickel molybdate showed a decrease in selectivity to CO_2 as compared to the α-$NiMoO_4$ catalysts alone and yielded the highest selectivity to the total C_8 olefins.

Preface

The experimental work described in this dissertation was carried out in the School of Chemistry, University of KwaZulu-Natal, Durban, from May 2009 to June 2011, under the supervision of Professor Holger B. Friedrich.

These studies represent original work by the author and have not otherwise been submitted in any form for any degree or diploma to any tertiary institution. Where use has been made of the work of others it is duly acknowledged in the text.

Declaration 1 - Plagiarism

I, Shantal Sewsunker declare that

1. The research reported in this thesis, except where otherwise indicated, is my original research.

2. This thesis has not been submitted for any degree or examination at any other university.

3. This thesis does not contain other persons' data, pictures, graphs or other information, unless specifically acknowledged as being sourced from other persons.

4. This thesis does not contain other persons' writing, unless specifically acknowledged as being sourced from other researchers. Where other written sources have been quoted, then:
   a. Their words have been re-written but the general information attributed to them has been referenced
   b. Where their exact words have been used, then their writing has been placed in italics and inside quotation marks, and referenced.

5. This thesis does not contain text, graphics or tables copied and pasted from the Internet, unless specifically acknowledged, and the source being detailed in the thesis and in the References sections.

Signed: ……

Declaration 2 – Conference Contributions

Part of the work reflected in this dissertation has been presented at the following conferences:

CATSA Conference 2009, Cape Town, Poster presentation, *Synthesis and characterisation of nickel molybdate and vanadium magnesium oxide catalysts*

CATSA Conference 2010, Bloemfontein, Oral Presentation, *Synthesis and characterisation of nickel molybdate and carbon nanotube supported nickel molybdate catalysts for the ODH of n-octane*

List of Figures

List of Schemes

List of Tables

Acknowledgements

I would like to express my sincere gratitude to everyone who contributed in any way towards the successful completion of this project. A special mention to the following:

To my Supervisor, Prof Holger B. Friedrich who has risen above and beyond the role of an academic, for being a vast well of knowledge, wisdom, inspiration and constant motivation, I thank you. I am forever grateful and indebted to you.

I would like to thank Dr Frans Prinsloo and Dr Jonathan Chetty of Sasol technology R&D. Thank you to Dr Prinsloo for his mentorship and supplying of the carbon nanotubes and Dr Chetty for his mentorship and encouragement.

I thank Sasol, NRF and Thrip for funding this project.

Thank you to Dr James Wesley-Smith, Miss Sharon Eggars and Mrs Priscilla Maartens from the Electron Microscope Unit for assistance with TEM and SEM. I thank Dr Vincent Nyamori for his advice and expertise shared on the science of carbon nanotubes.

Thank you to Mrs Vashti Reddy and Mr Gregory Moodley for their assistance with lab glassware and chemicals. I would like to thank Mrs Jay Govender, for the efficient processing of orders. Thank you to Verlan Govender of Swagelok for the efficient and friendly service.

I thank my friends at the Catalysis Research Group of UKZN especially, Mzamo. A special thank you to my dear friend Dr Nicolas Grosjean, for always being there in times of need. Thank you Nico for your intelligence, skilfulness and patience and most of all your friendship which has meant the world to me.

I would like to express my gratitude to my parents for allowing me the opportunity of good solid education which I can be proud of. My eternal gratitude to my grandparents for instilling in me wisdom, good values and work ethic and constant motivation, against all odds, to know that nothing is unattainable. To my little brother Rahul, thank you for being such a funny young man and most of all a good brother.

Lastly and most importantly to my fiancé Craig Martin who has been with me through the best and worst of times. For the late nights which you accompanied me at the lab often fighting the signs of fatigue, the sacrifices you made to ensure that my work was always put first, never once complaining. You have always been my source of strength and light and the reason that I will never give up. For everything that you bring to my life the words ‘thank you’ will never do justice. I love you, always.

Dedication

For my Aja, who is with me always...

Abbreviations

ODH	Oxidative dehydrogenation
DTA	Differential thermal analysis
XRD	X-ray diffraction
ESR	Electron spin resonance
XPS	X-ray photoelectron spectroscopy
CNTs	Carbon nanotubes
SWCNTs	Single walled carbon nanotubes
MWCNT	Multi walled carbon nanotubes
CNF	Carbon nanofibers
f-CNT	Functionalised carbon nanotubes
SEM	Scanning electron microscopy
EDX	Electron dispersive x-rays
TEM	Transmission electron microscopy
HR-TEM	High resolution transmission electron microscopy
TGA-DSC	Thermogravimetric analysis differential scanning calorimetry
UN-vis-NIR	Ultra violet - visible - near infra red spectroscopy
IR	Infra red spectroscopy
CVD	Chemical vapour deposition
ODE	Oxidative dehydrogenation of ethylbenzene
HDP	Homogeneous deposition precipitation
NM	Nickel molybdate
NM-A	α-nickel molybdate Ni:Mo = 1
NM-B	Nickel molybdate Ni:Mo < 1

NM-C	Nickel molybdate Ni:Mo > 1
NM-CNT	Carbon nanotube supported nickel molybdate
ICP-OES	Inductively Coupled Plasma - Optical Emission Spectroscopy
ATR-IR	Attenuated Total Reflectance Infrared Spectroscopy
BET	Brunauer-Emmett-Teller
TPR	Temperature Programmed Reduction
HPLC	High performance liquid chromatography
GC	Gas Chromatograph
GC-FID	Gas Chromatograph - Flame Ionisation Detector
GC-TCD	Gas Chromatograph – Thermal Conductivity Detector
id	Internal diameter
GHSV	Gas hourly space velocity
SAED	Selected area electron diffraction
% X	% Conversion
Temp	Temperature
RRF	Relative response factors

Contents

Chapter 1 - Background to study

1.1 Heterogeneous catalytic activation of paraffins

Selective catalytic oxidation of hydrocarbons contributes significantly to the gross national product of countries with a strong industrial chemistry sector and provides opportunities for growth in emerging countries. Organic chemicals such as olefins, aromatics and oxygenates make up the feedstocks in industrial processes of significance such as the production of polymers and bulk chemicals [1]. Olefins which are principally sourced via the steam cracking of naphtha and fluidised catalytic cracking in oil refining are fast becoming insufficient to meet the demand. There is a significant drive to source these chemicals by alternative means, and also towards the direct use of alkanes which are more economical than the corresponding olefins. With the increasing number of plants worldwide using gas to liquid technology, the demand for these chemicals is expected to rise considerably in the near future. This places an increased importance and requirement on paraffin activation for the production of fine chemical intermediates [2].

Due to the relative inactivity of paraffins, their selective oxidation is complex and control of product selectivity is difficult to achieve. The stability of the C-H bond coupled with the relatively low paraffin activity means that the energy requirements for activation are high and the process calls for high pressures and temperatures. These operating conditions lead to free radical formation and therefore inadequate control of product selectivity. One of the major problems faced with selective oxidation of paraffins is the higher reactivity of the partial oxidation products than that of the reactant itself. This makes it difficult to stop the reaction at the desired product and prevent its further non selective activation under the conditions at which the reactant is activated [2]. Another way in which product selectivity is reduced is at high temperatures, which drive total combustion resulting in the formation of CO, CO_2 and H_2O. The need for a selectively active catalyst for paraffin activation is apparent as a result of the above conditions.

1.2 Application of alkane oxidation in the petrochemical industry

Heterogeneous catalysis has been at the forefront of fundamental and influential industrial processes in the last century. The success of German chemist Fritz Haber in synthesising ammonia by feeding N_2 and H_2 at high pressures over an osmium catalyst was modified by Carl Bosch at BASF who found that an iron based catalyst was active and cheap enough to function commercially. The resulting Haber-Bosch process for synthesising ammonia has become one of the most important processes worldwide, earning Haber the 1918 Nobel Prize in chemistry. The three important types of refinery catalysis; hydrocarbon cracking, alkylation and dehydrogenation were developed in the early 1930's. Cracking and alkylation catalysts were used for the production of higher-octane aviation fuel and catalytic dehydrogenation of methylcyclohexane supplied the necessary toluene for the production of TNT during World War II. Table 1.1 illustrates a few examples of important industrial processes which occur via heterogeneous catalysis [3].

1.3 Approach to paraffin activation

Paraffin activation is traditionally achieved through the steam cracking of hydrocarbon feedstocks. The high temperatures and pressure required for steam cracking leads to increased energy demand, operational costs and greenhouse gas emissions. Commercially practised dehydrogenation of alkanes is well established, in particular the dehydrogenation of propane and butane to the respective olefins. These processes are endothermic and therefore thermodynamically limited. One of the greater advantages of such processes is the production of hydrogen gas. The disadvantages are the thermodynamically limited olefin yields, high frequency of regeneration to burn off coke from the catalyst surface and the high energy input requirements [1]. Oxidation of alkanes is an exothermic process which proceeds via the formation of intermediates like alcohols, aldehydes or ketones, carboxylic acids and then to the less desirable combustion products of water, CO and CO_2. Selective oxidation is a challenge which requires the reaction to stop at the production of the intermediates and prior to complete combustion. For these reasons it was desired to invent an oxidative dehydrogenation process for the production of olefins from paraffins that was not thermodynamically limited. The illustrative example shown is the two electron conversion of propane to propene.

$CH_3CH_2CH_3 + ½\ O_2$ (air) → $CH_2 = CHCH_3 + H_2O$

Table 1.1: Major industrial processes using heterogeneous catalysis [3]

Process	**Catalyst**	**Reactants**	**Products**	**End usage**
Haber-Bosch NH_3 synthesis	Fe (magnetite)	H_2, N_2	NH_3	fertilizer, gunpowder, explosives
Methanol synthesis	Cu/ZnO /Al_2O_3	CO, CO_2, H_2	CH_3OH	bulk chemicals, fuel
Fischer-Tropsch	Co, Fe	coal, natural gas	C_5-C_{11} hydrocarbons	automotive fuel
Cracking	clays	long alkanes, C_{12+}	C_7-C_9 alkanes	fuel, detergents
Dehydrogenation/reforming	Pt/Al_2O_3	alkanes	alkenes	polymers, bulk chemicals
Oxidation	vanadium oxide	xylenes	phthalic acids	polymers
Alkylation	zeolites, clays, silicates	C_3-C_5 alkanes	C_7-C_9 isoalkanes	high octane fuel

1.4 Oxidative dehydrogenation

Dehydrogenation is a process which is used on a wide scale industrially for the production of polymers and bulk chemicals as illustrated in Table 1.1. The synthesis of propene, butadiene and styrene, for example, are achieved through dehydrogenation [4]. The limitation faced with dehydrogenation is that high industrial pressures shift the equilibrium of the reaction in the unfavourable direction. Moreover the endothermic reaction is thermodynamically limited. Operation at high temperatures, in the range of 500°C–600°C, results in poor product selectivity due to side reactions such as cracking which are difficult to control [2,5]. A further problem which arises is coke deposition on the catalyst surface which reduces activity and lifetime of the catalyst. It is this high pressure and temperature demand which makes dehydrogenation an expensive process to run [6].

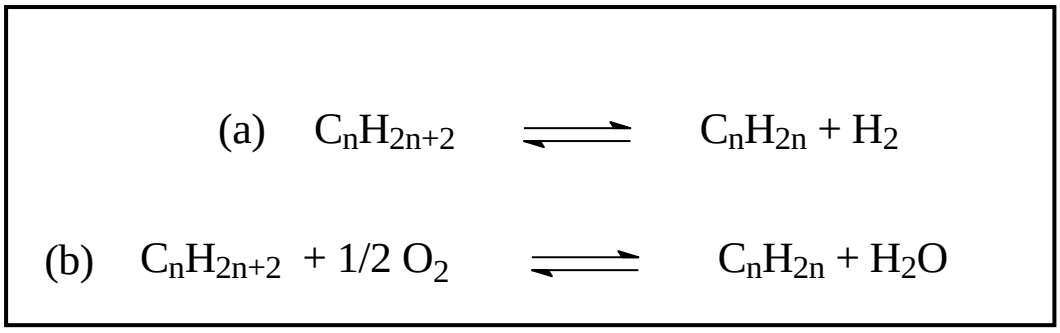

Scheme 1: Dehydrogenation (a) and oxidative dehydrogenation (b) of an alkane

A significant amount of research has been carried out on the selective oxidation of readily available feedstock alkanes to the valuable alkenes and oxygenates as mentioned in sections 1.1 and 1.2. In an oxidative dehydrogenation reaction (represented in Scheme 1 b) molecular oxygen in the reaction medium acts as a hydrogen acceptor and water is produced as a result of the exothermic reaction. The process is therefore thermodynamically favourable and can be carried out at lower temperatures making it economically viable to run [7].

1.5 The mechanism for catalytic oxidation

Catalytic oxidation reactions are thought to occur via a redox mechanism between the substrate and the active sites on the catalyst surface as suggested by Mars and van Krevelen. The Mars-van Krevelen mechanism, illustrated by Figure 1.1, involves the oxidation of the reactant hydrocarbon molecule by lattice oxygen from the solid catalyst [8]. The catalyst in turn is reduced. The reduced catalyst replaces the lattice oxygen by molecular oxygen from the reaction stream and in doing so is reoxidised [7]. The ability of the oxide to donate its structural oxygen (electrical conductivity) determines the activity and selectivity of the catalyst. Therefore a selective oxidation catalyst operating on this mechanism must have a viable redox couple e.g. a transition metal ion, high electrical conductivity and lattice oxygen anion mobility [8].

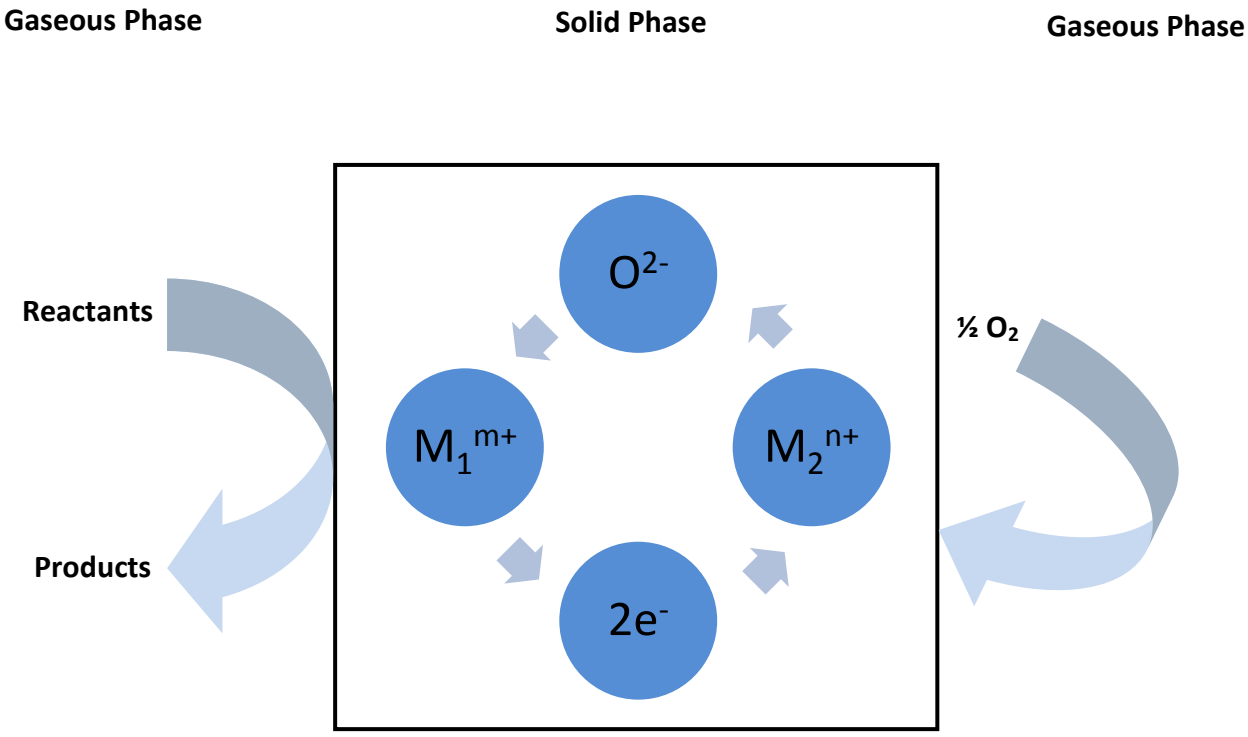

Figure 1.1: Schematic representation of the Mars-van Krevelen mechanism [8]

1.6 Role of the oxygen species

The activation of the substrate molecule i.e. abstraction of the hydrogen from the C-H bond is governed by the electronic potential of the abstracted hydrogen. A negatively charged hydrogen will require an acidic catalyst whereby the oxygen atom of the metal-oxygen double bond is electrophilic ($M^{\partial-}=O^{\partial+}$). Adsorbed oxygen on the surface of a catalyst decomposes at high temperatures to form radical species [4]. These electron deficient radical species (O^{2-}, O^{-}, O_2^{2-}) are strongly electrophilic and will therefore, by nature, attack electron rich regions of the π bonds in a hydrocarbon. These reactions lead to a breakdown of the structure of the hydrocarbon and the formation of degradation products [5]. It is for this reason that electrophilic oxygen species are thought to be responsible for deep oxidation reactions which, in the case of alkane ODH, lead to the formation of CO_2.

A positively charged hydrogen will require a basic catalyst having a nucleophilic oxygen ion ($M^{\partial+}=O^{\partial-}$). Literature has shown that nucleophilic lattice oxygen is required to activate methane, C-H bonds which are situated at α-positions to the double bond and aromatic rings, whereas the opposite holds true for activation of longer chain alkanes like propane [8-9].

1.7. Catalytic reactors

The phase of the reactants (feed, oxidant and diluent which for the purpose of this study are *n*-octane, oxygen and nitrogen, respectively) determines the type of reactor used and the physical form of the catalyst as illustrated in Table 1.2 [10]. In order to improve the quality of industrial processes it is important to fully understand the functioning and capacity of laboratory scale reactors and their respective catalytic systems [11].

A fixed bed reactor consists of a cylindrical tube (usually quartz or stainless steel) which is packed with the solid porous catalyst allowing the reactants to flow through.

Table 1.2: Types of catalytic reactors [10]

Phase of reactants	Type of reactor	Form of catalyst
Gases	Fixed bed	Coarse particles / monolithic structure
	Fluidised-bed	Fine particles
Gas and liquid	Batch reactor	Fine particles
	Bubble column reactor	Fine particles
	Continuous stirred tank reactor	Coarse particles
	Trickle column reactor	Coarse particles / monolithic structure

1.8 The classic gas-solid system

Over 90 % of chemicals worldwide are manufactured through the classic gas/solid system of heterogeneous catalysis usually utilising continuous plug-flow reactors [3]. The gaseous reactants enter the reactor and pass over the solid catalyst bed at high temperatures and/or pressures. Figure 1.2 illustrates the process of catalytic conversion; the gaseous reactants must first diffuse through the catalyst pores, adsorb on its surface, travel to the active site where they must react and thereafter desorb back to the gas phase [3,12]. This journey of the gaseous reactant takes place at the macroscopic level on the surface of the catalyst. Therefore it is the surface interactions of the catalyst which affect its activity, selectivity and stability [3,12]. It follows that characterisation of these solid catalysts is crucial in understanding

parameters such as particle size, shape and surface area which directly affect the catalysts performance. Chapter 5 is dedicated to catalyst characterisation.

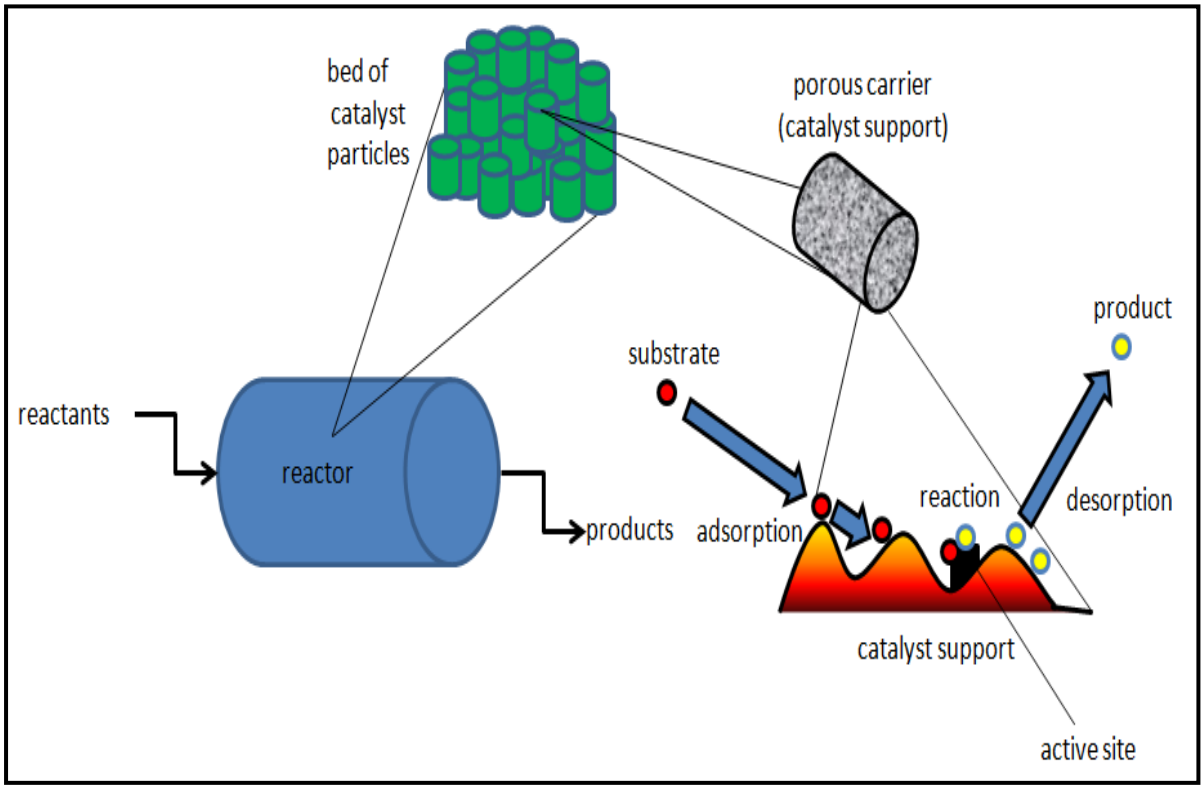

Figure 1.2: A plug-flow catalytic reactor at various zoom-in levels [3]

1.9 Supported metal oxides

The function of a catalyst support is to provide optimal dispersion and good accessibility of the active phase and to stabilise the active phase against sintering [3]. Sintering is catalyst deactivation via thermal degradation. At high temperatures the support pore structure may collapse and the size and shape of the metal crystallites can change. This decreases the catalysts surface area and number of active sites [13]. The temperature of sintering varies, but many metals are sensitive to sintering at ~200°C below their melting point. The active phase of a solid catalyst consists of a small metal cluster, whereas the support is usually a hard unreactive material which has a high melting point. Some commonly used supports are the oxides of silica, alumina and titania and porous carbon. Most supports are chemically inactive, however, in some cases it can be beneficial to have an active support. Cerium oxide

and ceria based mixed oxides ($Ce_xM_{1-x}O_y$) are an example of solid oxygen exchangers. At high temperatures (> 350°C) the redox cycle, $Ce^{3+} \leftrightarrow Ce^{4+} + e^-$ facilitates oxygen storage and release from the fluorite lattice [14]. This support has found application in hydrocarbon fuel cells and automotive three-way catalysis [15-16].

The support itself may also function as a catalyst arising in a bifunctional system. An example of this bifunctional catalytic system is found in the conversion of *n*-heptane to isoheptane which requires both a dehydrogenation catalyst (e.g. Pt/Al_2O_3) and an isomerisation catalyst (e.g. silica or alumina). A catalyst which incorporates Pt impregnated on porous silica or alumina will result in a bifunctional system which can catalyse both processes simultaneously [3]. The study reported in this thesis incorporates the bifunctional system of nickel molybdate, which has been shown to catalyse the ODH of alkanes such as *n*-hexane, supported on carbon nanotubes, which have catalysed the conversion of ethylbenzene to styrene.

1.10 Oxidation of *n*-octane and production of C_8 olefins

The production of higher linear α-olefins is a significant process which finds wide scale application in the chemical industry. These linear α-olefins are intermediates which can be further reacted to produce other fine chemicals. An example of this is hydration to produce aldehydes and ketones [17]. This study focused on the ODH of *n*-octane and the target products of interest were C_8 olefins and oxygenates. A specific target product was 1-octene which is the co-monomer used in the production of high density polyethylene and linear low density polyethylene [18].

Linear α-olefins are produced by catalytic cracking or dehydrogenation of alkanes. Catalytic cracking produces a significant amount of by-products (internal olefins, aromatics and dienes) making the α-olefins produced via this method unsuitable for the production of co-monomers. Dehydrogenation, in addition to being energy intensive and thermodynamically unfavourable, lacks control of the position of the double bond on the olefin. Both processes therefore, are unsuitable for large scale production of linear α-olefins [18].

Herein lies the motivation to develop a suitably active and selective catalytic system for the ODH of *n*-octane to C_8 olefins, in particular 1-octene. The production of oxygenated compounds will also be a significant result. The implementation of such a process has the potential to offer a more economical and environmentally friendly alternative to traditional steam cracking methods.

1.11. Justification of current study and choice of catalytic systems

The aim of this project is to investigate the oxidative dehydrogenation of *n*-octane using three catalysts; nickel molybdate, carbon nanotubes and nickel molybdate supported on carbon nanotubes. Nickel molybdate has been extensively researched as an ODH catalyst of short to medium chain alkanes. The material exists as two polymorphs and the phase which is present significantly affects the activity and selectivity of the catalyst. In more recent work carried out on the ODH of *n*-hexane, the α-phase resulted in 5.3 % selectivity to total hexenes at 4 % conversion at 300°C, whereas the β-phase gave 35.3 % selectivity to total hexenes at 9 % conversion [19].

Carbon nanotubes, due to their high thermal stability and unique structure and surface properties, have been favoured as catalyst supports. Furthermore, carbon nanotubes have been known to have catalytic activity with regards to paraffin activation and have been used in the ODH of ethylbenzene to styrene [20] and propane to propene [21]. Pereira and co-workers reported a 59.2 % selectivity to styrene at 19.6 % conversion of ethylbenzene at 450°C [20]. Research undertaken by Sui and co-workers reported a 42.6 % propene selectivity at 5.33 % conversion of propane at 400°C [21].

The above catalysts have not been explored with respect to the oxidative activation of longer chain paraffins. In particular, the ODH of a C_8 paraffin such as *n*-octane has not been researched with the use of nickel molybdate or carbon nanotube catalysts. Furthermore, supporting the stoichiometric α-nickel molybdate on carbon nanotubes has not been reported and is one of the focal points of this study. This work focuses on the synthesis and characterisation of nickel molybdate and supported nickel molybdate on carbon nanotubes for the ODH of *n*-octane. The three catalysts were tested in a plug-flow fixed bed reactor with

the use of air as the oxidant. A comparison between these catalysts is drawn with respect to their activity and selectivity to various products (refer to section 6.4 for catalytic results).

1.12. References

[1] Grasseli, R. K., *Catalysis Today*, 1999, **49**, 141.

[2] Cavani, F., Trifiro, F., *Catalysis Today*, 1997, **36**, 431.

[3] Rothenberg, G., *Catalysis, Concepts and Green Applications*; Wiley-VCH: Germany, 2008.

[4] Knözinger, H., Weitkamp, J., *Handbook of Heterogeneous Catalysis*, Weinheim: VCH, 1997; Vol. 5.

[5] Madeira, L. M., Portela, M.F., *Catalysis Reviews Science and Engineering*, 2002, **44**, 247.

[6] Cavani, F., Trifiro, F., *Applied Catalysis A: General*, 1992, **88**, 115.

[7] Vedrine, J. C., Millet, J. M. M., Volta, J.C., *Catalysis Today*, 1996, **32**, 115.

[8] Vedrine, J. C.; Coudurier, G.; Millet, J.-M. M., *Catalysis Today*, 1997, **33**, 3.

[9] Busca, G., Finocchio, E., Ramis, G., Ricchiardi, G., *Catalysis Today*, 1996, **32**, 133.

[10] Bond, G. C., *Heterogeneous Catalysis: Principals and Application*s, Oxford Science: London, 1987.

[11] Thomas, J. M., Zamaraev, K.I., *Perspectives in Catalysis*, Academic Press: London, 1992.

[12] Thomas, J. M., Thomas, W.M., *Introduction to the Principals of Heterogeneous Catalysis*, Academic Press: London, 1967.

[13] Anderson, J. R., Boudart, M., *Catalysis: Science and Technology*; Springer-Verlag: Berlin, 1984; Vol. 6.

[14] Trovarelli, A., de Leitenburgh, C., Boaro, M., Dolcetti, G., *Catalysis Today*, 1999, **50**, 353.

[15] Park, S. D., Vohs, J.M., Gorte, R.J., *Nature*, 2000, **404**, 265.

[16] Kaspar, J., Fornasiero, P., Graziani, M., *Catalysis Today*, 1999, **50**, 285.

[17] Centi, G., Cavani, F., Trifiro, F., *Selective Oxidation by Heterogeneous Catalysis*; Kluwer Academic / Plenum Publishers: New York, 2001.

[18] Deutschmann, O., Knözinger, H., Kochloefl, K., Turek, T. In *Ullmann's Encyclopedia of Industrial Chemistry*; 7th ed.; Wiley-VCH: Weinheim, 2009; Vol. 1002, p 313.

[19] Pillay, B., *A study of nickel molybdenum oxide catalysts for the oxidative dehydrogenation of n-hexane*, Ph.D. Thesis, University of KwaZulu-Natal, 2009.

[20] Pereira, M. F., Figueiredo, J.L., Orfão, J.J., Serp, P., Kalck, P., Kihn, Y., *Carbon*, 2004, **42**, 2807.

[21] Sui, Z., Zhou, J., Dai, Y., Yuan, W., *Catalysis Today*, 2005, **106**, 90.

Chapter 2: Nickel Molybdate Catalysts

2.1 Introduction

In the past two decades much progress has been made in the selective partial oxidation of light alkanes with molecular oxygen in the gas phase. Among the various catalysts utilised metal molybdates have emerged to be versatile and successful selective oxidation catalysts of important industrial processes [1]. The multifunctional character of the nickel-molybdenum-oxygen catalytic system is demonstrated by the wide variety of reactions in which it is applied and by the great diversity of products obtained with a given reactant. The catalytic system is the driving force of various important processes such as: hydrogenation and hydrogenolysis of toluene [2], hydrogenation of CO_x [3], hydrodesulfurization and hydrodenitrogenation of petroleum distillates [4]; the water-gas shift reaction [5], steam reforming of hydrocarbons and cracking of *n*-butane [6], oxidative coupling of methane [7], as well as other important hydrogenation and hydrotreating reactions [2,4,8-9]. Nickel molybdates in particular have shown interesting potential for oxidative dehydrogenation of light alkanes like ethane [10], propane [11-13] and *n*-butane [14-16].

2.2 Synthesis

Among the various routes which exist for the synthesis of nickel molybdates, co-precipitation is the most widely used and successful technique and as a result has been patented [17]. The unsatisfactory aspect of co-precipitation is the lack of reproducibility which arises as a result of the dependency of the catalyst precursor or precipitate on the precipitating conditions during synthesis. Both the chemical and textural properties and as a result the overall phase of the catalyst precursor are dependent on various conditions such as the synthesis pH, concentration of reactant ions in solution, rate at which ions are added to the solution, duration of aging of the precipitate in the mother liquor and the temperature of precipitation and filtration. Figure 2.1 illustrates the type of precursor obtained for the various synthesis conditions. Varying of these conditions leads to different precursors having the general

formula xNiOyMoO$_3$$nH_2OmNH_3$ making the synthesis difficult to reproduce. The stoichiometric α-phase is obtained by slowly adding equimolar solutions of nickel nitrate and ammonium molybdate at pH 5.6 and 85°C. The resultant light yellow precursor is dried at 120°C for 5 hours before calcination at 550°C in airflow for 2 hrs to obtain the catalyst [17].

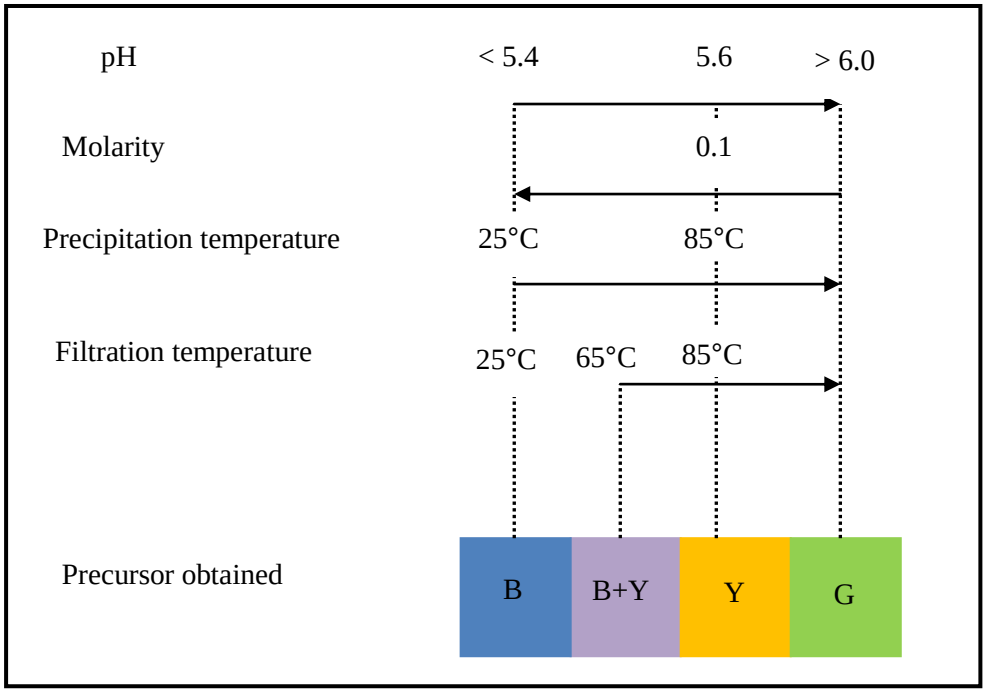

B (blue) = $(NH_4)_4H_6NiMo_6)_{24}\cdot nH_2O\cdot mNH_3$ S+B = stoichiometric α-phase

Y (yellow) = $NiMoO_4\cdot nH_2O\cdot mNH_3$ G (green) = $Ni_{1+x}MoO_4\cdot nH_2O\cdot mNH_3$

Figure 2.1: Synthesis conditions which determine type of $NiMoO_4$ precursor obtained [18]

The stoichiometric catalyst has been used in several studies, however the synthesis procedure used was not always exactly the same. For example Mazzocchia *et al*., in the investigation of the selective oxidation of butane over NiO-MoO_3 catalysts, utilised 0.5 M solutions of $Ni(NO_3)_2.6H_2O$ and H_2MoO_4 with a final pH of 5.1 and at 85°C [15]. However, during the investigation of the influence of thermal treatment on the phase transition of $NiMoO_4$ catalysts, Mazzocchia and Di Renzo used 0.25 M solutions with precipitation at pH 5.2 and temperature of 90°C [19], with filtration of the precipitate at 85°C and drying for 4 hours at 110°C followed by calcination for 2 hours at 550°C [13].

Synthesis of nickel molybdate by the dry mode from NiO and MoO_3 has also been reported [20]. Various other new techniques have been developed for the catalyst synthesis which allow for better control of the contact between phases as compared to the catalysts prepared by impregnation or precipitation. For instance reactive sputtering is an advanced technique which allows for the production of NiO-MoO_3 catalysts with controlled compositions and structures. The use of this technique to create multilayer films of $NiMoO_4$ on α-MoO_3 found an interfacial material identified as β-$NiMoO_4$ which was detected at relatively low temperatures in the bilayer structure [21]. Another technique which involves the use of organic salts, such as an oxalic acid precursor, has the advantage of providing a lower crystallisation temperature [22]. The use of polymers has also been reported, whereby the ionic compounds of the active catalyst is contained inside an organic polymeric matrix such as agar-agar which will contain the Ni and Mo ions inside in a 1:1 atomic ratio [23]. The advantage offered by this approach is its inexpensive simple preparation of multi-component catalytic systems by dissolution of the desired elements at appropriate concentrations in aqueous solution [23]. The sol-gel technique offers a method for catalyst synthesis at low temperature with excellent control of the stoichiometry of the precursor. Anouchinsky et al. have prepared several catalysts by this technique and achieved a homogeneous dispersion of Ni and Mo ions in the precursor and crystallisation at temperatures lower than that obtained through co-precipitation. This allowed for the stabilisation of the β-phase at lower temperatures [23]. Nanocrystalline molybdates, including $NiMoO_4$ have been synthesised by evaporation of a polymer-based metal-complex precursor solution which produces fine grained materials having diameters less than 100 nm with potential application in many technological areas [24-25].

2.3 Transition of the phases

Three different structures of nickel molybdate exist with only two of these being stable at room temperature. The phase of catalyst which exists is dependent on the synthesis conditions as well as the temperature and pressure. The α-phase is stable at room temperature and contains molybdenum in a pseudo octahedral coordination. The high temperature β-phase contains molybdenum in a tetrahedral coordination and is metastable.

These two polymorphs were first discovered by Plyasova et al. who reported the crystal structure to be monoclinic [26]. The α-phase (then termed the P-phase) when heated to ca. 650 °C was converted to the β-phase (then termed the N-phase). The metastable β-phase, upon cooling to 200°C, reverts back to the stable room temperature phase.

The thermal transitions of stoichiometric nickel molybdate (Ni:Mo ratios of 1) which were calcined at 550°C were investigated. The DTA cycle in Figure 2.2 showed an endothermic effect on heating of the solid to 720°C attributed to the conversion of the α → β-phase and an exothermic transition on cooling to 200°C attributed to the reverse transformation of β → α-phase [27].

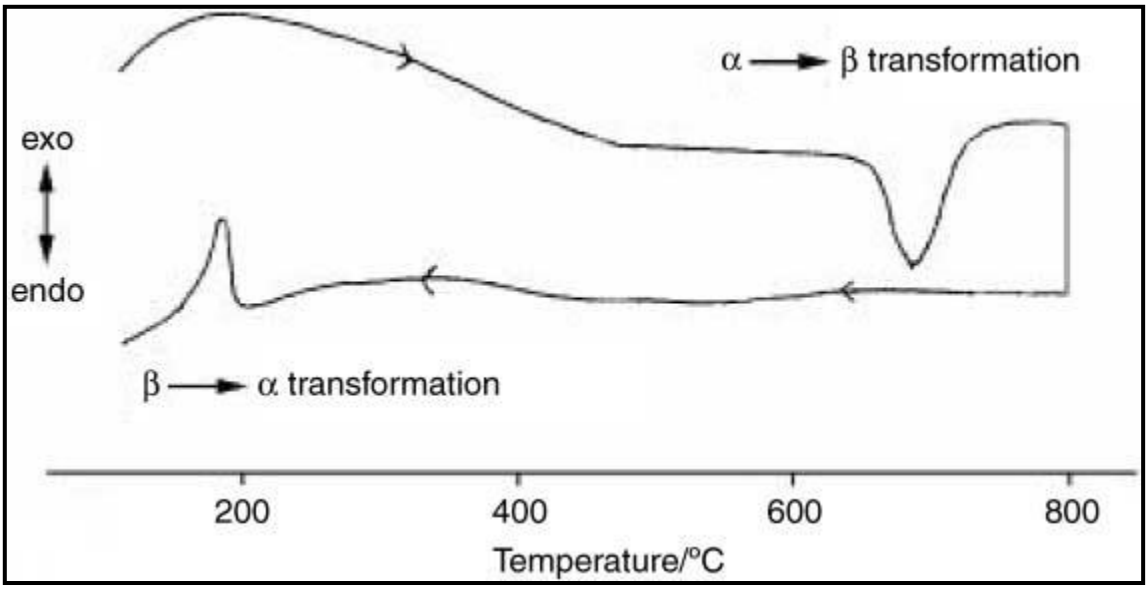

Figure 2.2: DTA cycle of stoichiometric nickel molybdate phase transitions [27]

Initially it was thought that the α-phase is octahedrally coordinated whereas the β-phase is tetrahedrally coordinated [28], however more recent studies of the phase transitions have provided a more accurate description. Rodriquez et al. have reported results of Rietveld refinement of XRD and density functional theory measurements which depict molybdenum to be coordinated in a pseudo-octahedral environment having two long Mo-O bonds [29].

2.3.1 Stabilisation of the β-phase at room temperature

The high temperature β-phase is catalytically more selective in the ODH of alkanes to alkenes (as discussed in section 2.5) and it is therefore desirable to stabilise this phase at room temperature and various attempts have been made in this regard [30-31]. The reason for the instability of the β-phase at room temperature is attributable to the fact that the α-phase is 9 kcal/mol more stable than the β-phase and the phase transition from α→β requires that an energy barrier of 50 kcal/mol be overcome [29].

AbdelDayem and Sadek reported the influence of ɣ-irradiation on the phase transition of α-$NiMoO_4$. It was found that ɣ-irradiation effectively reduced the temperature of the α→β transition, however did not alter the temperature of the reverse β→α transition [32]. This occurrence, as inferred from the XRD results, was attributed to the induced strain within the α-$NiMoO_4$ crystal as a result of radiation. The catalysts were tested in the ODH of cyclohexane at 500°C and the results showed that the ɣ-irradiated nickel molybdate resulted in a 3.5 % selectivity to cyclohexene in comparison to the unirradiated parent α-$NiMoO_4$ which resulted in a 0.2 % selectivity at isoconversion (5 %) [32].

2.4 Oxidation of hydrocarbons

Ozkan and Schrader have reported strong evidence in their work which suggests that the presence of excess MoO_3 in molybdate catalysts significantly affects the catalytic behaviour of selective oxidation reactions [7]. Nickel molybdates with excess MoO_3 were prepared and used to catalyse the reactions of C_4 hydrocarbons (1-butene [33], butadiene and furan [34]) to maleic anhydride. There is a great interest in maleic anhydride production due to its versatility, with uses ranging from agricultural chemicals, paints, synthetic resins and food additives. High selectivities to maleic anhydride were obtained with catalysts containing specific concentrations of MoO_3 (with a maximum of 15 % molar excess of MoO_3), whereas pure $NiMoO_4$ and MoO_3 were not selective. The most selective and stable catalyst was a MoO_3 phase superficially covered with $NiMoO_4$. Characterisation of the spent catalysts showed no change in the chemical or structural properties but did display a change in colour from yellow to dark grey as a result of carbon deposition on the surface [33]. With respect to the roles of each of the phases it was found that the competing processes of carbon oxides

and maleic anhydride formation were the determining factor in maleic anhydride selectivity as both processes occur at different MoO_3 sites. The $NiMoO_4$ phase selectively blocks the MoO_3 sites responsible for total oxidation and is the phase responsible for 1-butene oxidation therefore favouring selectivity to maleic anhydride [34].

Zou and Schrader, during the oxidation of 1-butene to furan and maleic anhydride, obtained a high selectivity to butadiene with yields of about 48 % when a thin film of nickel molybdate was deposited on MoO_3 which was previously supported [21].

Extensive studies have been carried out by Mazzocchia et al. in selective oxidation of hydrocarbons over Ni-Mo-O catalysts [20]. The authors mentioned were also responsible for pioneering the work on 1-butene oxidation to maleic anhydride over several catalysts. Yet again the catalyst with excess Mo relative to α-$NiMoO_4$ was found to be active and selective. Pulsed-feed experiments have shown that the ODH of 1-butene to butadiene occurs via a redox mechanism, whilst the production of partial and total oxidation products occurs via other forms of adsorbed oxygen. The highest selectivity to maleic anhydride achieved was 64 % as a result of the Mo(V) sites which activate molecular oxygen and exist in catalysts with MoO_3 present in a $NiMoO_4$ matrix.

It is clear that the presence of excess MoO_3 is crucial in oxidation reactions and the same is true for propene oxidation. The method of synthesis of the catalyst precursor, however, significantly affects the catalytic behaviour. Preparation of precursors, having the same atomic composition, but via different methods, results in catalysts with different properties. Various authors have investigated the use of Ni-Mo-O catalysts in propene ODH, particularly to acrolein and acrylic acid [20]. While all catalysts tested produced acrolein, only catalysts with excess MoO_3 produced acrylic acid. In addition, β-$NiMoO_4$ converted both propene and acrolein to acrylic acid, whereas the α-phase was inactive in both cases. Ferlazzo et al. have patented their version of the molybdenum based catalytic system for the ODH of propene which is formed with one or two crystalline phases and at least one promoter element (US patent No. 4,388,223) [35]. In a run involving the β-$NiMoO_4$ phase, a 95.3 % conversion of propene was achieved with 95.6 % selectivity to acrolein and acrylic acid. Mazzocchia et al. while investigating the direct oxidation of propene to acrylic acid synthesised a binary catalytic system $NiMoO_4 \cdot 2MoO_3$ which was promoted with $Te(Te_2MoO_7)$ which

significantly increased the catalysts performance [11]. It was found that the molybdic anhydride phase considerably increased the activity and selectivity of $NiMoO_4$, while tellurium increased the selectivity to acrylic acid. It was also found that tellurium decreases conversion, which possibly results from the fact that tellurium molybdate accelerates the $\alpha \rightarrow \beta$ $NiMoO_4$ transformation, resulting in a less active catalyst [11].

2.5 ODH of alkanes

The catalytic production of butadiene has been the subject of research for a significant period due to its use as a monomer in the production of synthetic rubber. Therefore the need exists to find a suitably active and selective catalytic system for the ODH of *n*-butane to butadiene [36]. Bertus et al. pioneered a study which used a nickel molybdate catalyst to obtain yields of butadiene between 4.3-13.5 % at 33 % selectivity [37]. Pilipenko et al. investigated the effect of composition of the nickel-molybdenum system in the conversion of *n*-butane and found the optimal atomic ratio of Ni:Mo to lie between 1.28 and 1.92 with a 54 % selectivity to butadiene at 17.1 % yield [16]. The conversion was found to decreases as MoO_3 content increased, whereas pure NiO provided virtually zero selectivity to butadiene albeit at high conversions. The study concluded that the α-$NiMoO_4$, NiO and β-$NiMoO_4$ were the most effective phases in *n*-butane to butadiene ODH and have suggested that NiO is the species responsible for the butane to butadiene conversion step [16]. Itenberg et al. however provided a different account of the same study and while they agree that NiO and MoO_3 are active in the ODH of *n*-butane to butadiene, the low conversions and selectivities led them to conclude that these were not the species responsible for the catalytic activity of the system [14]. A comparison of catalytic tests carried out between catalysts having varying compositions showed that at isoconversion the maximum selectivity (to both butenes and butadiene) was obtained with catalysts having Ni:Mo ratios between 1.0 and 1.2. This study of phase composition concluded that the active component was nickel molybdate or a solid solution of nickel oxide in the molybdate lattice [14]. A shift in these ratios ($m > 1.2$ or $m < 1.0$) results in a decrease in selectivity as a result of the effect of the individual oxides which comes into play. This study also suggests that the crystalline phase of the nickel molybdate, be it the α or β-phase does not affect the activity and selectivity of butane ODH and both these catalysts provide essentially the same results [14]. Cavani and Trifirò have reported similar findings with regards to butane ODH [38]. However results obtained by Mazzocchia et al. and

Madeira and Portela disagree with these findings [11,39]. Studies carried out by the authors have reported the α-phase to be more active, while the β-phase phase is more selective at comparable conversions and similar temperatures, with regards to butane ODH [39].

Lezla et al. have investigated the effect of phase composition of nickel molybdate catalysts in propane ODH and found the α-phase to be active [12]. An increase in composition of molybdenum oxide in the nickel molybdate was found to improve catalytic behaviour and the optimal ratio of Ni:Mo was found to1:1.27 which resulted in a 63 % selectivity to propene at 22 % propane conversion [12]. Thomas et al. carried out a similar study of the nickel molybdate catalytic system in propane ODH and found that selectivity to propene was enhanced for Mo-rich catalysts [40]. Stern and Grasselli investigated various simple molybdates of the type $AMoO_4$ (A= Ni, Co, Mg, Mn or Zn) for the ODH of propane and found that nickel molybdate was the most active with a 60 % selectivity of propene achieved at 27 % conversion. It was found that the molybdenum-oxygen bond is responsible for propane activation and consequently bonds of the type Ni-O-Mo-O are the most active [41]. Mazzocchia et al. have reported the α-phase to be slightly more active, whilst the β-phase is almost twice as selective to propene at comparable conversion and identical temperatures [13].

Pillay et al. studied the effect of phase composition of Ni-Mo-O catalysts in the ODH of *n*-hexane. The β-phase was reportedly the most selective catalyst for the synthesis of hexenes with 25 % selectivity to 1-hexene obtained at 9 % conversion. The difference in Mo coordination between the α and β-phases is believed to be the reason for the β-phase being more active and selective than the α-phase. The pure phases of NiO and MoO_3, although active in hexane ODH, showed poor selectivity to the hexenes at comparable conversions suggesting that they are not responsible for the catalytic activity of the NiO-MoO_3 system. The α-phase with additional MoO_3 was more active than the α-phase alone suggesting a synergistic relationship exists between the two phases [42].

2.6 Structural properties

The nature of the active sites of molybdenum containing catalysts has been the subject of investigation by various authors [43]. The use of surface characterisation techniques such as ESR and XPS in particular, has made a significant contribution to the understanding of the oxidation state of the active species. Many authors have recognised the role of Mo^{5+} as an active species in selective oxidation of hydrocarbons. In a study utilising ESR, Watson and Ozkan reported changes in Mo(V) species when in contact with propane [44]. The role played by Mo^{5+} species as part of the Mg-Mo-O catalytic system in the ODH of propane was studied by XPS and EPR. The authors suggested that the active site consisted of a coordinatively unsaturated form of Mo^{5+}, which is possibly generated on the surface by propane reduction [45-46].

The use of coupled Mo(V)/Mo(VI) redox pairs in propane ODH over molybdenum phosphates has also been reported [47]. In the case of propane ODH over Mg-Mo-O and Co-Mo-O systems it has been reported that catalytic performance increases with an increase in weak surface acid sites suggesting the involvement of these sites in propane activation [18]. Haarlin et al. reported the active state of Mo in the dehydrogenation of *n*-butane to be either Mo^{5+} or Mo^{4+} which upon further reduction leads to an increase in selectivity to cracking and the formation of coke [48].

The widely accepted consensus with regards to the Ni-Mo-O catalytic system accepts Mo^{5+} species to be present amongst the active sites. During the investigation of the conversion of butane to butadiene and maleic anhydride, Mazzocchia et al. reported evidence suggesting that butane dehydrogenation occurs without the use of lattice oxygen [15]. It was found that the formation of maleic anhydride is related to the activation of gaseous oxygen over sites which disappear through deep reduction and cannot be regenerated by re-oxidation [15]. It was suggested that these sites possibly belong to those of Mo(V). It has also been reported that the Mo^{6+}/Mo^{5+} redox couple is responsible for the ODH of propane [12]. It is evident that further research is necessary in order to provide a clear understanding of the nature of the active sites of nickel molybdate catalysts. The use of surface sensitive techniques is crucial in this regard and such catalyst characterisation techniques will provide valuable insight into the Ni-Mo-O catalytic system.

2.7 Kinetics and mechanism

The reason for the β-phase being more selective than the α-phase is the different types of oxygen bonds at the active sites. The presence of metal-oxygen double bonds is usually associated with the formation of oxygen containing products. The β-phase has a band which appears at lower frequencies in the infrared spectrum, which leads to the metal-oxygen double bond to be weaker in character as compared to that of the α-phase. This results in the higher temperature phase being more selective to dehydrogenation products [27]. Kaddouri et al. recently studied the difference in activity and selectivity of the two nickel molybdate phases and attributed this to the different reducibility of the phases. Interestingly enough in the case of propane ODH, a relationship was found between the reducibility of the catalysts and the catalytic behaviour indicating that lattice oxygen plays an important role in the reaction. It was concluded that the ODH process is governed by a redox mechanism known as the Mars-van Krevelen mechanism [49]. It was proposed that the formation of propene begins with the reaction of propane with superficial O^{2-} anions which then leads to the development of anionic vacancies (Vo^{oo}) shown in equation 1 [13]. The active oxygen species in propane ODH is regenerated through spontaneous re-oxidation of the surface by gaseous oxygen as displayed by the Mars-van Krevelen mechanism represented in equation 2.

$$C_3H_8 + O_s^{2-} \rightarrow C_3H_6 + H_2O + Vo^{oo} + 2e^- \qquad (1)$$

$$\frac{1}{2}O_2\,(g) + Vo^{oo} + 2e^- \rightarrow O_s^{2-} \qquad (2)$$

2.8 Coke deposition

The effects of coke deposition on nickel molybdate catalysts during the ODH of *n*-butane were reported by Maldonado-Hodar and co-workers [50]. Surprisingly it was observed that coke deposition did not result in deactivation but on the contrary conversion was found to increase to more than 40 % as well as lead to selectivity to dehydrogenation products, particularly butadiene. These effects were attributed to the stabilisation of the more selective β-phase at low temperatures as well as to the presence of catalytically active coke [50].

2.9 Supported nickel molybdate

There have been fewer reports on the use of supported nickel molybdate catalysts for the ODH of alkanes. Recent studies have reported the use of TiO_2 [51] and SiO_2 [52-53] supported catalysts on isobutene ODH. The supported catalysts were found to be more selective to isobutene than their unsupported counterparts. This is attributed either to the acid-base properties of the support surface or to the stabilisation of the β-phase at a lower temperature. The latter point is of significance as the β-phase is only metastable at room temperature and on an industrial scale it is not practical to keep the reactor operational above 200°C to avoid the transition back to the α-phase [51-53]. Attempts have been made to incorporate excess nickel in the catalysts to stabilise the β-phase at lower temperatures, however this was found to favour competitive side reactions. Silica-supported nickel molybdate catalysts synthesized via the sol-gel technique were tested in isobutene ODH, however no significant yields were obtained [30,54].

2.10 References

[1] Centi, G., Cavani, F., Trifiro, F., *Selective Oxidation by Heterogeneous Catalysis*, Kluwer Academic / Plenum Publishers: New York, 2001.

[2] Tsurov, M. A., Afanasiev, P.V., Lunin, V.V., *Applied Catalysis A: General*, 1993, **105**, 205.

[3] Aksoylu, A. E., Isli, A.I., Onsan, Z.I., *Applied Catalysis A: General*, 1999, **183**, 357.

[4] Vasudevan, P. T., Fierro, J.L.G., *Catalysis Reviews: Science and Engineering*, 1996, **38**, 161.

[5] Andreev, A.A., Kafedjiysky, V.J., Edreva-Kardjieva, R.M., *Applied Catalysis A: General*, 1999, **179**, 223.

[6] Borowiecki, T., Giecko, G., Panczyk, M., *Applied Catalysis A: General*, 2002, **230**, 85.

[7] Ozkan, U., Schrader, G.L., *Journal of Catalysis*, 1985, **95**, 120.

[8] Li, D., Nishijima, A., Morris, D.E., *Journal of Catalysis*, 1999, **182**, 339.

[9] Sarbak, Z., *Applied Catalysis A: General*, 2001, **207**, 309.

[10] Kaddouri, A., Anouchinsky, R., Mazzocchia, C., Madeira, L. M., Portela, M. F., *Catalysis Today*, 1998, **40**, 201.

[11] Mazzocchia, C., Anouchinsky, R., Kaddouri, A., Sautel, M., Thomas, G., *Journal of Thermal Analysis*, 1993, **40**, 1253.

[12] Lezla, O., Bordes, E., Courtine, P., Hecquet, G., *Journal of Catalysis*, 1997, **170**, 346.

[13] Mazzocchia, C., Aboumrad, C., Diagne, C., Tempesti, E., Herrmann, J.M., Thomas, G., *Catalysis Letters*, 1991, **10**, 181.

[14] Itenberg, I.S., Andrushkevich, M.M., Buyanov, R.A., Khramova, G.A., Sitnikov, V.G., *Kinetics Catalysis*, 1976, **17**, 867.

[15] Mazzocchia, C., Del Rosso, R., Centola, P., *Anales de Quimica*, 1983, **79**, 108.

[16] Pilipenpnko, F.S., Tsailingol'd, A.L., Stepanov, G.A., *Kinetics Catalysis*, 1976, **17**, 842.

[17] Mazzocchia, C., Tempesti, E., Aboumrad, C. In *U.S Patent (Editor)*; Norsolor, Ed. 1992; Vol. 5,086,032.

[18] Madeira, L. M., Portela, M.F., Mazzocchia, C., *Catalysis Reviews*, 2004, **46**, 53.

[19] Di Renzo, F., Mazzocchia, C., *Thermochemica Acta*, 1985, **85**, 139.

[20] Mazzocchia, C., Del Rosso, R., Centola, P., *Revista Portuguesa de Quimica*, 1977, **19**, 61.

[21] Zou, J. Y., Schrader, G.L, *Thin Solid Films*, 1998, **324**, 52.

[22] Mazzocchia, C., Kaddouri, A., Anouchinsky, R., Sautel, M., Thomas, G., *Solid State Ionics*, 1993, **63**, 731.

[23] Anouchinsky, R., Kaddouri, A., Mazzocchia, C., *Journal of Thermal Analysis*, 1996, **47**, 299.

[24] Sen, A., Pramanik, P., *Matter Letters*, 2001, **50**, 287.

[25] Sen, A., Pramanik, P., *Materials Letters*, 2002, **52**, 140.

[26] Plyasova, L.M., Ivanchenko, I.Y., Andrushkevich, M.M., Buyanov, R.A., Itenberg, I.S., *Kinetics Catalysis*, 1977, **14**, 882.

[27] Kaddouri, A., Del Rosso, R., Mazzochia, C., Fumagalli, D., *Journal of Thermal Analysis and Calorimetry*, 2001, **63**, 267.

[28] Rodriquez, J. A., Chaturvedi, S., Hanson, J.C., Albornoz, A., Brito, J.L., *Journal of Physical Chemistry*, 1998, **102**, 1347.

[29] Rodriquez, J.A., Hanson, J.C., Chaturvedi, S., Maiti, A., Brito, J.L., *Journal of Physical Chemistry*, 2000, **112**, 935.

[30] Tempesti, E., Kaddouri, A., Mazzocchia, C., *Applied Catalysis A: General*, 1998, **166**, L259.

[31] AbdelDayem, H. M., Alomair, M., *Industrial & Engineering Chemistry Research*, 2008, **47**, 1011.

[32] AbdelDayem, H. M., Sadek, S. A., *Thermochimica Acta*, 2008, **473**, 96.

[33] Ozkan, U., Schrader,G.L., *Journal of Catalysis*, 1985, **95**, 137.

[34] Ozkan, U., Schrader, G.L., *Journal of Catalysis*, 1985, **95**, 147.

[35] Ferlazzo, N., Bertollini, N., Ghirga, M. In *US Patent (Editor)*; Norsolor, Ed. 1983; Vol. 4,388,233.

[36] Stepanov, G.A., Tsailingol'd, A.L., Pilipenko, F.S., Sobolev, A.M., Boreskov, G.K., Buyanov, R.A., Veniaminov, S.A. In *British Patent*; Norsolor, Ed.; Vol. 1,197,537.

[37] Bertus, B. J. In *US Patent*; Norsolor, Ed.; Vol. 3,793,225.

[38] Cavani, F., Trifiro, F., *Selective oxidation of C_4 paraffins*, In *Catalysis*, Specialist Periodical Report, Royal Society of Chemistry: Cambridge, 1994; Vol. 11, 246.

[39] Martin-Aranda, R.M.; Portela, M.F., Madeira, L.M., Freire, F., Oliveira, M., *Applied Catalysis A: General*, 1995, **127**, 201.

[40] Thomas, G., Sautel, M., Kaddouri, A., Mazzocchia, C., *Solid State Ionics*, 1997, **101**, 775.

[41] Stern, D. L., Grasselli, R.K., *Journal of Catalysis*, 1997, **167**, 550.

[42] Pillay, B., Mathebula, M. R., Friedrich, H.B., *Applied Catalysis A: General*, 2009, **361**, 57.

[43] Madeira, L. M., Portela, M.F., *Catalysis Reviews Science and Engineering*, 2002, **44**, 247.

[44] Watson, R. B., Ozkan, U.S., *Journal of Molecular Catalysis A:Chemistry*, 2003, **194**, 115.

[45] Cadus, L.E., Abello, M.C., Gomez, M.F., Rivarola, J.B., *Industrial & Engineering Chemistry Research*, 1996, **35**, 14.

[46] Abello, M.C., Gomez, M.F., Cadus, L.E., *Industrial & Engineering Chemistry Research*, 1996, **35**, 2137.

[47] Khan, M.M., Somorjai, G.A., *Journal of Catalysis*, 1985, **91**, 263.

[48] Haarlin, M. E., Backman, L.B., Krause, A.O.I., Jylha, O.J.T., *Journal of Catalysis*, 1999, **183**, 300.

[49] Vedrine, J. C., Millet, J. M. M., Volta, J.C., *Catalysis Today*, 1996, **32**, 115.

[50] Maldonado-Hódar, F.J., Madeira, L. M., Portela, M. F., Martín-Aranda, R. M., Freire, F., *Journal of Molecular Catalysis A: Chemical*, 1996, **111**, 313.

[51] Zãvoianu, R., Dias, C. R., Farinha Portela, M., *Catalysis Communications*, 2001, **2**, 37.

[52] Dias, C. R., Zãvoianu, R., Portela, M.F., *Catalysis Communications*, 2002, **3**, 85.

[53] Dias, C. R., Zãvoianu, R., Portela, M.F., *Catalysis Letters*, 2002, **77**, 317.

[54] Cauzzi, D., Deltratti, M., Predieri, G., Tiripicchio, A., Kaddouri, A., Mazzocchia, C., Tempesti, E., Armigliato, A., Vignali, C., *Applied Catalysis A: General*, 1999, **182**, 125.

Chapter 3: Carbon Nanotubes

3.1 Background

Carbon nanotubes (CNTs) are exceptionally interesting from a fundamental research point of view. CNTs are hollow cylinders of sp^2 hybridised graphite sheets which are chemically stable, mechanically very strong and conduct electricity. For this reason, the material lends itself to various applications such as nano-transistors in circuits, field emission displays, artificial muscles and added reinforcements in alloys [1].

Carbon nanotubes were first discovered in 1991 in their multi-walled form by Sumio Iijima, an electron microscopist, then working at the NEC laboratories in Japan. He had used transmission electron microscopy to study soot and had noticed a variety of novel carbon architectures including large cylindrical deposits of long hollow fibres. Two years later he discovered the tubes in their single-walled form [2]. Since then the material has found potential application in the fields such as mechanics, optics and electronics. There has been a considerable amount of progress in these areas and the first initial applications appeared on the market about 8 years ago [1].

Since there are many ways to roll a sheet into a tube, the tubes may have different diameters and microscopic structures. Single-walled carbon nanotubes (SWCNTs) consist of a single layer of graphite rolled up into a hollow cylinder, whereas multi-walled carbon nanotubes (MWCNTs) comprise of several concentrically arranged cylinders. SWCNTs form hexagonal packed bundles during the growth process and have a wall to wall distance between two tubes in the same range as the interlayer distance in graphite of 3.41 Å. MWCNTs have similar lengths to SWCNTs but much larger diameters in the range of 5 to 100 nm and many of their properties are similar to those of graphite (properties are tabulated in Table 3.1). While MWCNTs have found wide scale application, their structural and electronic properties are less well defined due to the large number of possible layers which may exist [3].

Table 3.1: Structural features and electronic properties of CNTs and CNFs [4]

Property	**SWCNT**	**MWCNT**	**CNF**
Diameter[a] (nm)	0.5-2 (1-1.5)	5-200 (10-40)	10-500 (50-100)
Length	Few μm up to 20 cm	Few to hundreds of μm	Few to hundreds of μm
Apparent density (g/cm^3)	0.5-1	0.02-0.3[b]	0.3-1.4
S_{BET} (m^2/g)	400-900	50-450	10-250
Porosity (cm^3/g)	Microporous	Mesoporous	Mesoporous
Young's modulus (TPa)	1.05-1.3	0.5-1.2	0.3-0.7
Tensile strength (GPa)	45-150	3-30 to 150[c]	3-12
Electrical conductivity (S/cm)	550	80-1000	300
Electrical resistivity (Ω·cm)	6×10^{-4}	$(0.6\text{-}2) \times 10^{-4}$	1.5-3
Thermal conductivity[d] (W/*K*·m)	1000-6000[e]	300-3000[b]	800-2000

[a]Typical values in parentheses.

[b]The lower value is for a powder and the upper for short MWCNTs.

[c]Defect-free MWCNTs.

[d]Axial thermal conductivity at room temperature.

[e]For a single rope of SWCNTs.

3.2 Properties which make CNTs suitable for Catalysis

The study of structural, electronic, mechanical and thermal properties of CNTs is vital in catalysis. This allows one to better understand their stability as well as the interaction of the metal particle with that of CNTs, in the case of supported metal catalysts. Furthermore it is of interest to understand how chemicals react with these supported metal catalysts and what these novel carbon forms can bring to the field of catalysis.

3.2.1 Structural features and electronic properties

Carbon nanotubes can either be single walled or multi walled. Single walled CNTs consist of a single graphene sheet rolled up into a cylinder and closed to semi-fullerene caps. Multi walled CNTS can be considered as concentric SWCNTs with an increasing diameter and coaxially disposed. Carbon nanofibers (CNFs) can be considered as a carbon nanotube without an inner cavity [1]. The characteristics of these materials are displayed in Table 3.1. Characterisation of CNT structure has mainly been carried out by electron microscopy (SEM and TEM), Raman spectroscopy, thermal analysis (TGA-DSC) and absorption spectroscopy (UV-vis-NIR and IR). Certainly no single technique can give a complete description of the CNT sample. A combination of these techniques is needed to determine the type (SWCNTs, MWCNTs or CNFs), quality, quantity and properties of the sample. High resolution TEM (HR-TEM) is arguably the most widely used and powerful technique. Recent technology has allowed the atomic network which makes up the tubes as well as the layered structure to be imaged directly, allowing for a better understanding of their structure [2]. Electron diffraction has been useful for the study of SWCNTs but is of less value for MWCNT as the diffraction pattern of MWCNTs contain spots from tubes of different chiralities making the pattern difficult to interpret [2].

There are two possible theoretical structures for nanotubes known as zig-zag and armchair, illustrated in Figure 3.1 (a) and (b) respectively. It is believed that in practice most nanotubes do not have these highly symmetric structures mentioned but rather are arranged helically around the tube axis. These structures (Figure 3.2) are aptly termed chiral as they can exist as mirror images of each other [2]. Most MWCNTs grown by catalytic chemical vapour deposition (CVD) result in a bamboo shaped structure (see Figure 5.25 b) with the graphene layers perpendicular to the tube walls, which makes the inner cavity rarely accessible. Therefore relatively few studies deal with the inner layer of MWCNTs [4]. Nitrogen doped CNTs also result in the bamboo-like structure and therefore nitrogen can be used to alter the physiochemical properties of the tubes. The precise lengths and diameters of CNTs are difficult to control and thus arises the problem of standardisation for the material [4].

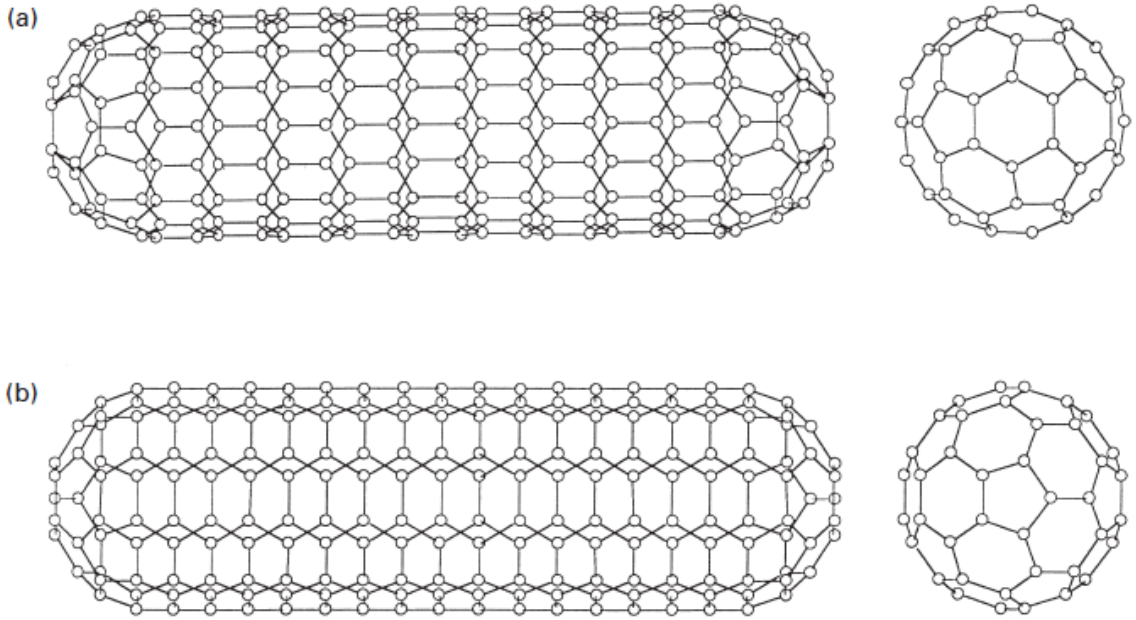

Figure 3.1: Structure of CNTs showing the (a) zig-zag and (b) armchair configurations [2]

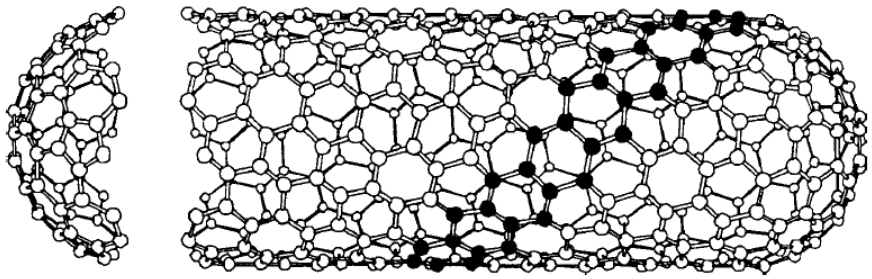

Figure 3.2: Structure of a chiral nanotube [2]

3.2.2 Adsorption properties

A high surface area and well developed porosity are important structural features for achieving a high dispersion of the active phase in a catalyst. Carbon based supports have a much higher surface area as compared to other conventional supports like silica and alumina however a large part of this surface area may be contained in narrow micropores and thus unavailable to the reactants [5]. Thus the porous nature of CNTs makes the material an attractive choice for catalysis (refer to section 5.3.6). In MWCNTs the pores can be divided into inner hollow cavities of small diameter (narrowly distributed, mainly 3-10 nm), external walls and aggregated pores (widely distributed, 2- 100 nm). The aggregated pores are formed

by interaction of isolated MWCNTs and are important for adsorption [5]. MWCNTs can be classified as a mesoporous material which contains some macroporosity (pores > 50 nm) [4]. The predominant mesoporous structure significantly reduces diffusion transport limitations which occur with other materials like activated carbon. Microporosity can be brought about by chemical activation of the tubes by treatment with a base (KOH or NaOH) which has also been reported to purify and open the tubes simultaneously, thus altering the pore structure [3]. It is important to note that the defects and kinks which occur on MWCNTs display enhanced reactivity and may act as active sites for catalysis [6]. These unavoidable imperfections play a key role in tailoring the adsorption properties.

3.2.3 Mechanical and Thermal properties

The unique mechanical strength of CNTs is as a result of the particularly strong bonds in the curved graphene sheet which are stronger than those in diamond as revealed by the C-C bond lengths (0.142 for graphene and 0.154 in diamond). This strength makes the material particularly stable towards deformation with a Young's modulus in the order of terapascals as displayed in Table 3.1. Another important property of the material is its thermal stability and thermal conductivity under reaction conditions [7]. Thermogravimetric analysis is used to study the resistance of a carbonaceous material toward heating in air (refer to section 5.3.8). It was found that CNTs are more stable toward oxidation than activated carbons, but more reactive than graphite. It is important to note that the presence of residual metal on or inside the tubes, as well as the concentration of surface defects, which catalyse carbon gasification, could lower the temperature at which gasification occurs. This makes an objective comparison difficult. It is accepted, however, that amorphous carbon burns off first, followed by SWCNTs and then MWCNTs [4].

3.3 Carbon as a catalytic support

3.3.1 Porous carbon catalytic supports

Porous carbon materials lend themselves as ideal supports for heterogeneous catalysts due to their physical and chemical surface properties. These properties can be tailored to develop a large surface area to disperse the active phases, the proper pore size distribution to facilitate the diffusion of reactants and products to and from the surface and the acid-base character needed for obtaining the best performance. Even though carbon-supported catalysts are considered to be the best choice for a large number of reactions, very few large scale processes currently use carbon supported catalysts. The reason for this is the lack of reproducibility that arises with carbon supported catalysts due to the poor understanding of the properties which influence the materials behaviour. Fortunately the increasing number of scientific publications on carbon supported catalysts is helping to better understand the subject. One of the earliest reviews focusing on carbon supports for the preparation of highly dispersed metal catalysts was carried out in 1984 by Ehrburger [8]. One of the more recent reviews by Rodríguez-Reinoso et al. focuses on the use of carbon materials as catalysts and catalytic supports [5,9]. Of the large number of carbon materials which can and have been used as catalytic supports, among the most popular are granular and powdered activated carbons and carbon blacks but there is an increasing interest in activated carbon fibres, nanotubes and nanofibers [10]. A comprehensive review on the use of these materials as catalysts and catalytic supports has been published [11]. The various advantages offered by carbon supports over traditional catalytic supports are mentioned below [5]:

- The carbon surface is resistant to both acidic and basic media
- The structure is stable at high temperatures
- The pore structure can be tailored to obtain the pore size distribution for a given application
- Porous carbons can be prepared with a variety of macroscopic shapes (e.g. granules, powders, fibres, cloths, pellets, monoliths, discs, tubes)
- The chemical property of the surface can be modified to control polarity and hydrophobicity

- The active phase can be recovered easily from spent catalysts by burning away the carbon support
- Carbon supports are usually cheaper than conventional catalyst supports

3.3.2 Carbon nanotubes as a catalytic support

Carbon nanotube and carbon nanofiber (CNF) supported particles find a wide variety of application in various fields other than catalysis (as mentioned in section 3.1). Figure 3.3 illustrates the various elements which have been deposited on carbon materials as a result. The more extensively studied carbon supported catalysts stem from the precious metal group (e.g. Pt and Pd) due to the application of these catalysts in the fine chemical industry [12]. In addition to this, Pt and Pt-Ru supported CNTs have found application in fuel cell electrocatalysis [13]. Along with monometallic, bimetallic and trimetallic particles, oxides, semimetals, nitrides, phosphides, sulphides, selenides and tellurides and hydrides have been supported on CNTs [4].

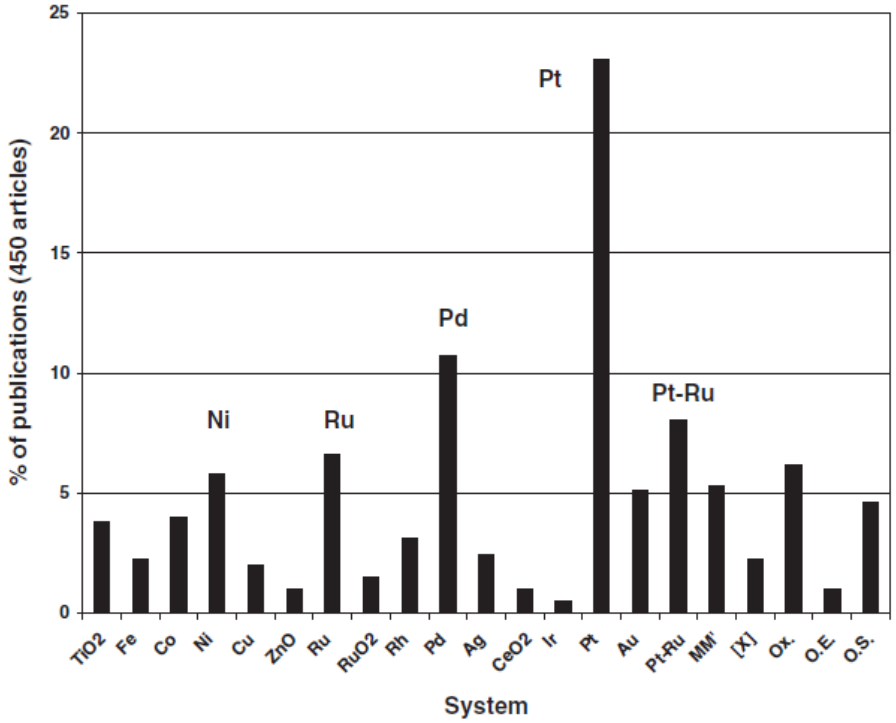

Figure 3.3: Elements that have been deposited on CNTs or CNFs. MM´ bimetallic systems; [x] molecular complexes; Ox. oxides; O.E. other elements; O.S. other systems [4].

Surface functionalisation, which is the creation of active groups on the CNT surface, is essential in order to attain a high dispersion of the active phase. Most commercially available CNTs do not contain a large number of functional groups on their surface. In these cases the metal anchoring sites available are the defects which may exist on the material surface [14]. As a result, a poor distribution of the metal is achieved and it is not possible to attain high metal loadings in such cases [11]. Due to the broad spectrum of applications for CNTs, many reliable methods have been developed for their chemical and electrochemical functionalisation [15]. The most common methods of CNT functionalisation are:

- Acid oxidation [16]
- Gas-phase oxidation (air [16] or CO_2 [17])
- Oxidation by common oxidising agents (e.g. hydrogen peroxide [16], permanganate [18], ozone [19], osmium tetroxide [20])
- The use of polymeric additives [21]
- Ball-milling [22-23]
- Sonication [24]

These methods of functionalisation can also modify the hydrophilicity of the support and the reducibility of the precursor. For example HNO_3 acid treated CNTs are hydrophilic, whereas untreated CNTs are hydrophobic [6]. This difference becomes important in liquid phase reactions as the properties of the support can be tailored accordingly [6]. Therefore the method of functionalisation chosen strongly affects the surface chemistry and structural features on the CNT. Functionalisation is most commonly carried out by treatment with HNO_3 or HNO_3/H_2SO_4 which introduces surface oxygen functionalities at the defect sites on the outer and sometimes inner walls [16,25-27]. Refluxing with acids introduces, by means of oxidation, carbonyl and other oxide groups as well as carboxylic and anhydride groups [16]. The HNO_3/H_2SO_4 treatment has been known to create a higher density of carboxylic acid surface groups with a concentration as high as 1.4 oxygen containing surface groups per square nanometer measured by chemical titration in the case of oxidised CNTs [6]. However prolonged refluxing may induce the opening of MWCNT tips, damage the walls and slightly increase the surface area [6]. Treatment with H_2SO_4 has been known to induce sulphur containing species on the surface of MWCNTs as demonstrated by XPS analysis [28]. Reports have shown that sonication of MWCNTs in HNO_3/H_2SO_4 at 333 K have introduced carbonyl, ester and phenol groups, with the addition of a few carboxylic groups as determined

by infrared spectroscopy [28]. However, the introduction of a large number of functionalities can negatively affect the mechanical and electronic properties of the material and prolonged sonication may lead to fragmentation and mechanical damage of the tubes [6]. Rao et al. have experimented with, and compared, other oxidative treatments for MWCNT functionalisation such as aqua regia, HF-BF_3, aqueous OsO_4 and $KMnO_4$ solutions [29]. It was observed that the above treatments open the nanotubes while preserving the essential structural features. The advantage found with the HF-BF_3 and OsO_4 treatments was that the reactions could be carried out at room temperature [29].

CNT supported catalysts have been synthesised by various chemical methods including incipient wetness impregnation, ion exchange, chemical vapour deposition, organometallic grafting, impregnation with colloidal solutions, deposition precipitation as well as electrochemical techniques [7,30]. Optimal metal dispersions on these supports are obtained using CNFs, followed by MWCNTs and then SWCNTs. The reason for this ranking is the peculiar orientation of the graphene layers in CNTs, which provide potential anchoring sites for the metal. Furthermore SWCNTs are arranged in bundles and it is therefore difficult to get a good distribution of metal anchoring [7]. Metal-support interactions play a vital role in metal anchoring as high dispersions are achieved with Ru and Pt, whereas Ni, Co and Pd give rise to larger particles [7].

Chemical vapour deposition (CVD) and electrode deposition are two methods which have been adopted for the synthesis of CNT based catalysts. CVD is known to produce well dispersed catalysts, however the method is not without its limitations [31]. If the synthesis is conducted in two successive steps it results in low metal loadings. Secondly, it is difficult to scale up since deposition must be carried out in a fluidised bed and CNTs are difficult to fluidise without external activation such as vibration [32].

Electrode deposition is a process which produces metal particles by reduction of a metal salt solution at a cathode. The limitations with this method are the difficulty in controlling the metal loading due to the concurrent reduction of protons and in reaching small particle sizes [13].

3.4 Carbon nanotubes as a catalyst

Although fewer reports exist on the use of CNTs as catalysts, a few pioneering works worth mentioning are: the report on methane decomposition by Muradov [33], the oxidative dehydrogenation of ethylbenzene to styrene by Maskimova and co-workers [34-37],the ODH of propane to propene by Sui et al. [38], the oxidation of *p*-toluidine [39] and the conversion of aniline to azobenzene [40] by Croston et al.

As the study reported in this thesis focuses on the oxidative dehydrogenation of *n*-octane, further mention will be made on the ODH of ethylbenzene to styrene and propane to propene. Based on the pioneering work by Iwasawa [41] and Alkhazov [42] on the performance of activated carbons for the oxidative dehydrogenation of ethylbenzene (ODE), Pereira et al. studied the catalytic activity of CNTs in the ODE reaction [43]. This study compared MWCNTs, before and after different oxidative treatments and hence possessing different surface groups, to activated carbon and graphite. It was found that not only were the MWCNTs active catalysts for ODE but they also showed the highest specific activity per initial surface area and were the most stable under oxidative conditions as compared to all catalysts tested. However, activated carbon was found to show the best overall performance. Oxidation treatments with HNO_3 (liquid phase) and O_2 (gas phase) increased the amount of oxygenated surface groups, whilst preserving the textural and structural features. Furthermore, oxidation with O_2 was found to also increase the specific surface area due to the opening of the MWCNTs which improved the selectivity to styrene (see Table 3.2). Interesting to note was that the performance of the mentioned catalysts improved with coke deposition, which could be explained by the fact that coke is in itself active towards the ODE reaction [44].

Sui et al. tested carbon nanofibers (CNF) and CNF-supported phosphoric oxides for the ODH of propane to propene [38]. Note the difference between CNTs and CNFs is that CNFs lack a hollow cavity. It was found that the CNF itself is an effective catalyst for the ODH of propane with 42.6 % propene selectivity achieved at 5.33 % propane conversion at 400°C. Higher yields can only be achieved at higher reaction temperatures (> 450°C), however higher temperatures cause CNF gasification. CNF-supported phosphoric oxides can operate at higher temperatures (up to 525°C) without gasification. The introduction of phosphoric oxides to the CNF was found to decrease the catalytic activity, however the catalyst can

operate at 500°C without gasification and inhibits propane over-oxidation to COx. A 39.63 % propene selectivity was achieved at 42.1 % propane conversion at 500°C over 5 wt % CNF-supported phosphoric oxides [38].

Table 3.2: Steady state results for the ODE of ethylbenzene to styrene [43]

Catalyst	**% X**	**% $S_{styrene}$**
MWCNT (untreated)	19.6	59.2
MWCNT (treated with HNO_3)	19.7	55.4
MWCNT (treated with O_2)	27.6	67.5
Activated carbon	49.9	82.5
Graphite	0.6	55.0

3.5 References

[1] Reich, S., Thomsen, C., Maultzsch, J., *Carbon Nanotubes: Basic concepts and physical properties*; Wiley-VCH Weinheim, 2004.

[2] Harris, P.J.F., *Carbon Nanotube Science: Synthesis, properties and applications*; Cambridge University Press: New York, 2009.

[3] Endo, M., Iijima, S., Dresselhaus, M.S., *Carbon Nanotubes*, Elsevier Science Limited: New York, 1996.

[4] Serp, P., Figueiredo, J.L., *Carbon Materials for Catalysis*, John Wiley & Sons: New Jersey, 2009.

[5] Rodriguez-Reinoso, F. *Porosity in Carbons: Characterisation and Applications*, Edward Arnold: London, 1995.

[6] Bitter, J. H., Murzin, D.Y., *Nanocatalysis*, Research Signpost: Kerela, India, 2006.

[7] Bacsa, R., Serp, P. *Carbon Metatubes*; Wiley: Weinheim, Germany, 2009.

[8] Ehrburger, P., *Advanced Colloid Interface Science*, 1984, **21**, 275.

[9] Rodriguez-Reinoso, *Carbon*, 1998, **36**, 159.

[10] Pham-Huu, C., Ledoux, M.J., *Topics in Catalysis*, 2006, **40**, 49.

[11] Serp, P., Corrias, M., *Applied Catalysis A: General*, 2003, **253**, 337.

[12] Auer, E., Freund, A., Pietsch, J., Tacke, T., *Applied Catalysis A: General*, 1998, **173**, 259.

[13] Lee, K., Zhang, J., Wang, H., Wilkinson, D.P., *Journal of Applied Electrochemistry*, 2006, **36**, 507.

[14] Yang, S. H., Shin, W.H., Lee, J.W., Kim, S.Y., Woo, S.I., Kang, J.K., , *Journal of Physical Chemistry*, 2005, **110**, 13941.

[15] Tasis, D., Tagmatarchis, N., Bianco, A., Prato, M., *Chemical Reviews*, 2006, **106**, 1105.

[16] Ros, T.G., van Dillen, A.G., Geus, J.W., Koningsberger, D.C., *Chemistry - A European Journal*, 2002, **5**, 1151.

[17] Zhao, N., He, C., Jiang, Z., Li, J., Li, Y., *Materials Letters*, 2007, **61**, 681.

[18] Sathishkumar, B. C., Govidaraj, A., Mofokeng, G., Subbanna, G., Rao, C.N., *Journal of Physics B*, 1996, **29**, 4925.

[19] Agrawal, S., Raghuveer, M.S., Li, H., Ramanath, G., *Applied Physics Letters*, 2007, **90**, 193104.

[20] Banerjee, S., Wong, S.S., *Journal of the American Chemical Society*, 2004, **126**, 2073.

[21] Li, W., Gao, C., Quian H., Ren, J., Yan, D., *Journal of Materials Chemistry*, 2006, **16**, 1852.

[22] Maurin, G., Stepanek, I., Bernier, P., Colomer, J.F., Nagy, J.B., Henn, F., *Carbon*, 2001, **39**, 1273.

[23] Pierard, N., Fonseca, A., Konya, Z., Willems, I., van Tendeloo, G., Nagy, J.B., *Chemical Physics Letters*, 2001, **335**, 1.

[24] Xing, Y., Li, L., Chusuei, C.C., Hull, R.V., *Langmuir*, 2005, **21**, 4185.

[25] Kusnetzova, A., Popova, I., Yates, T.J., Bronikowski, M.J., Huffman, C.D., Liu, J., Smalley, R.E., Hwu, H.H., Chen, J.G., *Journal of American Chemical Society*, 2001, **123**, 10699.

[26] Kyotani, T., Nakazaki, S., Xu, W.H., Tomita, A., *Carbon*, 2001, **39**, 771.

[27] Toebes, M. L., van Heeswijk, J.P.M., Bitter, J.H., van Dillen, A.J., de Jong, K.P., *Carbon*, 2004, **42**, 307.

[28] Liu, Z., Lin, X., Lee, J.Y., Zang, W., Han, M., Gan, L.M., *Langmuir*, 2002, **18**, 4054.

[29] Satishkumar, B. C., Govindaraj, A., Mofokeng, G., Subbanna, G.N., Rao, C.N.R, *Journal of Physics B*, 1996, **29**, 4925.

[30] Georgakilas, V., Gournis, D., Tzitzios, V., Pasquato, L., Guldi, D.M., Prato, M., *Journal of Materials Chemistry*, 2007, **17**, 2679.

[31] Serp, P., Kalck, P., Feurer, R., *Chemical Reviews*, 2002, **102**, 3085.

[32] Xia, W., Schluter, O.F.K., Liang, C., van der Berg, M.W.E., Guraya, M., Muhler, M., *Catalysis Today*, 2005, **102**, 34.

[33] Muradov, N., *Catalysis Communications*, 2001, **2**, 3.

[34] Maskimova, N., Mestl, G., Schlögl, R., *Studies in Surface Science and Catalysis*, 2001, **133**, 383.

[35] Maskimova, N., Raddatis, V., Mestl, G., Ledoux, M., Schlögl, R., *Eurasian Chemico-Technological Journal*, 2000, **2**, 231.

[36] Mestl, G., Maskimova, N.I., Keller, N., Raddatis, V.V., Schlögl, R., *Angewandte Chemie International Edition*, 2001, **40**, 2066.

[37] Keller, N., Maskimova, N.I., Roddatis, V.V., Schur, M., Mestl, G., Butenko, Y.V., *Angewandte Chemie International Edition*, 2002, **41**, 1885.

[38] Sui, Z., Zhou, J., Dai, Y., Yuan, W., *Catalysis Today*, 2005, **106**, 90.

[39] Croston, M., Langston, J., Sangoi, R., Santhanam, K.S.V., *International Journal of Nanosciences*, 2002, **1**, 277.

[40] Croston, M., Langston, J., Takacs, G., Morrill, T.C., Miri, M., Sanatham, K.S.V., *International Journal of Nanosciences*, 2002, **1**, 285.

[41] Iwasawa, Y., Nobe, H., Ogasawara, S., *Journal of Catalysis*, 1973, **31**, 444.

[42] Alkhazov, T. G., Lisovoskii, A.E., Ismailov, Y.A., Kozharov, A.I., *Journal of Catalysis*, 1978, **19**, 482.

[43] Pereira, M. F., Figueiredo, J.L., Orfao, J.J., Serp, P., Kalck, P., Kihn, Y., *Carbon*, 2004, **42**, 2807.

[44] Pereira, M. F. R., Orfão, J.J.M., Figueiredo, J.L., *Applied Catalysis A: General*, 1999, **184**, 153.

Chapter 4: Experimental

4.1 Introduction

Nickel molybdate, carbon nanotubes and carbon nanotube supported nickel molybdate were the catalysts tested for the activation of *n*-octane. This chapter details the synthesis methodology used for nickel molybdate and the CNT supported nickel molybdate, as well as the functionalisation of the CNT support. The characterisation techniques used for the bulk and surface analysis of the catalysts are described, as well as the set up of the fixed-bed plug-flow reactor. The qualitative and quantitative analysis of the oxidation products from the reactor was carried out by GC-FID and GC-TCD, the details of which are also described.

4.2 Catalyst preparation

The chemicals used are detailed in Appendix 1.

4.2.1 Synthesis of nickel molybdate

Co-precipitation was used as the modus operandi for the synthesis of nickel molybdate (refer to Figure 2.1). The catalyst precursor was prepared by modifying the method reported by Mazzocchia et al. [1]. Equimolar solutions of nickel and molybdenum were prepared by dissolving $Ni(NO_3)_2.6H_2O$ (14.5 g in 100mL) and $(NH_4)_6Mo_7O_{24}.4H_2O$ (8.83 g in 100 mL) in deionised water. The solutions were then added drop wise, at a constant rate, to a round bottom flask fitted with a magnetic stirrer and heated in an oil bath. The pH of the stirred solution was carefully monitored and maintained at 5.6 by adding either NH_4OH or HNO_3. The temperature was maintained at 43°C whilst the metal solutions were being added and thereafter increased to 85°C. The resulting precipitate was filtered hot under suction using a Buchner funnel and dried in an oven at 110°C for 12 hours.

4.2.2 Catalyst activation

The catalyst precursor was calcined at 550°C in airflow for 2 hours, to obtain the bright yellow α-$NiMoO_4$. The calcined catalysts were pelletized and sieved to a particle size of 300-600μm. The β-$NiMoO_4$ was generated *in situ* by heating the α-$NiMoO_4$ in the reactor to 720°C in air and maintaining the temperature for 10 minutes before cooling to 300°C.

4.3 Carbon nanotubes

The carbon nanotubes were commercially available and multi walled in structure. Functionalisation of the nanotubes was necessary prior to their use as a catalytic support.

4.3.1 Functionalisation of carbon nanotubes

The carbon nanotubes were functionalised by refluxing in 55 % nitric acid at 110°C for 6 hours, after which time the nanotubes were filtered and dried in an oven at 110°C for 12 hours. This method was adapted from that reported by Keyser and Prinsloo [2]. The functionalised nanotubes were lightly crushed using a pestle and mortar and stored in a desiccator.

4.3.2 Method of preparation of supported catalyst

The supported catalyst NM-CNT was prepared using three different methodologies; Homogeneous deposition precipitation (HDP), wet impregnation and co-precipitation. It is worth mentioning that the supporting of a stoichiometric α-$NiMoO_4$ catalyst on MWCNTs is, to our knowledge, novel and thus different approaches were explored.

(a) Homogeneous deposition precipitation (HDP)

The supported catalyst was prepared by modifying the HDP method as described by Keyser and Prinsloo [2]. Functionalised carbon nanotubes (f-CNT) were sonicated in deionised water for 45 minutes in order to improve homogeneity. A mass of 0.0160 g of α-$NiMoO_4$ and

0.0442 g of urea was added to the stirred suspension of f-CNTs in 100 mL of deionised water. The suspension was heated to 95°C in a 250 mL 3-neck round bottom flask fitted with a pH meter and thermometer. A series of experiments were carried out in which the pH was monitored and controlled by adding either acid (HNO_3) or base (NH_4OH) in order to determine the effect of pH on metal loading. The solid catalyst was filtered off under suction using a Buchner funnel and dried in an oven at 110°C for 12 hours.

(b) Wet impregnation

The wet impregnation method used was adapted from the method reported by Pawelec et al. [3]. The nickel molybdate catalyst was synthesised as described in Section 4.2.1. A mass of $NiMoO_4$ was added to 50 mL of deionised. A mass of f-CNTs (twice the mass of $NiMoO_4$) was added to 100 mL of deionised water. Both the $NiMoO_4$ and f-CNT suspensions were sonicated for 45 minutes to induce homogeneity before mixing together. The resulting mixture was fitted with a magnetic stirrer and gently heated to and maintained at 85°C for a 14 hour period. Aliquots of the mixture were removed every hour, the solid catalyst filtered off under suction using a Buchner funnel and dried in an oven at 110°C for 12 hours.

(c) Co-precipitation

The co-precipitation method described in Section 4.2.1 was adapted for the preparation of the supported catalyst [1]. Equimolar solutions of nickel and molybdenum were prepared by dissolving $Ni(NO_3)_2.6H_2O$ (13.6 g in 25 mL) and $(NH_4)_6Mo_7O_{24}.4H_2O$ (2.21 g in 25 mL) in deionised water. Functionalised CNTs (twice the mass of $NiMoO_4$ theoretically expected from the catalyst synthesis after calcination) were sonicated in 50 mL of deionised water for 45 minutes. The slurry of CNTs in deionised water was thereafter transferred to a round bottom flask and heated to 43°C. The metal solutions of nickel and molybdenum were added drop wise, at a constant rate, to the stirred suspension of CNTs. The pH of the stirred suspension was carefully monitored and maintained at 5.6 by adding either NH_4OH or HNO_3. On completion of addition of the metal solutions the suspension was heated to 85°C. The resulting precipitate was filtered at 85°C and dried in an oven at 110°C for 12 hours. The supported catalyst precursor was calcined at 550°C in airflow for 2 hours, to obtain the supported catalyst hereafter referred to as NM-CNT.

4.4 Catalyst Characterisation

4.4.1 Inductively Coupled Plasma - Optical Emission Spectroscopy (ICP-OES)

The bulk composition of the catalysts was determined by ICP-OES on a Perkin Elmer Precisely, Optical Emission Spectrometer, Optima 5300 DV.

(a) Nickel molybdate

The instrument was first calibrated by analysing multi elemental standards of nickel and molybdenum prepared by diluting a 1000 ppm standard solution to the required calibration range of 0-100 ppm. The standards were diluted with deionised water and matrix matching was accounted for by the addition of 5 mL 32 % HCl to each standard.

The samples were prepared by digesting 0.02 g of the catalyst in a volume of 5 mL 32 % HCl in a beaker on a hotplate. The digested sample was diluted in a 100 mL volumetric flask with deionised water.

(b) Supported catalysts

Similarly to 4.4.1 *(a)* the supported catalyst was digested, however prior to dilution of the sample the CNTs were filtered off using gravity filtration. The filtrate sample was diluted in a 100 mL volumetric flask with deionised water. The CNTs filtered off were analysed by SEM-EDX and TEM to analyse for residual metals.

4.4.2 X-Ray Diffraction (XRD)

Powder and *in situ* X-ray diffraction (XRD) patterns were recorded on a Bruker D8 Advance diffractometer operated at 40 kV and 40 mA. The source of radiation was Cu Kα (wavelength 1.5406 Å). The 2θ covers the range between 5 and 90 degrees at a speed of one degree per minute with a step size of 0.02 degrees. Powder samples were analysed at room temperature in static air. *In situ* samples were analysed in the temperature range of 30°C-600°C, at a ramp

rate of 0.2 °C/min. The *in situ* reduction experiments were carried out under a flowing stream of 5 % H_2 in N_2 (30 mL/min) whereas the *in situ* re-oxidation was carried out under a flowing stream of air (30 mL/min). All data was manipulated using Eva software. Employing the full width at half maximum of the highest intensity peak, the average crystallite size was calculated using the Scherrer equation.

4.4.3 Attenuated Total Reflectance Infrared Spectroscopy (ATR-IR)

The infrared spectra were recorded at room temperature using a Perkin Elmer Spectrum 100 FT-IR Spectrometer fitted with a Universal ATR Sampling Accessory. A small amount of the powder sample was placed on top of the ATR crystal (composite of zinc selenide and diamond) and a pressure of about 120 Gauge was applied to allow for better contact between the sample and the crystal.

4.4.4 Brunauer-Emmett-Teller (BET) surface area and pore volume analysis

The BET surface areas and pore volume were measured by nitrogen physisorption isotherms at 77 K (liquid nitrogen) using the standard multipoint method (eleven points) on a Micromeritics Gemini instrument. Prior to the analysis samples were degassed in a stream of nitrogen at 200°C for 24 hours. The instrument calculated the surface area and pore volume as a function of the mass of the degassed catalyst.

4.4.5 Thermal Gravimetric Analysis Differential Scanning Calorimetry (TGA-DSC)

TGA analyses were conducted on a Perkin Elmer SDT Q600 instrument. A mass of 5-10 mg of sample was placed in a platinum crucible which was heated from 10°C to 1000°C at a rate of 10°C/min under static air. The catalyst weight loss as a function of temperature was monitored.

4.4.6 Scanning Electron Microscopy (SEM)

Scanning electron microscopy (SEM) images were obtained using a LEO 1450 Scanning Electron Microscope. Samples for SEM images were coated with gold using a Polaron SC Sputter Coater or carbon coated using a JEOL JEE 1C vacuum evaporator (all CNT based samples were gold coated). Backscattered SEM images were obtained using the JEOL JSM 6100 microscope and backscattered detector. Elemental analysis was obtained using a Bruker detector and Esprit 1.8 software.

4.4.7 Transmission Electron Microscopy (TEM)

Transmission electron microscopy (TEM) images were taken on a Jeol JEM 1010 Transmission Electron Microscope operated at a voltage of 100 kV. Samples were prepared by deposition of a small amount of the catalyst between two formvar coated copper grids and the images were captured with MegaView III Soft Imaging System.

4.4.8 Temperature Programmed Reduction (TPR)

Temperature Programmed Reduction was carried out on a Micromeritics AutoChem II 2920 automated catalyst characterisation system. The sample analysis was performed by passing over a reducing gas, 5% hydrogen in argon at a flow rate of 30 mL/min, over 50 mg of the catalyst at ambient temperature. The temperature of the sample was raised linearly at 5°C/min to 900°C whilst the hydrogen consumption was monitored.

4.5 Catalyst testing

4.5.1 Reactor configuration

The oxidative activation of *n*-octane, in the gas phase, was carried out in a plug-flow, fixed-bed reactor. The reactor design is based on previous research and has been modified and reconstructed to suit the scope of this project [4]. Figure 4.1 details the flow diagram of the

reactor setup. The liquid feed of *n*-octane was pumped into the system, using an isocratic HPLC pump and gasified at 180°C before being mixed with the oxidant (air) and diluent (nitrogen). The gaseous mixture was then passed through a heated stainless steel fixed bed reactor tube packed with the catalyst at the hottest spot and void spaces filled with inert carborandum (SiC). The catalyst bed was held in position at the hottest spot and separated from the carborandum by means of a glass wool plug. The products from the reactor were allowed to condense in the sampling cylinder which was cooled to 1°C. The liquid samples collected were separated into an organic and aqueous layer and individually injected into the Gas Chromatograph – Flame Ionisation Detector (GC-FID). The non-condensable gaseous products were passed to a Ritter wet gas flow meter which measured the total flow rate of the gaseous products and allowed for quantification. The gaseous samples were injected into the Gas Chromatograph – Thermal Conductivity Detector (GC-TCD) and GC-FID for qualitative and quantitative analysis. A control panel was used to monitor the flow rates of the gases (air and nitrogen) as well as the heating of the feed line and reactor tube. The precise temperature inside the reactor tube was controlled and monitored using a sliding thermocouple which was situated at the hottest spot during the catalytic runs. The pressure inside the reactor was monitored using a pressure gauge and a pressure relief valve was used to vent and relieve pressure inside the reactor in case of pressure build up.

4.5.2 Product characterisation techniques

A Perkin Elmer Precisely, Clarus 400 Gas Chromatograph (GC) equipped with a thermal conductivity detector (TCD) was used to separate and quantify carbon oxides produced in the reaction. The GC was fitted with a 50 m long Carboxen 106 PLOT column with a 0.53 mm internal diameter. The detector was set at 250°C, while the injector and TCD filament temperature were set at 150°C. The helium carrier gas flowed through the column at a pressure of 60 kPa. A Perkin Elmer Clarus 500 GC equipped with a flame ionisation detector (FID) was used to separate and quantify hydrocarbons produced in the reaction. The GC was fitted with a 50 m long PONA column having a 0.2 mm internal diameter. The detector was set at 300°C, whilst the injector was set at 250°C. The hydrogen carrier gas was set at a pressure of 300 kPa. A Perkin Elmer GM-MS equipped with auto sampler using a PONA SGE 50 m x 0.15 mm column and helium as the carrier gas was used to identify any

unidentified hydrocarbons in the reaction. All liquid products were analysed for the water content using a Metrohm 870 KF Titrino Plus Karl Fischer Titrator.

The temperature programmes used for the GC-TCD and GC-FID and GC-MS are illustrated in Appendix 2.

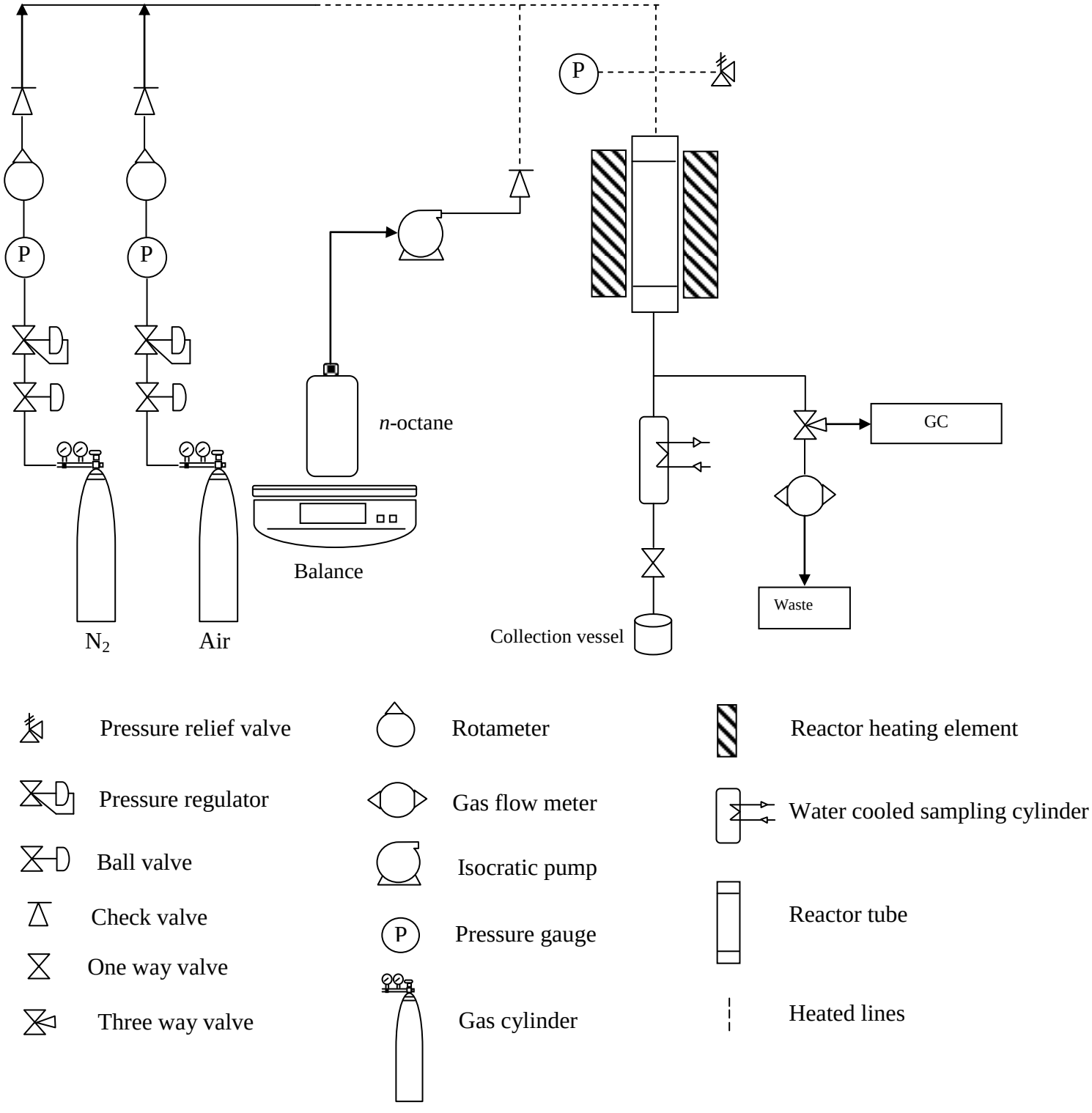

Figure 4.1: Flow diagram of the reactor set-up

4.5.3 Reactor conditions

The reactions were performed at atmospheric pressure using a 9 mm id x 35 cm long stainless steel fixed-bed continuous-flow reactor. A volume of 0.5 mL (approximately 0.7 g) of catalyst, having particle sizes in the range of 300 – 600 μm, was loaded in the hottest spot of the reactor tube, which was determined by probing different positions inside the reactor tube using a thermocouple. The catalyst packing length was approximately 1 cm. The void spaces within the reactor were filled with coarse 24 gritt (14755/24 = 615 microns) carborandum (SiC). General operating conditions included; a temperature range of 250-500°C, octane/O_2 ratio of 2 and nitrogen dilution of 89 %. A new reaction was started and fresh NM catalyst loaded for each temperature tested. The β-$NiMoO_4$ was generated in situ (refer to section 4.4.2). Note that the β-phase of the supported catalyst could not be tested as the CNTs are not stable at the high temperature which is needed to generate the β-phase. Each catalyst was maintained on stream for 24 hours and a steady state was achieved for the first 12 hours on stream for the catalyst NM-A. The gaseous and liquid products were sampled every 2 hours. Table 4.1 illustrates the parameters used for all reactions. The carbon balance, for all data points used, was between 95-105 % and each point was replicated in duplicate.

Refer to Appendix 2 for the details of the calculation used for product quantification.

Table 4.1: Reaction parameters used for catalytic testing

Catalyst	[a]GHSV(h^{-1})	Temp (°C)	% Total N_2	*n*-octane gas flow ($mL.min^{-1}$)	Air Flow ($mL.min^{-1}$)	Total Flow ($mL.min^{-1}$)
Carborandum	2500	250-500	89.2	3.0	7.2	41.7
Carborandum	4000	250-500	89.8	4.5	10.8	105.1
Carborandum	7500	250-500	87.4	10.5	25.1	125.0
α-NM	2500	250-500	89.2	3.0	7.2	41.7
α- NM	4000	250-500	89.8	4.5	10.8	105.1
α-NM	7500	250-500	87.4	10.5	25.1	125.0
β-NM	4000	300	89.8	4.5	10.8	105.1
CNT	4000	250-500	89.8	4.5	10.8	105.1
α-NM-CNT	4000	250-500	89.8	4.5	10.8	105.1

[a]GHSV (h^{-1}) = Total flow of gaseous reactants into reactor ($mL.h^{-1}$) / volume of catalyst (mL)

4.6 References

[1] Mazzocchia, C., Del Rosso, R., Centola, P., *Anales de Quimica*, 1983, **79**, 108.

[2] Keyser, M.M., Prinsloo, F.F., *Studies in Surface Science and Catalysis*, 2007, **163**, 45.

[3] Pawelec, B., La Parola, V., Navarro, R.M., Murcia-Mascaros, S., Fierro, J.L.G., *Carbon*, 2006, **44**, 84.

[4] Friedrich, H. B., Mahomed, A. S., *Applied Catalysis A: General*, 2008, **347**, 11.

Chapter 5: Characterisation Results and Discussion

5.1 Introduction

The chemical and textural structure of a catalyst can significantly influence the catalytic behaviour with regards to activity and selectivity to certain products. In order to study the physiochemical properties of the catalyst, detailed characterisation was carried out. The main focus of this project is the synthesis and characterisation of supported nickel molybdate catalysts for the catalytic oxidative dehydrogenation of *n*-octane. This chapter details the characterisation results of: nickel molybdate catalysts; carbon nanotubes and supported nickel molybdate on carbon nanotubes.

5.2 Nickel molybdate

This section will discuss the characterisation results obtained for the nickel molybdate catalysts ($NiMoO_4$). The stoichiometric α-phase is referred to as NM-A. The nickel molybdates with a Ni:Mo ratio less than one and greater than one are referred to as NM-B and NM-C, respectively.

5.2.1 Inductively Coupled Plasma-Optical Emission Spectroscopy (ICP-OES)

The stoichiometric catalyst which has a Ni:Mo ratio of 1:1 consists purely of the catalytically active α-phase. The synthesis parameters of pH, concentration of reacting solutions and precipitation and filtration temperature, need to be carefully controlled in order to form the precursor to the α-phase (refer to section 2.2, Figure 2.1) [1-2]. The precipitation pH of 5.6 is known to be the crucial parameter which must be maintained throughout the synthesis. The metal concentrations of three catalysts determined by ICP are compared in Table 5.1. The metal ratios of these catalysts indicate that pH is not the only parameter that controls the catalyst stoichiometry. Precipitation temperature must be carefully controlled in order to obtain a catalyst with a metal ratio of one. In this case it was found that the precipitation

temperature must be maintained at 43°C whilst the metal solutions are being added and thereafter increased to 85°C for the aging and filtration processes. In addition, the rate at which the metal solutions are added is of vital importance to ensure that neither an excess of nickel or molybdenum precipitate out in the precursor. Catalyst NM-B has a Ni:Mo ratio of 0.56 and therefore consists of an excess of molybdenum. This excess of molybdenum precipitates out as MoO_3. Catalysts NM-C has a Ni:Mo ratio of 1.2 and contains an excess of nickel which precipitates out as NiO. In both cases, the pH was maintained at 5.6, however the precipitation temperature differed. The stoichiometric α-nickel molybdate, catalyst NM-A, was obtained at a precipitation pH of 5.6 and temperature of 43°C. The precipitation temperature of 43°C differs from that given in literature of 85°C [2].

Table 5.1: Elemental composition of NM catalysts (ICP) and synthesis parameters

Catalyst	Ni/Mo	Colour	Precipitation temp (°C)	Filtration temp (°C)	pH
NM-A precursor	0.98	Light yellow	43	85	5.6
NM-A	1.0	Bright yellow	43	85	5.6
NM-B	0.56	Green	85	85	5.6
NM-C	1.2	Yellow-green	85	85	5.6

5.2.2 Attenuated Total Reflectance-Infrared Spectroscopy (ATR-IR)

FTIR analysis of the catalysts allows one to gain an insight into the functional groups present within the material which is then used to infer the phases present [3]. The IR spectrum of the NM-A precursor (Figure 5.1) shows the peaks at 814 cm^{-1} and 826 cm^{-1} which are allocated to MoO_3 [4] . The peaks at 1427 cm^{-1} and 1618 cm^{-1} are allocated to unreacted ammonium heptamolybdate; the peaks at 450 cm^{-1} and 721 cm^{-1} are assigned to nickel hydroxide and the

ammonium nitrate respectively [5]. These peaks are no longer observed in the spectrum of the NM-A catalyst. This is due to the solid-state reaction that occurs during calcination. When the precursor is heated to 550°C during calcination, the unstable phases are lost as volatile material by sublimation. This leaves behind the more stable form of the precursor material that is the catalyst. This change in the phase between the precursor and catalyst brings about the distinct structural differences seen in the x-ray diffractograms and SEM images. The reaction temperature at which the catalyst was tested, therefore, did not exceed the calcination temperature of 550°C. The characteristic peaks representative of α-$NiMoO_4$ are observed for the NM-A catalyst, at 580 cm^{-1}, 930 cm^{-1} and 950 cm^{-1}.

The spectra of the non-stoichiometric catalysts (NM-B and NM-C), shown in Appendix 3, show bands at 812 cm^{-1} and 880 cm^{-1} which are allocated to MoO_3, whereas the bands at 930 cm^{-1} and 950 cm^{-1} are due to the α-$NiMoO_4$ phase. This is expected as these catalysts consist of a mixed phase nickel molybdate, MoO_3 (NM-B) and metallic nickel (NM-C). The vibrations of the O_2^{2-} ions are noted between 800 and 900 cm^{-1}[4].

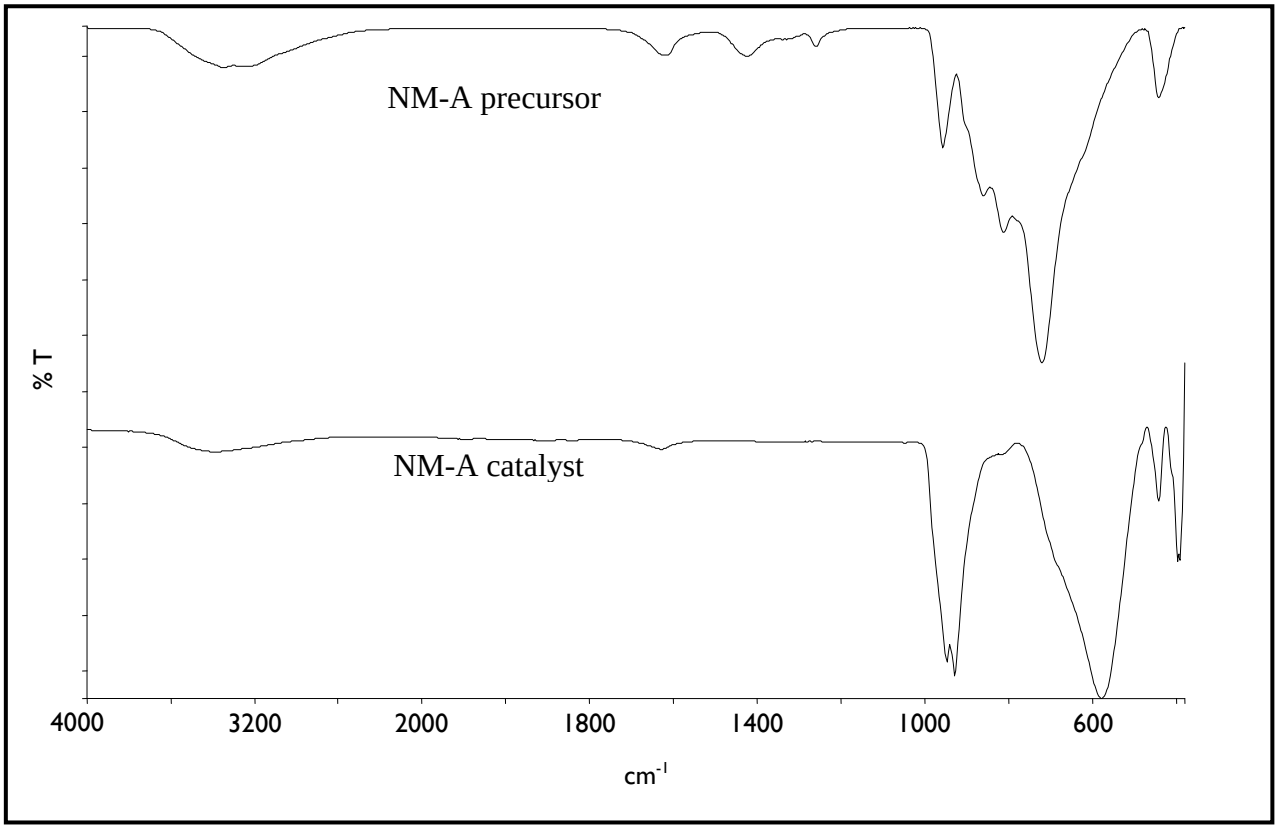

Figure 5.1: IR spectrum of NM-A pre and post calcination

5.2.3 Raman Spectroscopy

The bands, for catalyst NM-A, at 961 cm^{-1} and 913 cm^{-1} have been assigned to the symmetric and asymmetric stretching modes of the terminal Mo-O bond and the band at 706 cm^{-1} has been attributed to the Ni-O-Mo symmetric stretch (Table 2.5). Figure 5.2 displays the Raman spectra of all 3 catalysts. Catalyst NM-C which contains an excess of nickel presents new bands at 800 cm^{-1} and 880 cm^{-1}. Catalyst NM-B which contains an excess of molybdenum contains bands characteristic of MoO_3 at 670 cm^{-1}, 882 cm^{-1} and 998 cm^{-1} [4].

Table 5.2: Raman peak allocations of various nickel molybdate catalysts

Catalyst	Raman bands (cm^{-1})	Phases
NM-A	913 s	$NiMoO_4$
	961 vs	$NiMoO_4$
	706 s	$NiMoO_4$
NM-B	670 s	MoO_3
	822 vs	MoO_3
	998 s	MoO_3
NM-C	800, 880	NiO

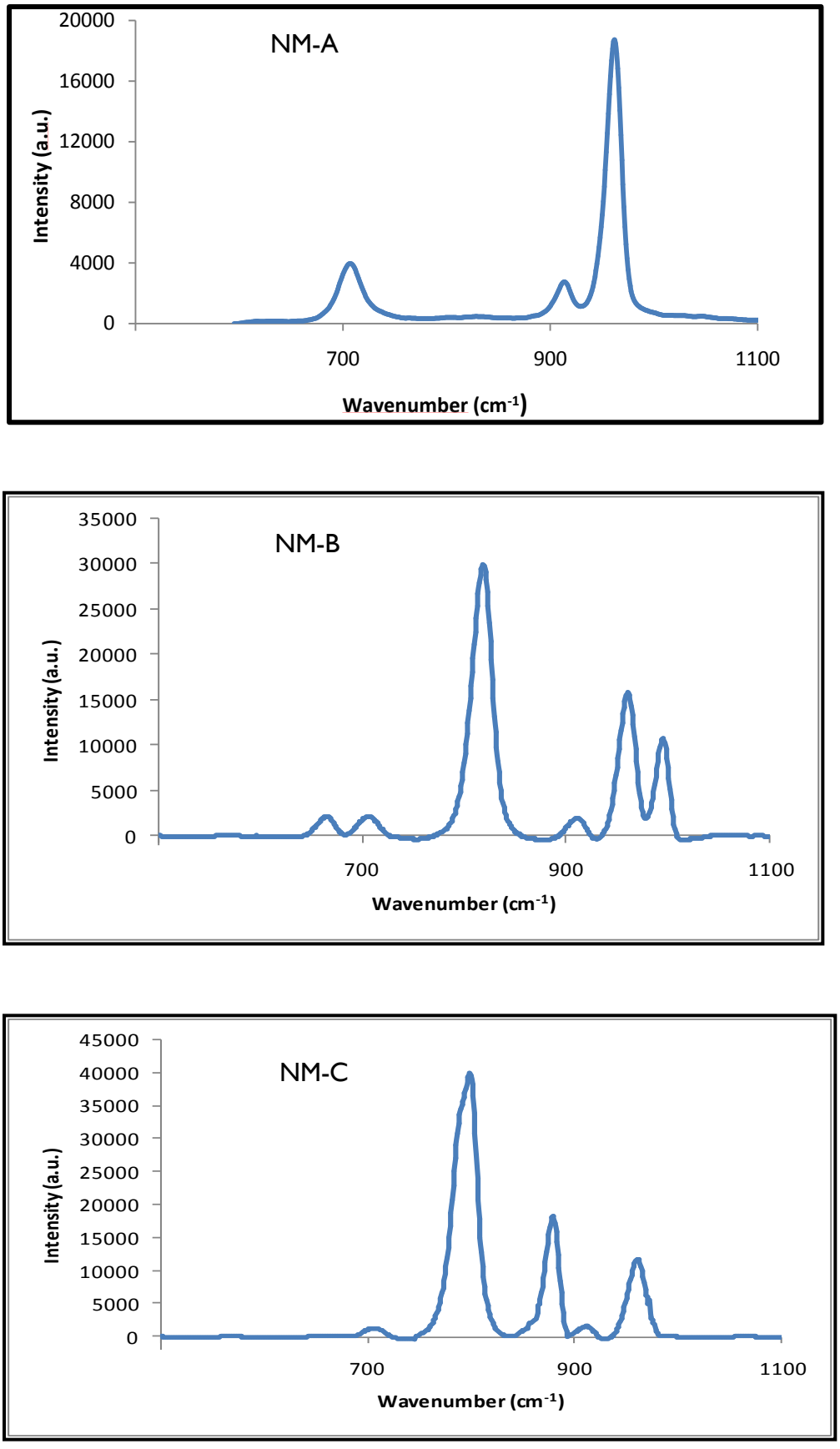

Figure 5.2: Raman Spectra of nickel molybdate catalysts

5.2.4 Powder X-ray Diffraction (XRD)

X-ray diffraction patterns were used to determine the phase composition of the catalysts. The d-spacings of all catalysts were compared to JCPDS cards 33-948, 45-01142, 5-508 and 4-835 for α-$NiMoO_4$, β-$NiMoO_4$, MoO_3 and NiO, respectively. The diffractogram of the precursor to catalyst NM-A displayed in Figure 5.3 show two major peaks at 2θ = 26.8° and 29.5° which is allocated to the presence of a metallomolybdate salt $NH_4(NiMoO_4)_2OH{\cdot}H_2O$ [6]. The peaks observed in the diffractogram of NM-A at 2θ = 14.2°, 25.5°, 29.6°, 33.0°, 38.8° and 41.4°, 43.9°, 47.5°, 53.0°, 56.1°, 58.2° and 62.0° are characteristic of α-$NiMoO_4$. The sharp intense peaks are indicative of the crystalline nature of the catalyst [7]. The peaks observed for catalyst NM-B shown in Figure 5.4 are assigned to both the α-$NiMoO_4$ and the MoO_3 (2θ = 12.5°, 25.8°, 27.2°, 29.0°, 33.9°, 46.50° and 48.20°) phases suggesting excess molybdenum in the catalyst is present as the MoO_3 phase. The XRD pattern of catalyst NM-C is similar to that of NM-B and therefore contains both the α-$NiMoO_4$ and MoO_3 phases, in addition to the presence of metallic nickel which is represented by the peaks at 2θ = 14.2 and 25.20.

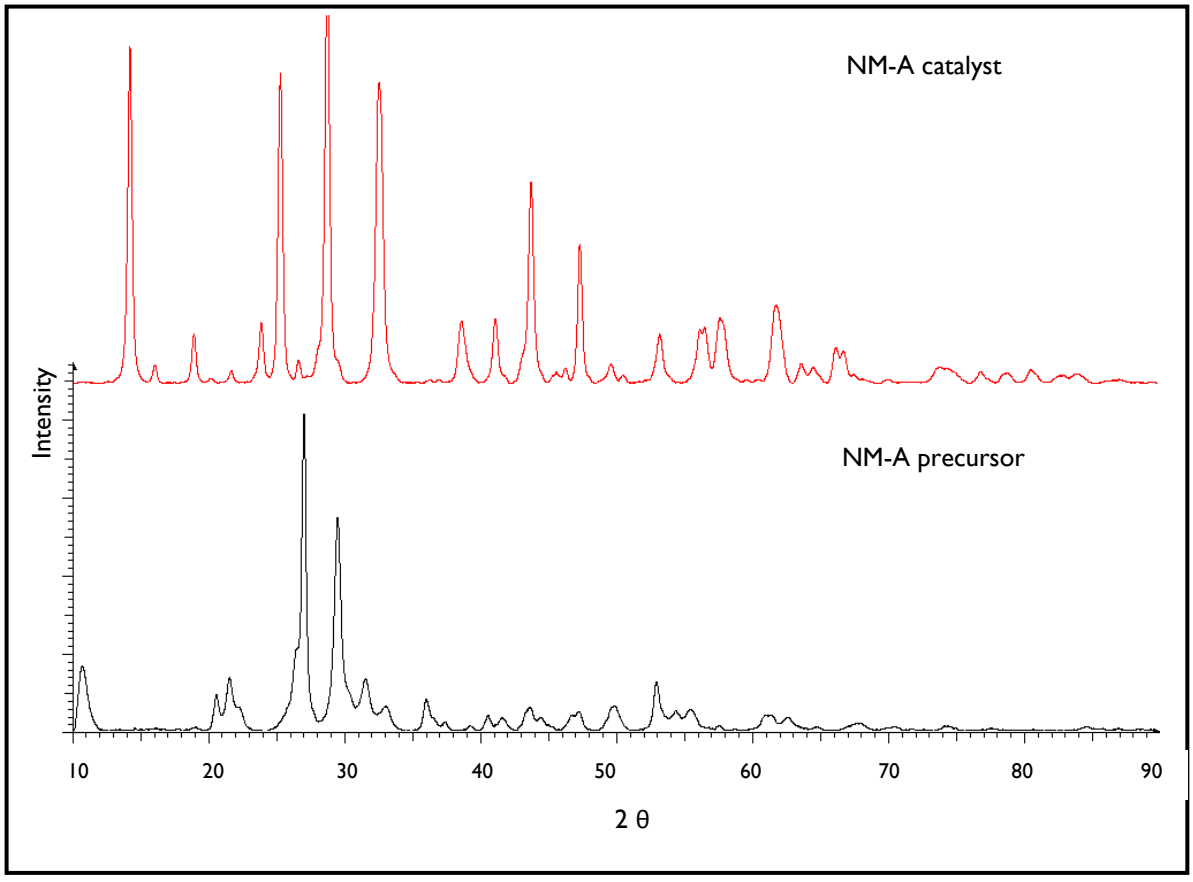

Figure 5.3: X-ray diffractograms of NM-A catalyst and precursor

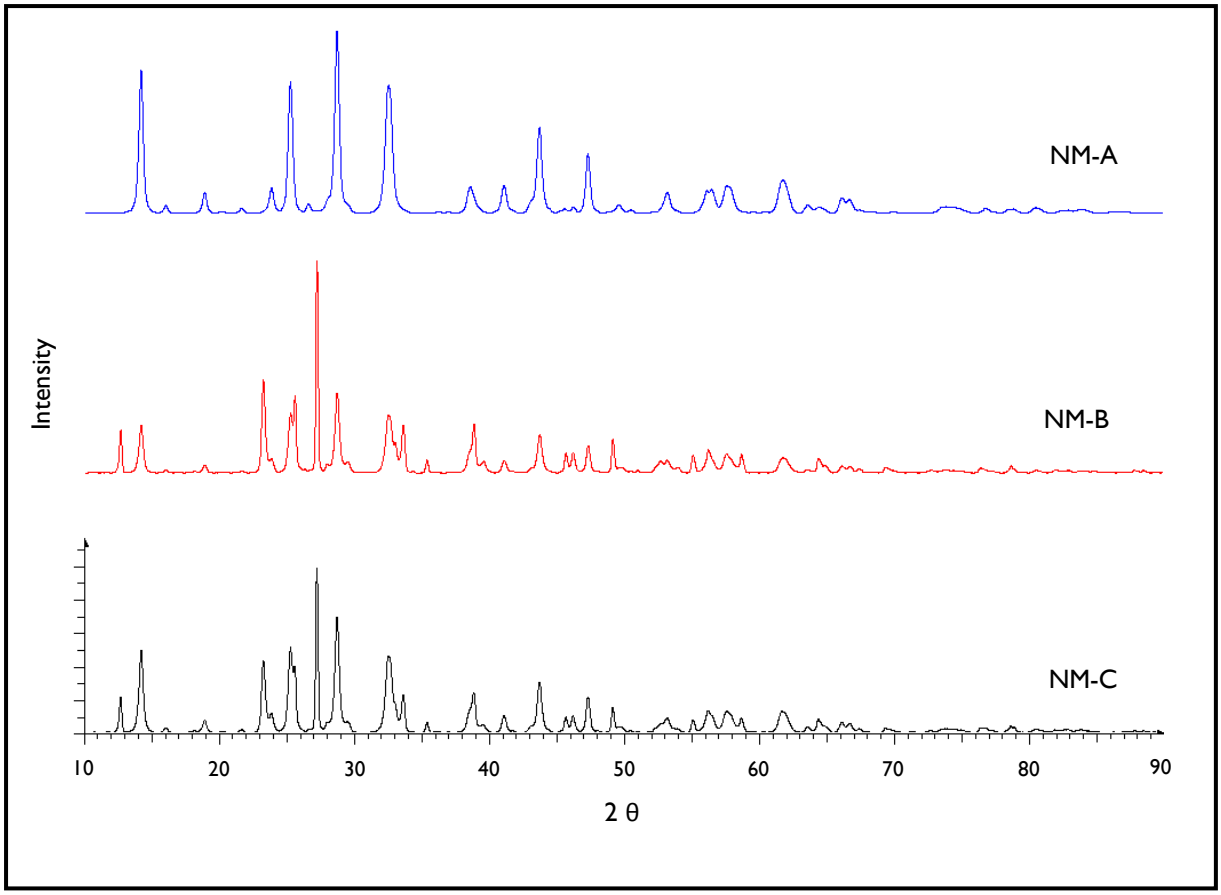

Figure 5.4: X-ray diffractograms of catalysts NM-A, NM-B and NM-C

5.2.5 *In situ* X-ray Diffraction (*In situ* XRD)

In situ x-ray diffraction was carried out on NM-A in order to gain insight on the thermal phase transformations which take place within the catalyst. It has been well established that nickel molybdate exists as two ploymorphs. The α-phase, stable at room temperature, has a monoclinic crystal structure whereby the molybdenum is octahedrally coordinated. Upon heating to 720°C the catalysts is converted to the metastable β-phase (or high temperature phase) whereby the molybdenum is tetrahedrally coordinated. The β-phase, on cooling, is stable to a temperature of 200°C and any further decrease in temperature results in the phase transition of β to α-phase [8]. *In situ* studies were first carried out in air. There was no observable phase transformation for temperatures up to 600°C. The reason for this is that the α→β-phase transformation takes place in air at 720°C. This phase transformation could not be seen in air due to the temperature limitation of the Anton Paar cell of 600°C. The *in situ*

experiment was repeated under hydrogen gas in order to create a reducing atmosphere to try and reproduce, in reasonable proximity, the conditions experienced by the catalyst within the reactor. The catalyst within the reactor under experimental conditions is reduced by the feed (*n*-octane) and the feed is in turn oxidised to the various products. The observed phase change (Figure 5.4) begins to transpire between 500-600^{o}C. The peaks at 2θ = 38.8° and 65.1° are allocated to MoO_2 and metallic nickel. The peaks at 2θ = 43.8° and 76.0° are allocated to metallic nickel and the peak at 52.0° to MoO_2. Re-oxidation of the reduced catalyst in air (Figure 5.8) results in an onset of change in phase at 300°C and at 600°C pure β-phase is present, illustrated by the characteristic XRD pattern having major peaks at 2θ = 25.4°, 26.6°, 27.8°, 29.0°and 33.0° (JCPDS card 45-01142) [7]. Note all *in situ* diffractograms are stacked in order of temperature increasing from bottom to top. The first diffractogram at the bottom is at room temperature, the second from the bottom is at 100°C and the temperature increases in 50° increments to 600°C (last at the top).

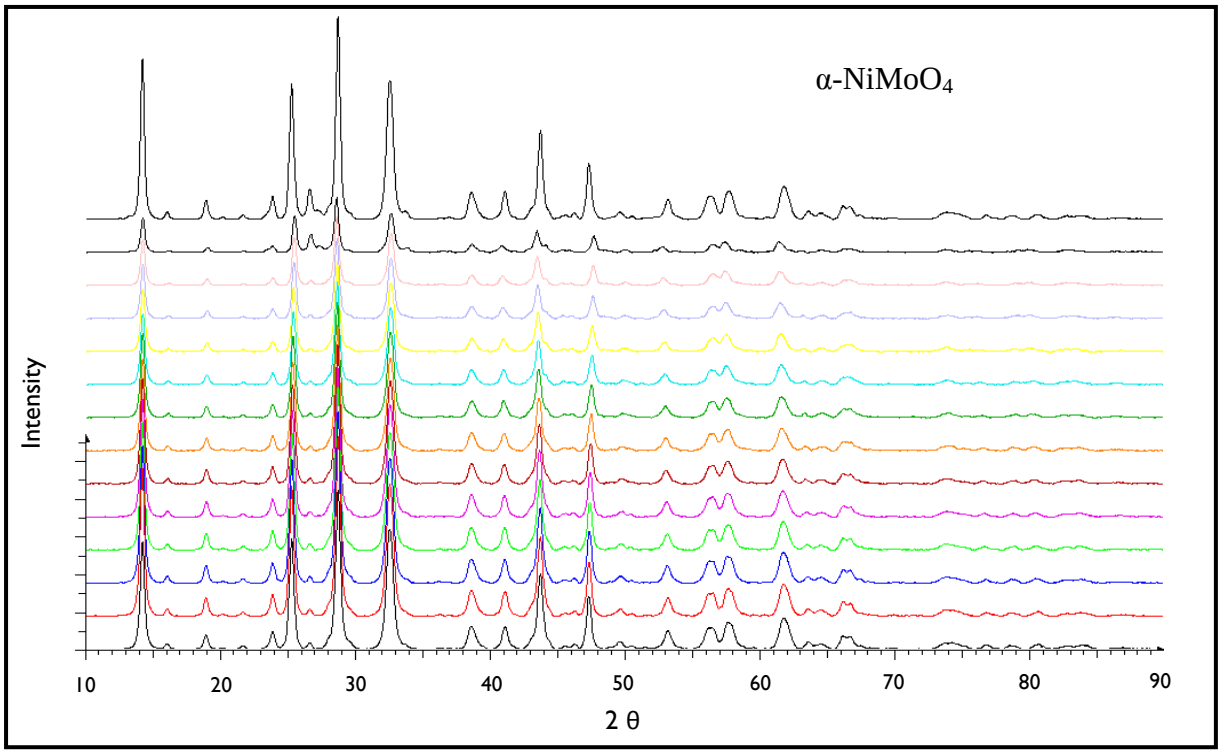

Figure 5.5: *In situ* x-ray diffractogram of NM-A heated in air

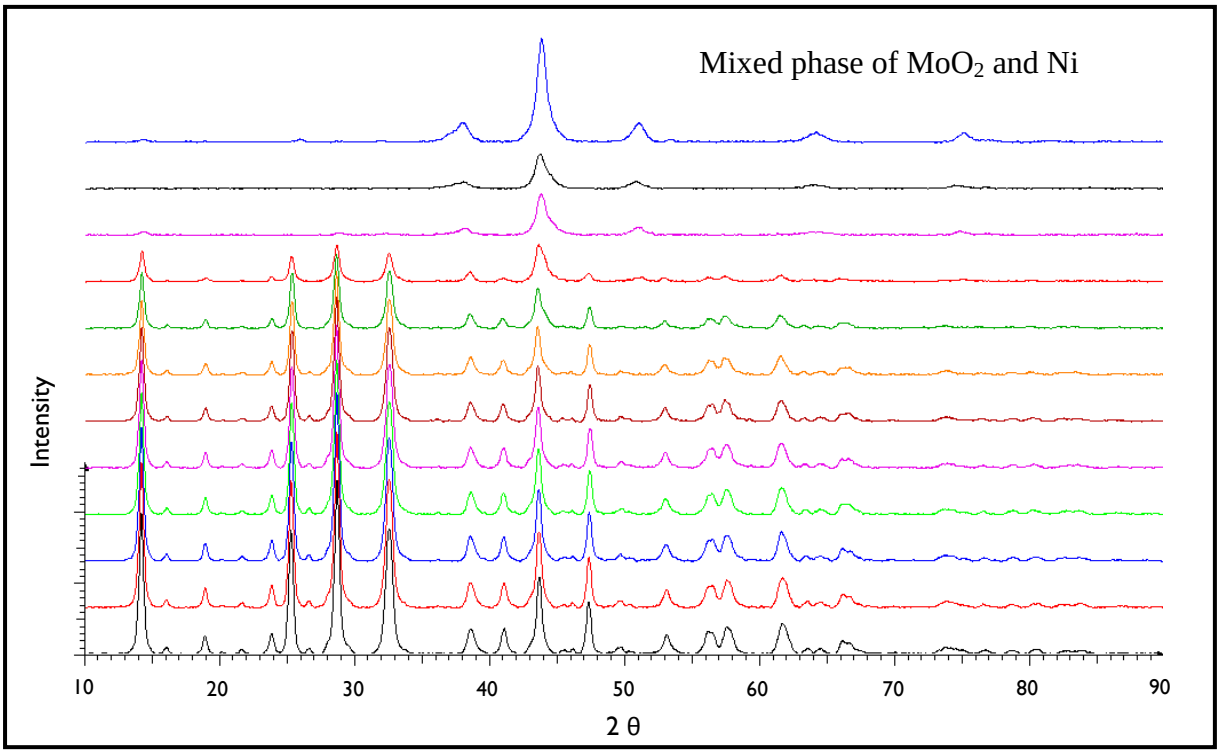

Figure 5.6: *In situ* x-ray diffractogram of NM-A reduced under hydrogen

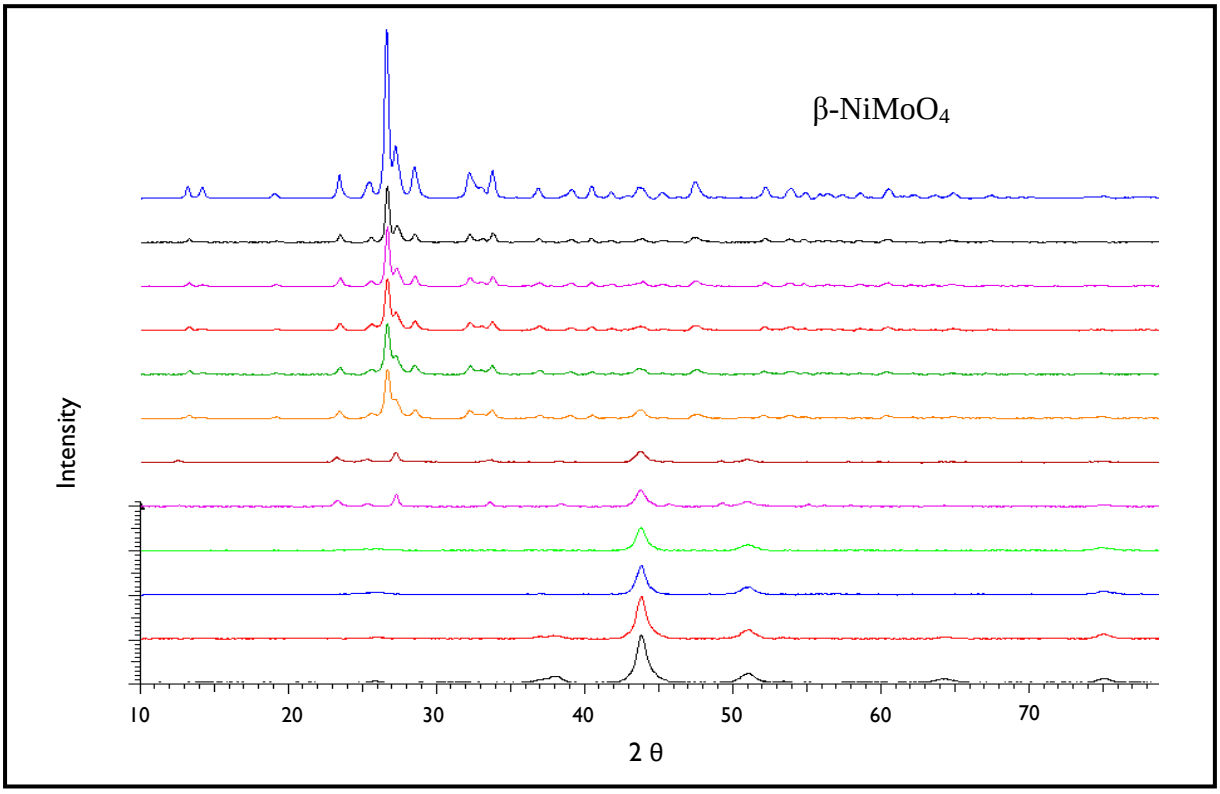

Figure 5.7: *In situ* x-ray diffractogram of NM-A re-oxidised in air

5.2.6 Brunauer-Emmet-Teller surface analysis (BET) and Scanning Electron Microscopy (SEM)

The chemical composition of the catalysts strongly affects the surface area and there is a direct relationship between the two parameters as can be seen from the results represented in Table 5.3. The BET surface area of catalyst NM-A is 45 m^2/g which is within the expected range for stoichiometric α-$NiMoO_4$ of 37- 46 m^2/g [9]. A pore volume of 0.25 cm^3/g was obtained. It can be concluded from this result that the catalyst is porous in nature. This porosity can be seen in the SEM image of NM-A (Figure 5.10) which shows the catalyst surface to consist of rounded sponge-like particles. The surface area of catalyst NM-B is 28.8 m^2/g which is considerably lower than that of NM-A (Figure 5.8). This decrease in surface area is attributable to the excess molybdenum in the catalyst which exists as MoO_3. Molybdenum trioxide has a low surface area of 3 m^2/g therefore the presence of the MoO_3 phase results in a decrease in surface area of the catalyst. Similarly, the surface area of catalyst NM-C is considerably lower at 26.6 m^2/g. This is due to the excess nickel in the catalyst present as NiO. NiO has a low surface area of 5 m^2/g and therefore the presence of this phase lowers the surface area of the catalyst [9]. The lower pore volumes of 0.17 and 0.12 obtained for catalysts NM-B and NM-C, respectively, correspond with the lower surface area obtained. This is expected as the structure of these catalysts differ from the porous catalyst NM-A (discussed in the subsequent pages).

The crystallite size of the catalysts was calculated, using the Scherrer equation, from the full width at half maximum of the highest intensity peak obtained from the x-ray diffractogram. The results are represented in Table 5.3 and a correlation between crystallite size and surface area can be drawn; as the surface area of the catalysts increase the crystallite size decreases.

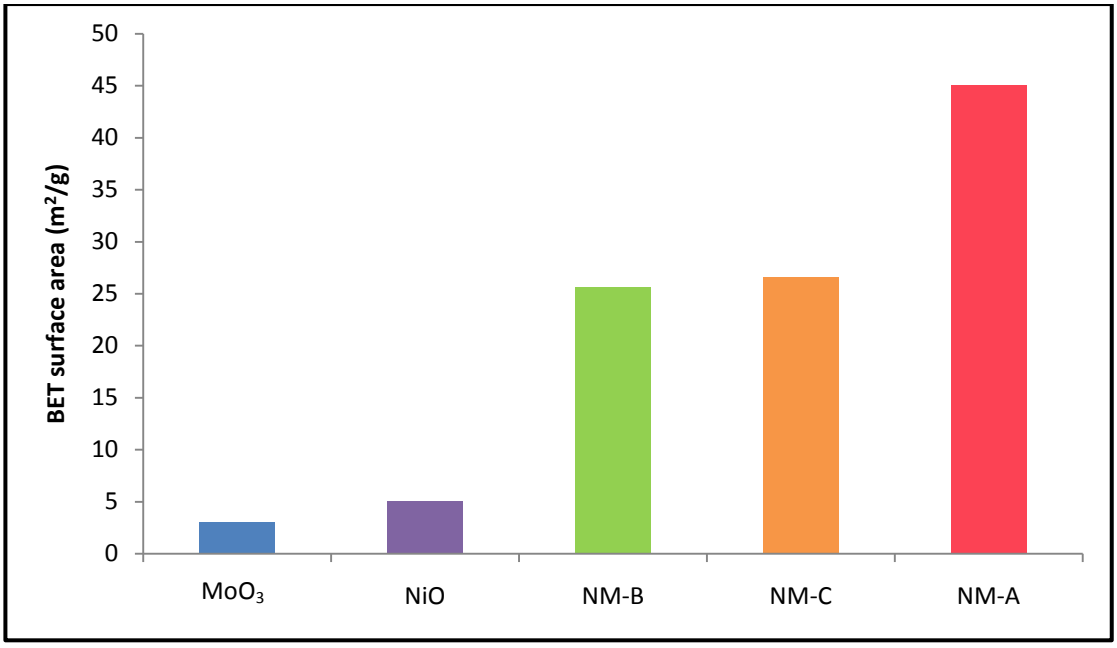

Figure 5.8: BET surface areas of various catalysts

Table 5.3: Comparison of BET surface areas and XRD crystallite size

Catalyst	BET surface area (m^2/g)	BET pore volume (cm^3/g)	[a]XRD crystallite size (nm)
NM-A precursor	40.2	0.20	20.1
NM-A	42.7	0.25	19.3
NM-B	28.8	0.17	37.8
NM-C	26.6	0.12	39.9

[a]*Calculated using the Scherrer equation from FWHM of highest intensity peak*

As mentioned above, scanning electron micrographs show the surface of the stoichiometric α-phase (Figure 5.10 c) to consist of rounded porous sponge-like particles. The SEM-EDX images illustrate the distribution of molybdenum, mapped in red, and nickel mapped in green (Figure 5.10 d and e respectively). The superimposed image (Figure 5.10 f), which is essentially yellow, show neither metal to exist in excess and depicts a homogeneous metal distribution on the catalyst surface. This correlates with the ICP results which found the ratio of nickel to molybdenum to be 1:1 confirming the catalyst composition to be pure homogeneously dispersed α-phase. The surface structure of NM-B (Figure 5.9 a) consists of well defined hexagonal shaped particles which are characteristic of MoO_3 [9]. SEM-EDX results show molybdenum to be in excess in an average weight of 12 %. The results differ from ICP as EDX is a surface analysis technique whereas ICP is a bulk analysis technique. It can therefore be deduced that there exists a small percentage of excess molybdenum clustered on the catalyst surface. This conclusion is supported by the backscattered SEM images, which show heavier elements to appear brighter and lighter elements to appear darker in shade. Fig 5.9 b displays backscattered SEM image of NM-B which shows the excess molybdenum in the catalysts to be distributed as metal clusters on the surface. The surface of NM-C (Figure 5.10 a) consists of rigid sharp edged particles which are either square or rectangular in shape. The excess of nickel present in the catalysts can be observed on the surface from the SEM-EDX image (Figure 5.10 b), which displays nickel in green. It can be concluded that the BET surface area and pore volume results correlate with the XRD crystallite size and are supported by the SEM surface morphology.

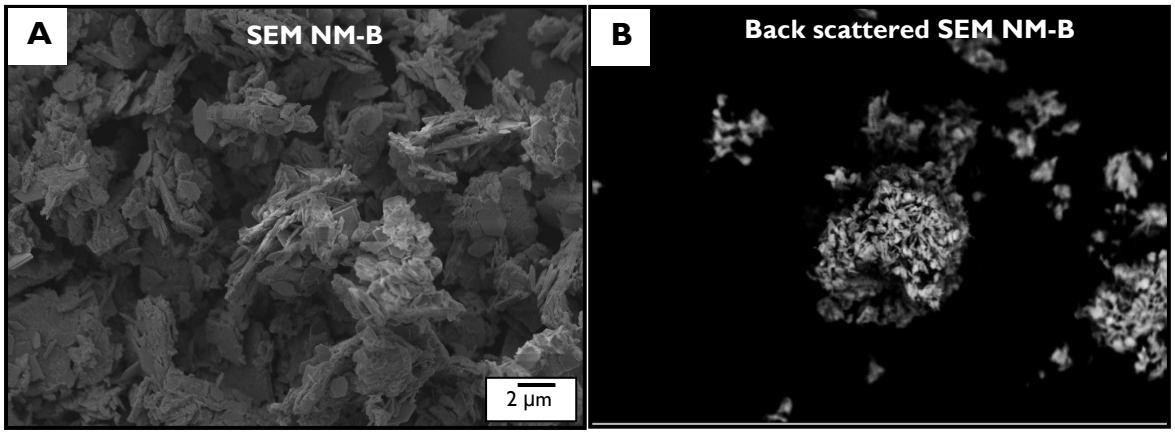

Figure 5.9: SEM image and backscattered SEM image of NM-B

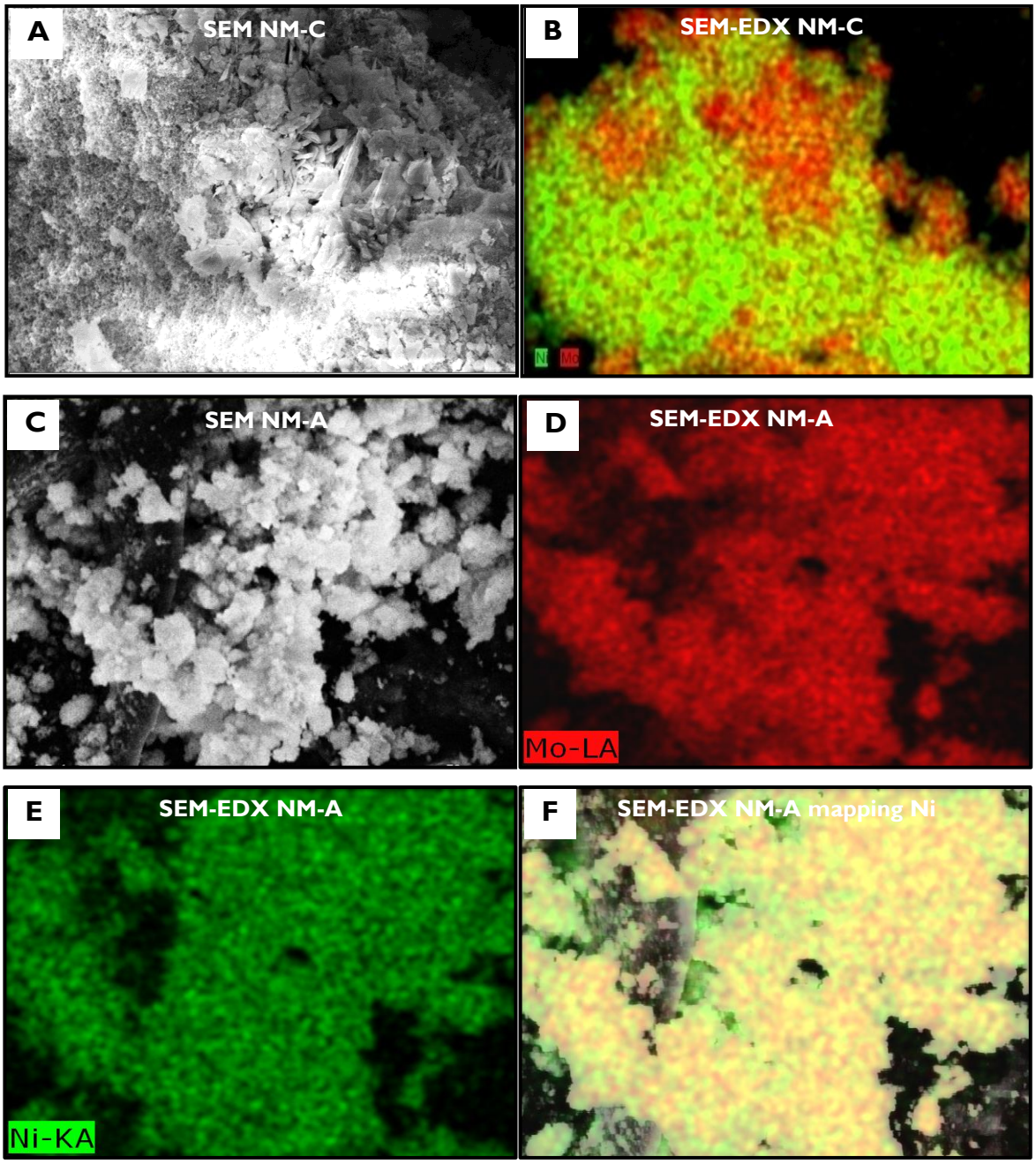

Figure 5.10: SEM image and SEM-EDX mapping of NM-A and NM-C

5.2.7 Transmission Electron Microscopy (TEM)

The TEM image of NM-A (Figure 5.11 a) shows the catalyst to consist of elongated rod-like particles. The selected area electron diffraction (SAED) pattern (Figure 5.11 b) consists of a series of spots which radiate outwards to form a spotted circular pattern. This spotted pattern is indicative of the crystalline nature of the catalyst which is in accordance with the sharp intense peaks of the x-ray diffractogram. The structure of NM-B (Figure 5.12 a) has a clearly different morphology consisting of small rounded particles, whereas NM-C (Figure 5.12 c) consists of small rounded particles which agglomerate to form elongated particles. The electron diffraction pattern of NM-B (Figure 5.12 b) consists of ordered spots which lie parallel to each other as the diffraction occurred on a singular orientated particle, whereas the pattern of NM-C (Figure 5.12 d) is more randomly orientated due to the overlap of particles which result in a compound diffraction pattern. All three diffraction patterns, though they may appear slightly different due to the orientation of the particles, provide the same information i.e. the catalysts are crystalline.

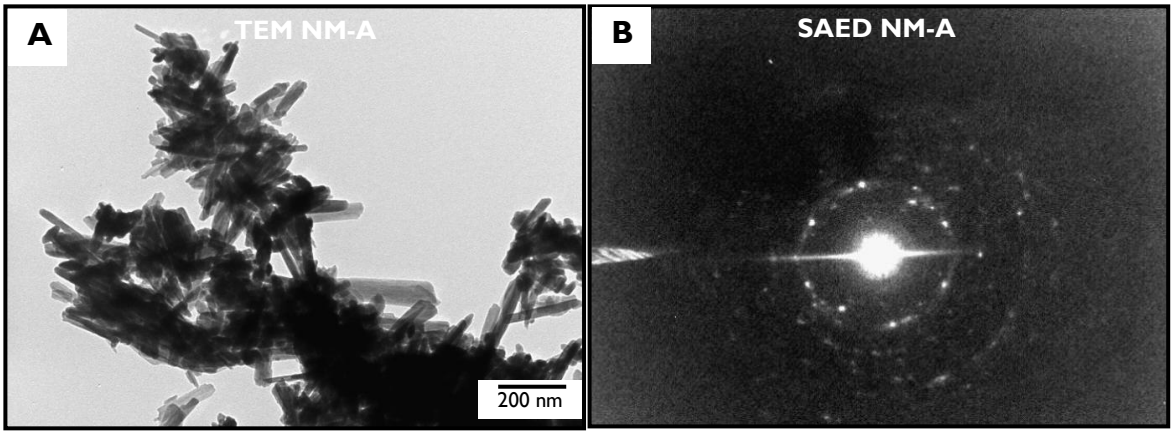

Figure 5.11: TEM images and SAED of catalysts NM-A

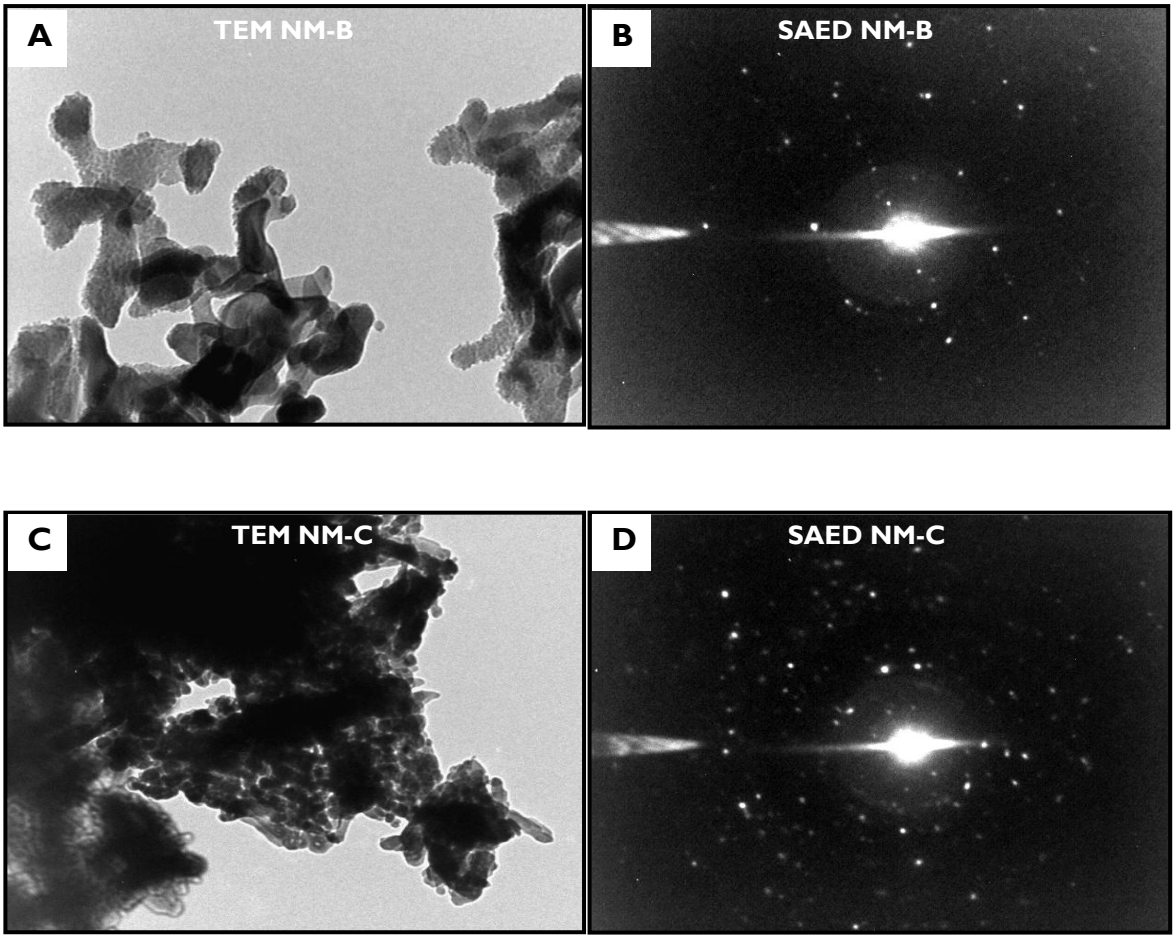

Figure 5.12: TEM images and SAED of catalysts NM-B and NM-C

5.2.8 Thermogravimetric Analysis (TGA) and Differential Scanning Calorimetry (DSC)

The curve for uncalcined NM-A (Figure 5.13) shows two weight losses between the temperature ranges of 200°C to 450°C. The first weight loss of 3.37 % occurs at around 256°C and is attributed to loss of adsorbed water and ammonia on the catalyst surface. The second exothermic weight loss of 2.06 % occurs at 446°C is attributed to the decomposition of $NH_4(NiMoO_4)_2OH.H_2O$ and ammonium nitrate in the structure [10]. There are clear differences in the thermal transitions of the calcined catalysts displayed in Figure 5.14 as opposed to the uncalcined. Firstly and most prominently, there is no observable weight loss, which is expected as the volatile components are removed on calcination. The catalyst was

calcined at 550°C to remove water and volatile components in the structure such as ammonium and nitrate ions, therefore the two weight losses which occur for the uncalcined catalyst (in the region 200°C to 500°C) will not be seen. Secondly, there is an endothermic peak at 580°C which is attributed to the α to β phase transformation [10]. Conversely, on cooling, the exothermic peak at 200°C is attributed to the β to α transformation. This is in accordance with the phase transition, seen in the *in situ* XRD diffractogram at 550°C (Figure 5.22).

Note that all TGA-DSC samples were run in static air as detailed in section 4.4.5.

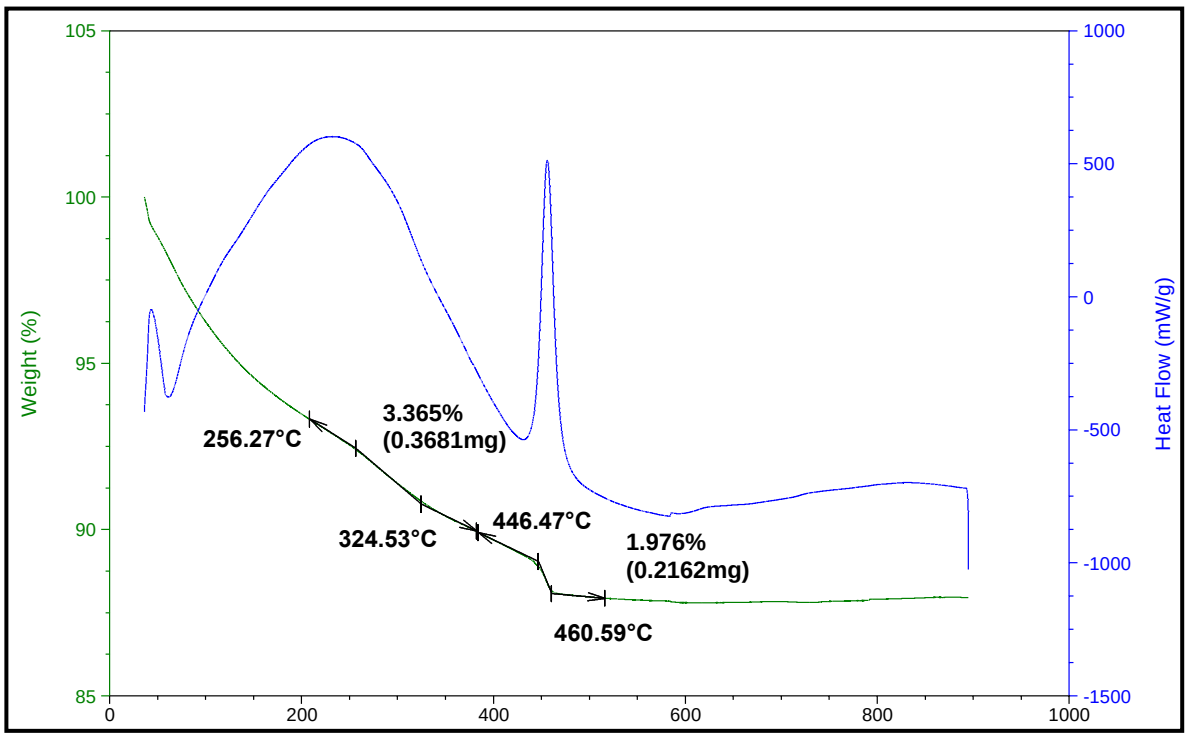

Figure 5.13: TGA-DSC curve of uncalcined NM-A

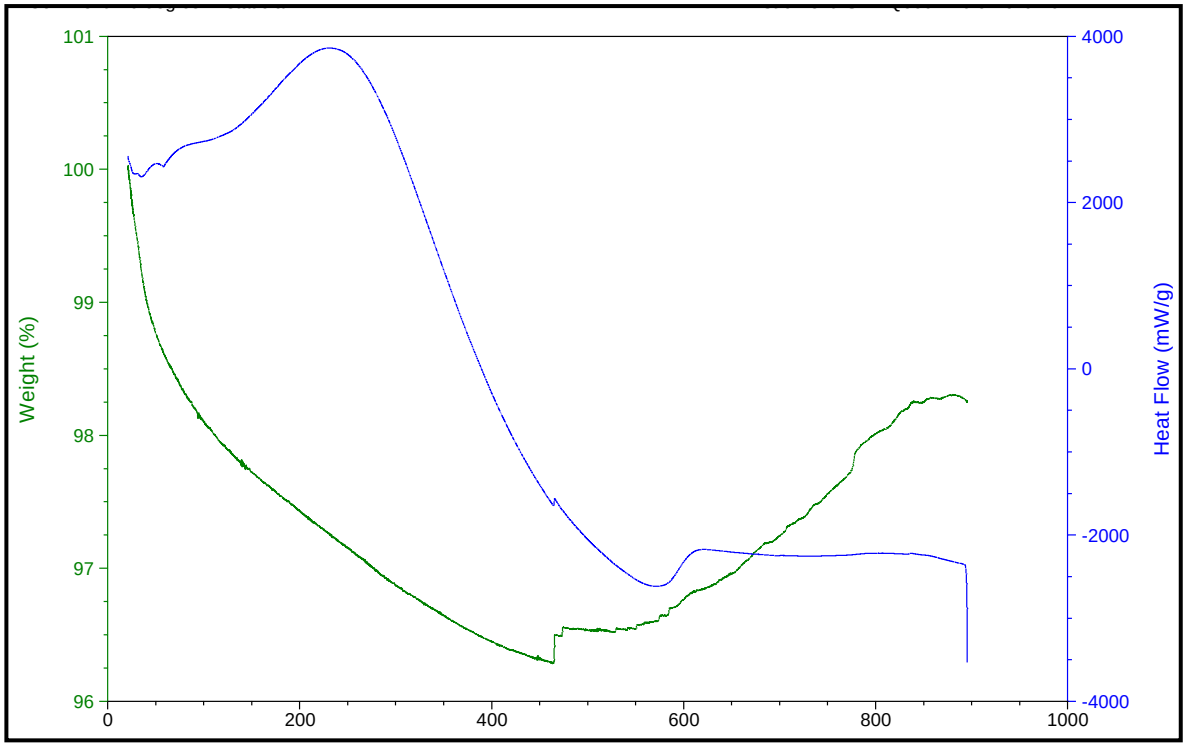

Figure 5.14: TGA-DSC curve of calcined NM-A

5.2.9 Temperature Programmed Reduction (TPR)

The Temperature Programmed Reduction of α-$NiMoO_4$ (NM-A) under hydrogen occurs at two temperatures. The first, lower temperature reduction is allocated to three possible products; metallic nickel, Ni_4Mo and amorphous MoO_2. The second higher temperature reduction is attributed to that of Mo^{4+} to metallic molybdenum, intermetallic Ni_3Mo and a Ni-Mo alloy. This first reduction peak corresponds to the phases seen in the in situ x-ray diffractogram at 550°C whereby Mo^{2+} and Ni exist as MoO_2 and metallic nickel, respectively.

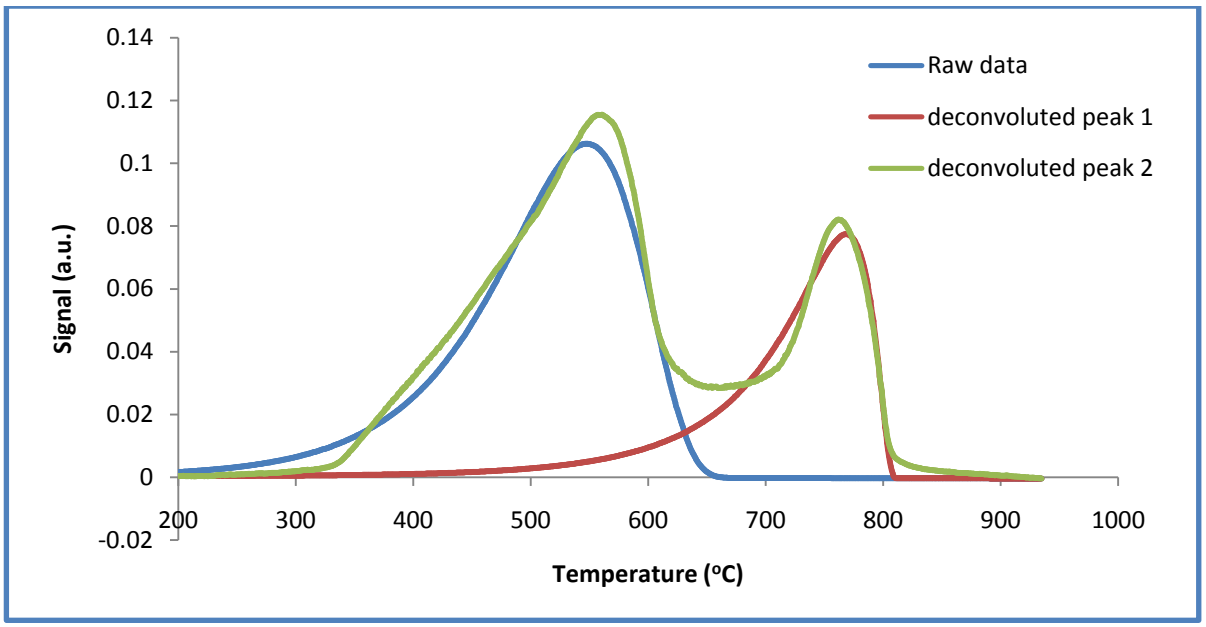

Figure 5.15: TPR of NM-A

5.3 Carbon nanotubes

This section will discuss the characterisation results of the carbon nanotube (CNT) support and the supported catalyst which consists of α-$NiMoO_4$ on CNT, referred to from here on as NM-CNT.

5.3.1 Attenuated Total Reflectance-Infrared Spectroscopy (ATR-IR)

Infra-red spectroscopy was used to study the chemical nature of the surface of the CNT as well as that of the oxidised CNT.

The peaks in Figure 5.16 are of the supported catalyst post calcination. The peaks below 950 cm^{-1} represent the out of plane deformation vibrations of the C-H groups in the aromatic structure [11]. The bands at 1330 cm^{-1} and 1530 cm^{-1} are allocated to the symmetric and asymmetric stretching vibrations of the NO_2 group respectively, which indicates that the HNO_3 treatment introduced NO_2 groups onto the CNT surface. The peak at 1378 cm^{-1} is due

to nitrates adsorbed on the CNT surface. The band at 1726 cm^{-1} is allocated to carboxylic anhydride or lactone groups [12-13]. It can therefore be concluded that the treatment of the CNTs with HNO_3 resulted in the introduction of ketone, carboxylic, lactone and nitro groups on the surface of the support.

The oxidised CNTs were calcined, after being deposited with the nickel molybdate precursor, at 550°C in airflow for 2 hours. Phenolic groups are represented by a band at ~ 1200 cm^{-1} [14] and is clearly absent in the spectrum below. It can be construed that heat treatment decomposes certain surface oxygen functional groups when calcined to 550°C [15]. The NM-A peaks are visible at 429 cm^{-1} and 625 cm^{-1}.

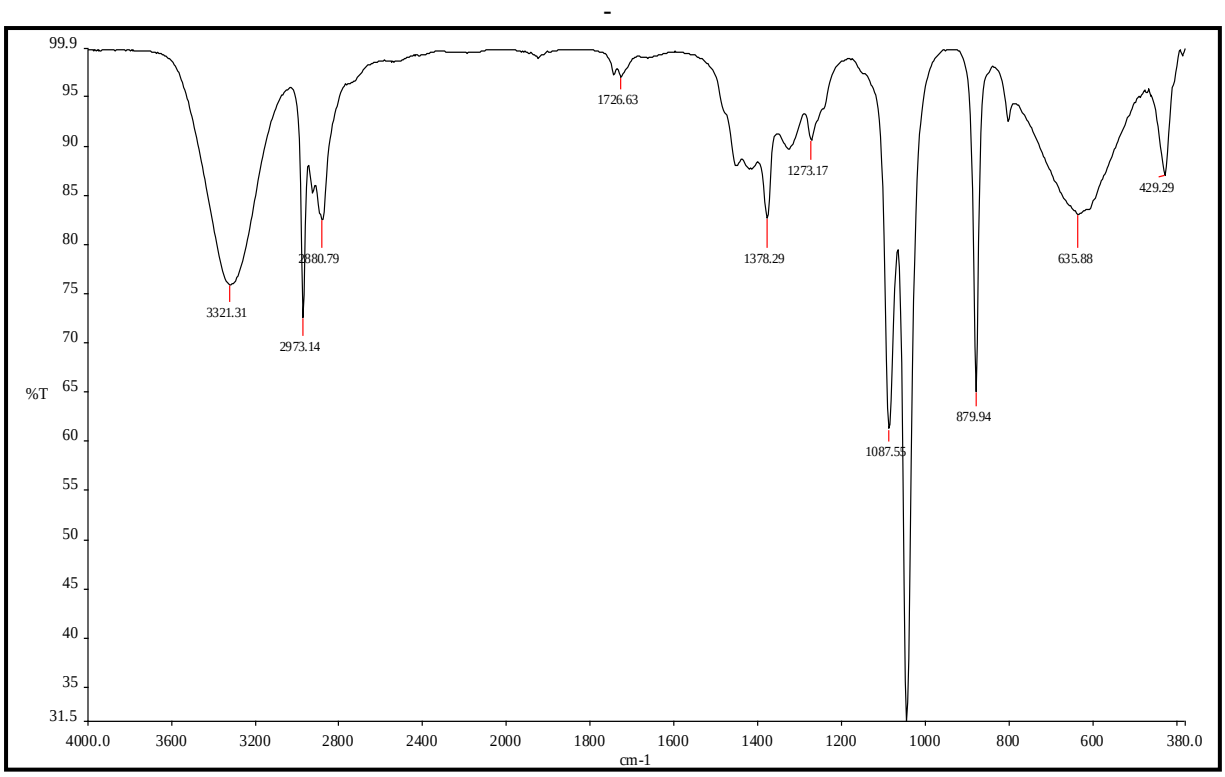

Figure 5.16: IR spectra of supported CNT (post calcination)

5.3.2 Raman Spectroscopy

Figure 5.17 displays the Raman spectrum of CNTs. The vibrational band appearing at 1350 cm^{-1} is assigned to the disordered carbon structure (i.e. the D-band) and the band at 1580 cm^{-1} is assigned to the graphitic mode (i.e. the G-band). The D-band indicates the degree of disorder with respect to the orientation of the nanotubes whereas the G-band reflects the structure of the sp^2 hybridised carbon and represents the degree of graphitisation [16]. The extent of graphitisation in the CNT can be quantified by the intensity ratio of the G-to-D bands (i.e. I_G/I_D). The ratios of I_G/I_D shown in Table 5.4 are 1.2 and 1.6 for the CNT and calcined NM-CNT, respectively. It can clearly be seen that the I_G/I_D ratio increases for the supported CNT upon heat treatment confirming an increase in graphitisation of the carbon structure [16].

Table 5.4: Ratio of intensities of Raman peaks of CNT and NM-CNT

Catalyst	I_G/I_D
CNT	1.2
NM-CNT uncalcined	1.2
NM-CNT calcined	1.6

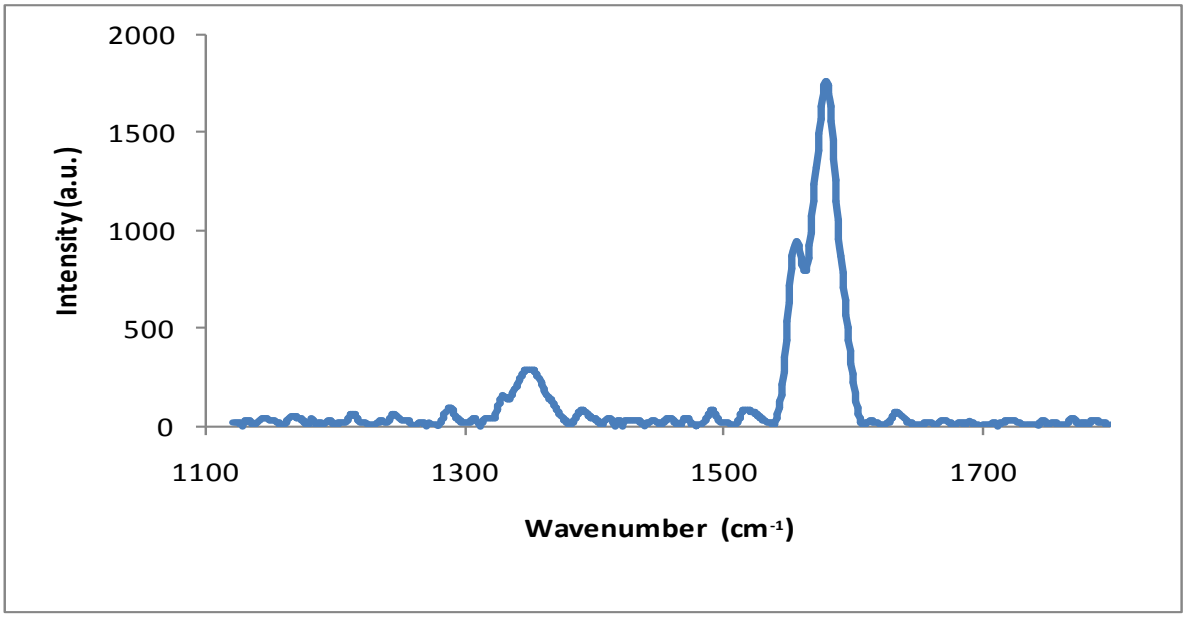

Figure 5.17: Raman spectrum of CNT

5.3.3 Inductively Coupled Plasma-Optical Emission Spectroscopy (ICP-OES)

The loading of the nickel molybdate catalyst on the CNT support was carried out by wet impregnation, homogeneous deposition precipitation (HDP) and co-precipitation. Impregnation involves the deposition, of a solution containing the precursor, of the active phase on to the support. In this case excess-solution impregnation was the first method used. This involved the use of a volume of solution much larger than the pore volume of the support. The resulting slurry which formed was filtered after a period of time to remove the excess solvent. This method does not allow for precise control of the amount of catalyst loaded unless a study is carried out to determine adsorption isotherms [17].

The pH was varied for the HDP experiments in order to determine the optimum pH for a maximum loading of the nickel molybdate catalyst. Urea was used as its hydrolysis releases the hydroxyl anion which acts as a precipitating agent [18]. Figure 5.18 shows that the loading of molybdenum increases with increasing pH with the maximum loading of 7% achieved at a pH of 5.7, after which the molybdenum loading decreases as the conditions become more basic. The variable parameter for the wet impregnation experiments was time. Figure 5.19 shows that the loading of molybdenum on CNT increases as time increases and

levels off at 5.5 hours with a maximum loading of 7.2% achieved at 6.5 hours. In both the HDP and wet impregnation techniques there exists a higher concentration of metal in the filtrate than on the CNT. More importantly, the catalyst stoichiometry of the α-phase is lost as the Ni:Mo ratio is no longer 1. The co-precipitation method resulted in the α-phase being successfully supported on the CNT surface and the ratio of Ni:Mo is maintained at one as confirmed by the XRD and ICP analyses respectively. The loading of nickel molybdate on the CNT surface was determined to be 15 %. This supported catalyst, NM-CNT, was used in the catalytic tests.

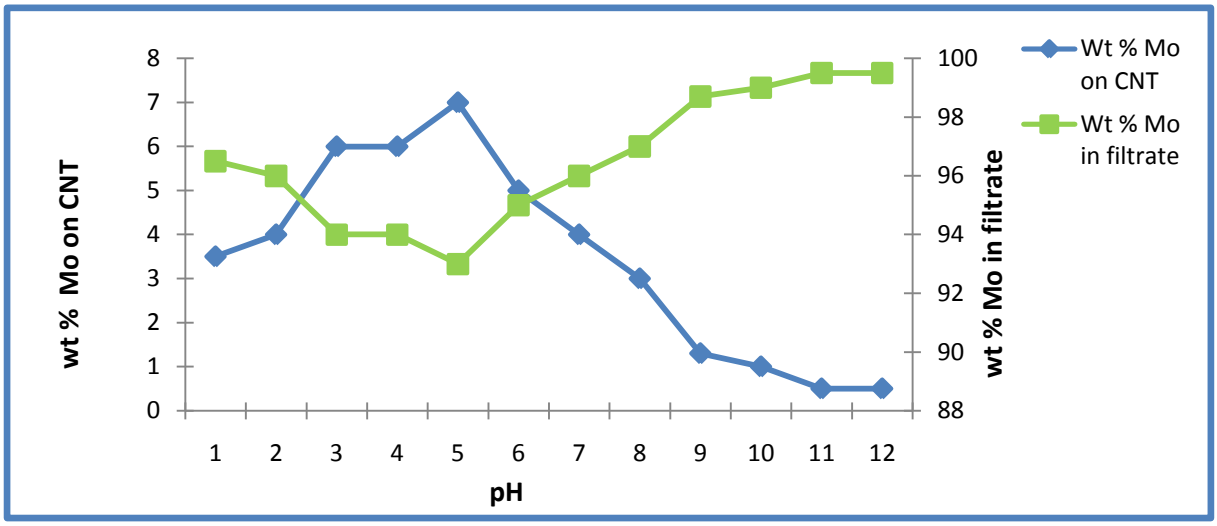

Figure 5.18: Loading of Mo on CNT by Homogeneous deposition precipitation

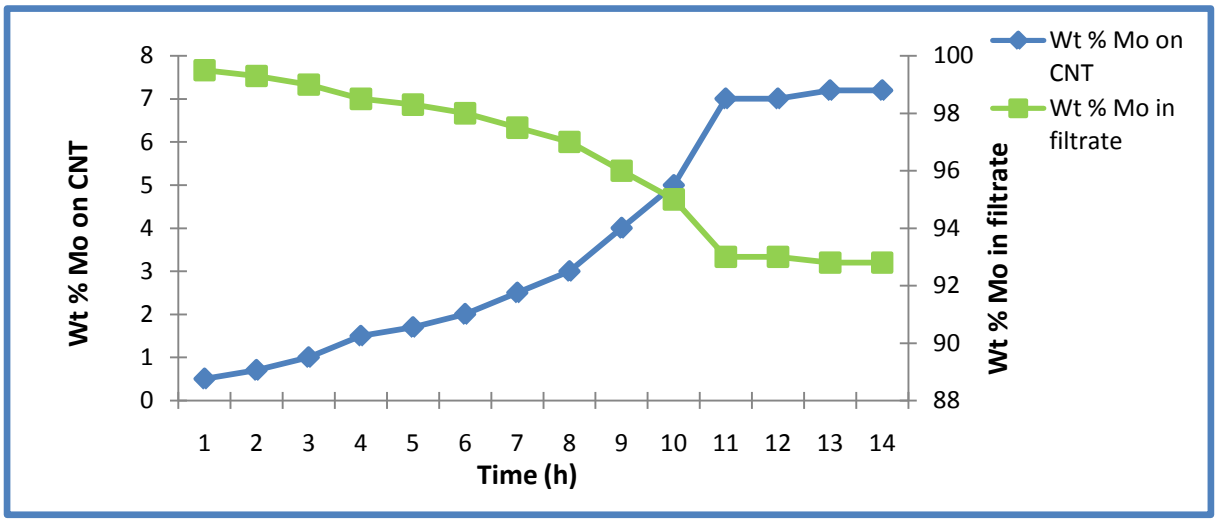

Figure 5.19: Loading of Mo on CNT by Wet Impregnation

5.3.4 Powder X-ray Diffraction (XRD)

The powder x-ray diffractogram of the carbon nanotubes shows the presence of sharp peaks indicating a rigid crystalline structure. The high intensity of the peak at 26° indicates a lower alignment of the tubes i.e. the tubes do not lie parallel to one another in a neatly ordered fashion but are rather randomly aligned. The crystal faces of the 002, 100 and 110 planes are illustrated by the peak at 26°, the doublet between 42.5° and 44° and the peak at 77.2° respectively. The peaks at 42.5°, 44°, 50°, 54°, 74° and 77.2° may be ascribed to the diffraction peaks for the planes of graphite [19-20].

The powder XRD of the supported catalyst shows the nickel molybdate to exist as the stoichiometric α-phase illustrated by its characteristic peaks at 2θ = 14.2°, 25.5°, 29.6°, 33.0°, 38.8° and 41.4°, 43.9°, 47.5°, 53.0°, 56.1°, 58.2° and 62.0°. The CNT is represented by the intense peak at 26.03°. The CNT peaks at 42.5°, 44°, 50°and 54° are underneath the corresponding molybdate peaks. The supported catalyst is crystalline as inferred from the sharp peaks of the diffractogram, having an average crystallite size of 17.4 nm.

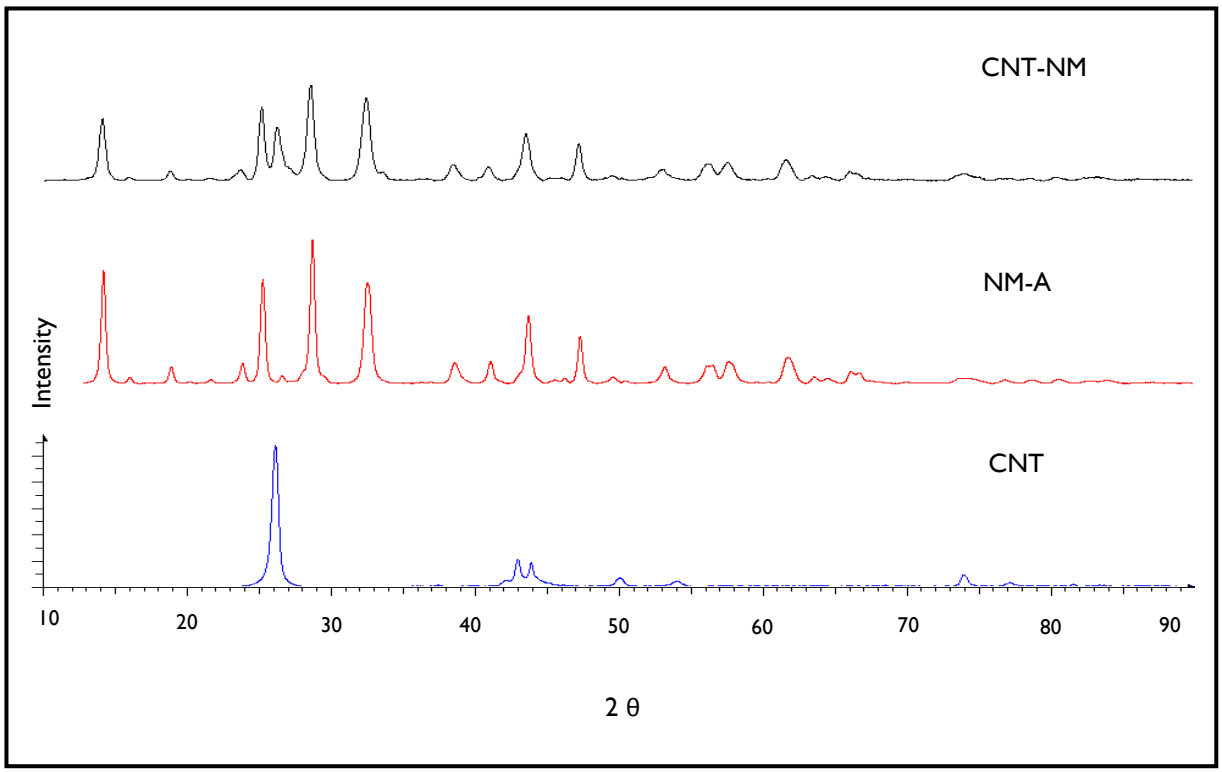

Figure 5.20: Powder x-ray diffractogram of CNT, NM-A and NM-CNT

5.3.5 *In situ* X-ray Diffraction (*In situ* XRD)

The *in situ* x-ray diffractogram of the carbon nanotubes, which were heated from room temperature to 600°C in air, shows the nanotubes to be thermally stable. There is no change of structure relating to a change of phase. The crystallite size remains the same, as for the room temperature scan, at 14.3 nm. The *in situ* reaction was repeated in the presence of hydrogen gas to create a reducing atmosphere in order to gain an understanding of the possible changes which occur within the nanotube structure in the reactor. The diffractogram shows the same result as both the *in situ* in air and powder analysis. The nanotubes are stable in a reducing atmosphere at high temperatures up to 600°C.

The *in situ* studies carried out in air show the catalyst to be stable at temperatures up to 600°C as there are no phase changes which take place, for both the nickel molybdate and the CNT. The β-phase transition is not seen under these conditions as the temperature of the reaction cell could not reach the desired temperature of 720°C for the phase transformation to take place. In the presence of a reducing atmosphere of hydrogen gas, however, the nickel molybdate changes phase in same manner as when unsupported. These phases are allocated to MoO_2 and metallic nickel. Re-oxidation in air results in a further phase change to the metastable β-phase. It can therefore be postulated that the transition from the α to β-phase occurs via an intermediate mixed phase of MoO_2 and nickel. The supported catalyst behaves in the same manner, at room temperature and under *in situ* conditions, as the nickel molybdate and CNT individually.

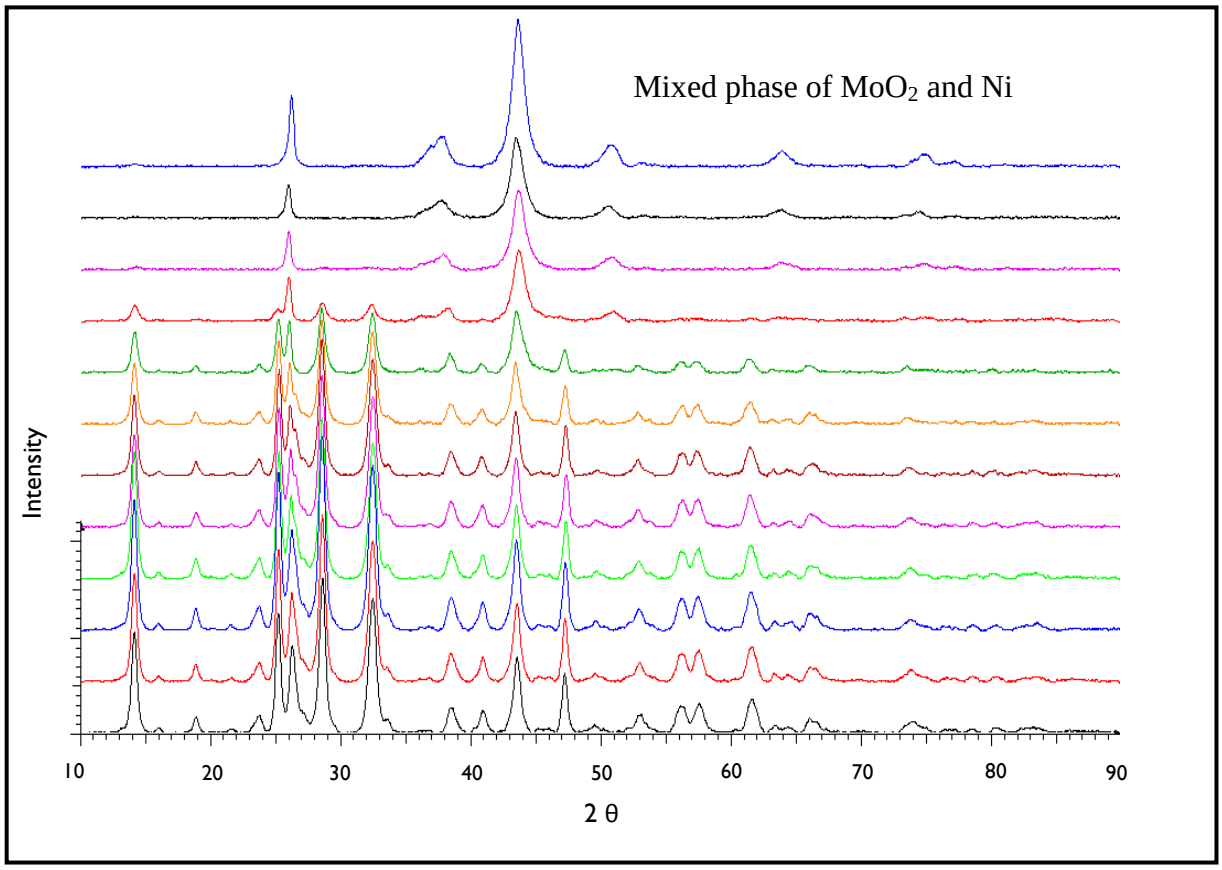

Figure 5.21: *In situ* x-ray diffractogram of NM-CNT reduced under hydrogen

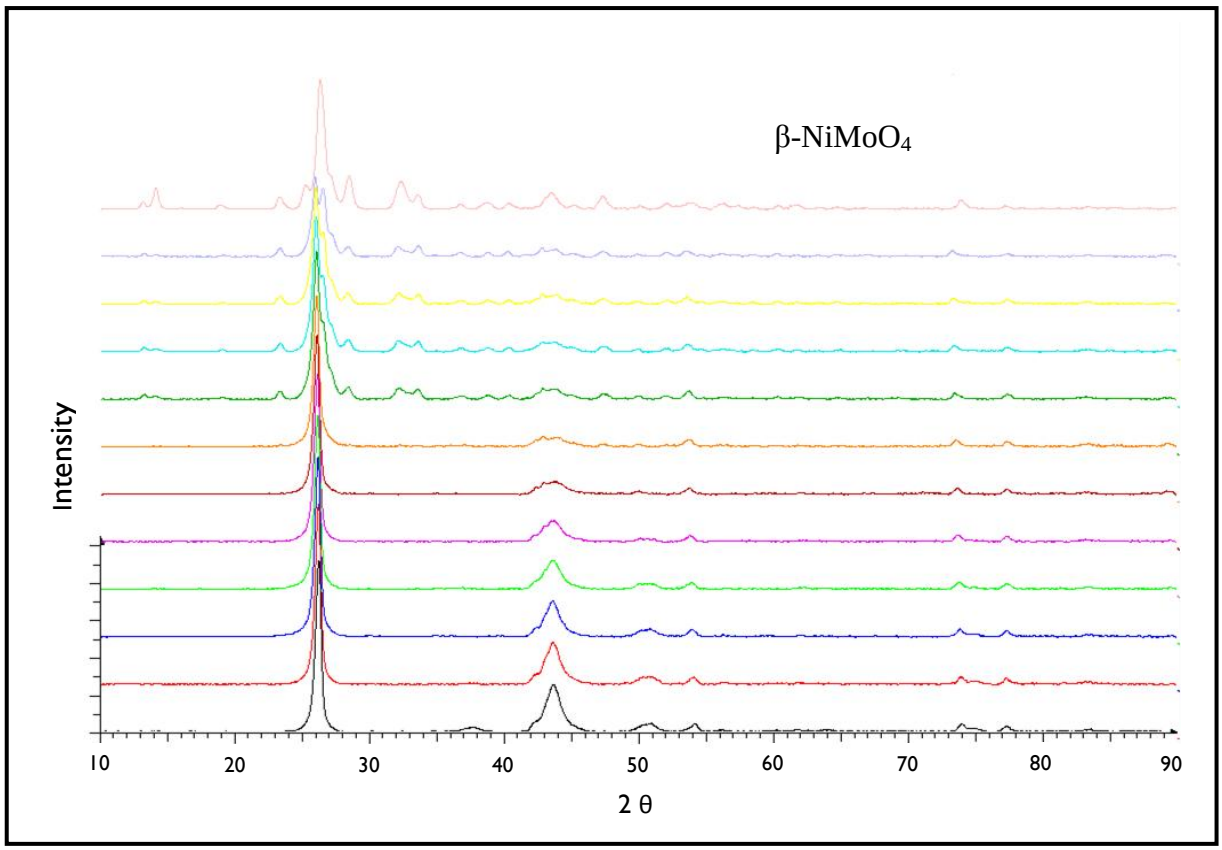

Figure 5.22: *In situ* x-ray diffractogram of NM-CNT re-oxidised in air

5.3.6 Brunauer-Emmet-Teller surface analysis (BET) and Scanning Electron Microscopy (SEM)

The SEM images of the CNTs in Figure 5.23 show the structure to consist of a matrix of entangled tubes varying in length and diameter. It is this entangled agglomerate of tubes which give the CNTs their property of high mechanical strength as well as facilitating an open pore volume and even pore size distribution [21]. The observed BET surface area and pore volume of the CNT was found to be 72.5 m^2/g and 0.3 cm^3/g respectively. This porous nature of the material is in accordance with the entangled tubular structure seen in the SEM micrograph. SEM-EDX analysis of the CNTs confirms the purity of the material as no metal species were detected.

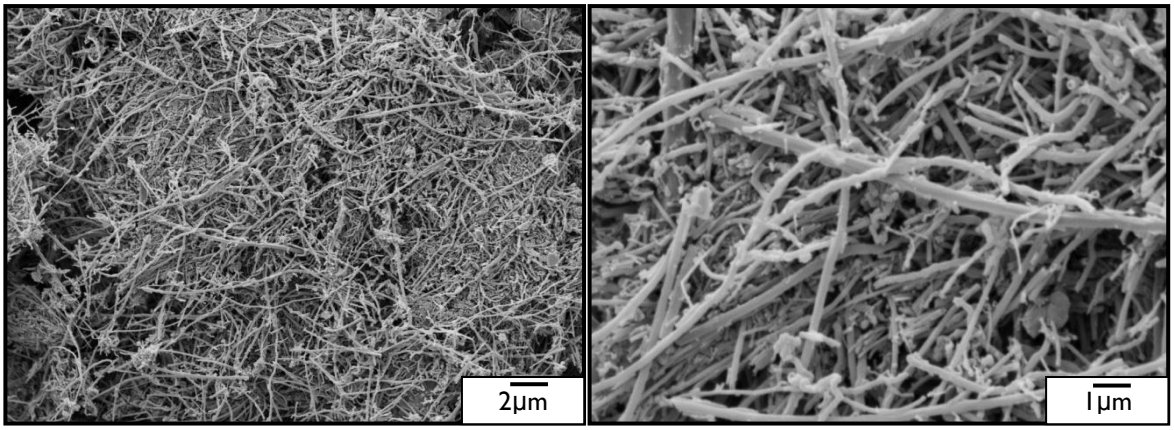

Figure 5.23: SEM images of CNTs

The backscattered SEM image of the uncalcined NM-CNT in Figure 5.24 a shows the nickel molybdate (which appears as the brighter particles) to be clustered and sparsely dispersed on the CNT. The supported catalyst was calcined at 550°C in a flow of air for 2 hours. This was done in order to transform the nickel molybdate precursor to the α-$NiMoO_4$ catalyst, by allowing the volatile components to sublime, leaving behind the thermally stable active phase. Moreover the heat treatment of the supported catalyst results in an increase in agglomeration of the nickel molybdate clusters on the CNT surface, seen in Figure 5.24 b. The calcination process is important for the distribution of the active phase on the support surface. The calcination temperature is also of importance. In the case of Pt supported on carbon it was found that if the calcination temperature exceeds the temperature at which the surface oxygen functional groups decompose, the metal dispersion is increased [22-23].

It can be seen from the results in Table 5.5 that the supported catalyst has a surface area and pore volume higher than NM-A but lower than CNTs. It can be inferred that the clusters of NM-A block some of the pores of the CNT and the overall surface area of the supported catalyst lies in between that of NM-A and CNTs alone. The same conclusion can be drawn for the crystallite size of the supported catalyst. A possible explanation for the increase in crystallite size of the supported catalyst as compared to NM-A is the anchoring of NM-A particles to the CNT surface as well as the agglomerated particle distribution.

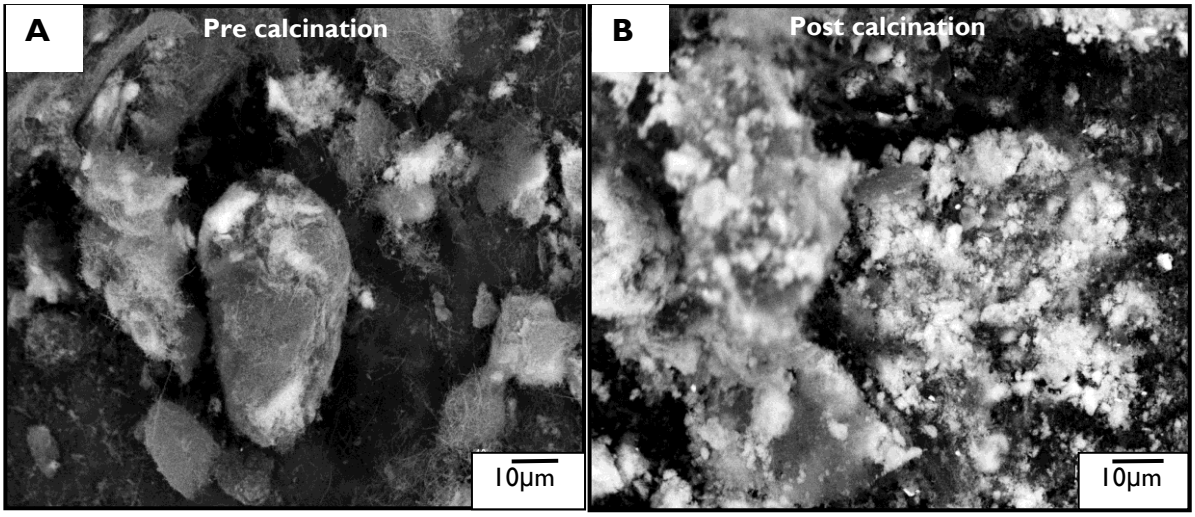

Figure 5.24: Backscattered SEM images of NM-CNT pre and post calcination

Table 5.5: BET surface area and XRD crystallite size of CNT, NM-A and NM-CNT

Catalysts	**Surface area** ($m^2.g^{-1}$)	**Pore volume** ($cm^3.g^{-1}$)	**[a]Crystallite size** (nm)
CNT	72.5	0.32	14.3
NM-A	43.8	0.25	19.3
NM-CNT	52.0	0.29	17.4

[a] *Calculated using the Scherrer equation from FWHM of highest intensity peak (XRD)*

5.3.7 Transmission Electron Microscopy (TEM)

The Transmission Electron Microscopy (TEM) images show the varied structure of the carbon nanotubes. The inner and outer tube walls can clearly be seen as well as the rigid nature of the material (Figure 5.25 a). Some tubes are straight whilst others display a bamboo-like structure (Figure 5.25 b) having ends which are either capped or open. The tubes are pure as no traces of metals can be seen from the TEM images which are in accordance with the SEM EDX analysis. The inner and outer diameters of the tubes were measured by using *i*TEM software (Table 5.6) and found to vary within the range of 26.1 - 100 nm and 39.6 - 189.3 nm respectively.

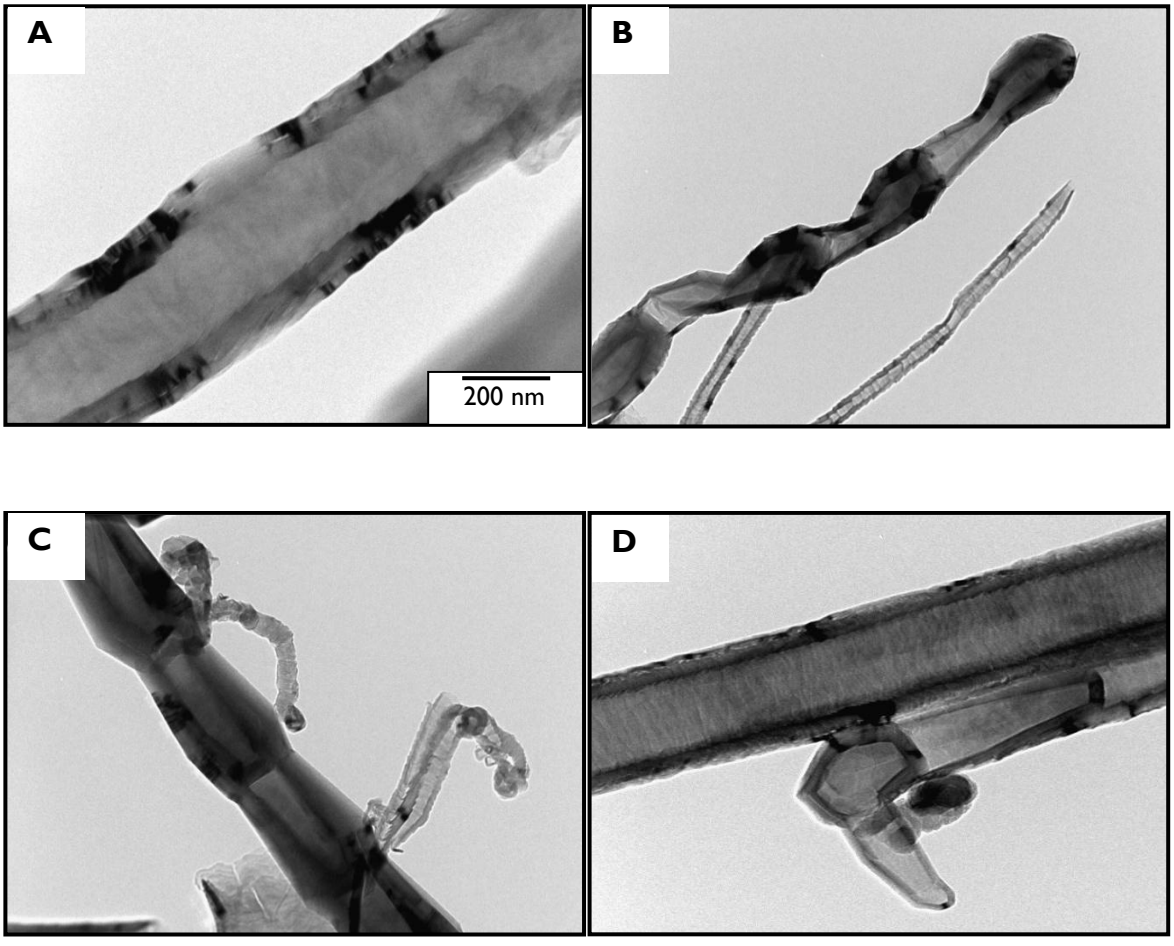

Figure 5.25: TEM images of CNT

Table 5.6: Particle size analysis from *i*TEM software

Catalyst	Mean length/ nm	Min length/ nm	Max length/ nm
CNT outer diameter	189.3	39.6	318.3
CNT inner diameter	100.0	26.1	130.0
NM-A	21.3	12.6	25.0

The TEM image of the supported catalyst prior to calcination (Figure 5.26 a) shows the elongated nickel molybdate particles to exist localised on the surface of the CNT. There exists a high degree of agglomeration of the nickel molybdate particles on the CNT surface post calcination (Figure 5.26 b). This increase in agglomeration of the catalyst particles after heat treatment corresponds with the results seen in the SEM images (figure 5.24 a and b) and is in keeping with the report by Prado-Burguete et al. [22-23] which stresses the importance of the temperature at which the surface oxygen functional groups decompose. For Pt catalyst supported on carbon it was found that if the catalyst heat treatment temperature exceeds that at which the majority of the surface oxygen functional groups decompose, the metal dispersion also increased [22]. A similar finding was reported by Keyser and Prinsloo who found that heat treatment of a carbon nanofiber supported Co catalyst at 300°C resulted in an increase in interaction between the metal species and the support [18]. It can be seen from the images in Figure 5.26 that the catalyst particles lie in an interweaved matrix (i.e. between the CNT) as well as on the surface of the CNT support.

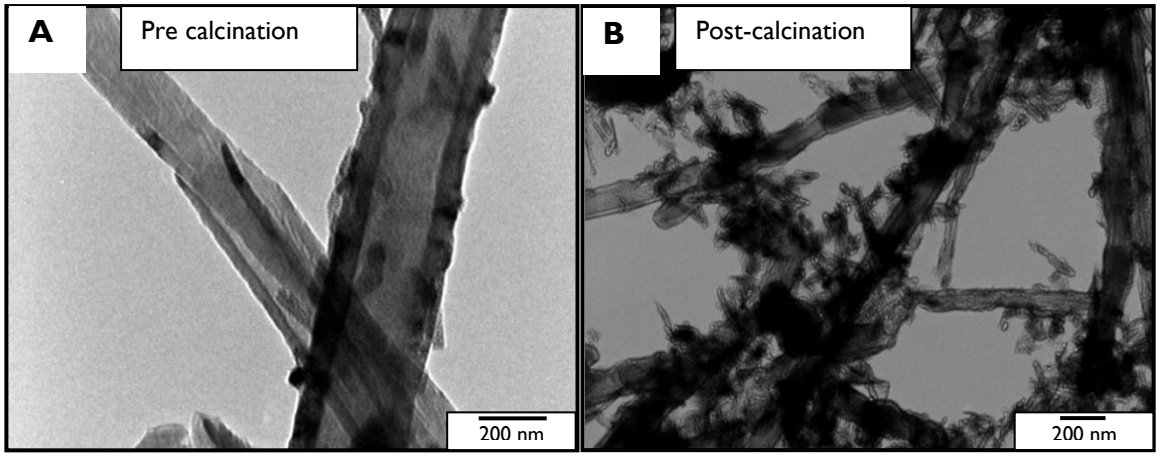

Figure 5.26: TEM images of NM-CNT pre and post calcination

5.3.8 Thermogravimetric Analysis (TGA) and Differential Scanning Calorimetry (DSC)

The thermogravimetric (TGA) analyses provide an indication of the types of surface oxygen functional groups present on the CNT and the temperatures at which these functional groups decompose. The TGA and corresponding differential curve of the CNT (Figure 5.27) shows a major weight loss of 98.4 % between 772°C and 928°C. This thermal decomposition, which is accompanied by an exothermic DSC transition, is a characteristic feature, which illustrates the high thermal stability, of carbon nanotubes. The differential curve of the functionalised CNT is represented in Figure 5.28. The peak at 98°C is due to the desorption of physisorbed water on the surface [24]. There are also peaks and shoulders at 420°C, 475°C, 600°C, 680°C, 725°C, 780°C, 875°C, 900°C and 950°C. It has been reported in TPD studies carried out on activated carbon oxidised with HNO_3 that, in general, CO_2 desorbs between 100°C and 700°C and as many as four peaks have been observed in this region. The peaks allocated to CO were found to desorb between 227°C and 1000°C and in this region six peaks were observed [24-26]. Therefore in this case it can be postulated that the peaks at 420°C, 475°C, 600°C and 680°C are due to both CO_2 and CO forming groups, whereas the peaks at 725°C, 780°C, 875°C, 900°C and 950°C are allocated to CO forming groups. Therefore the calcination of the supported catalyst at 550°C has decomposed some of the CO_2 forming groups.

The DSC curve of the uncalcined supported catalyst (Figure 5.29) shows an exothermic transition between 100°C and 300°C which is attributed to the transformation of the nickel molybdate precursor to that of the α-molybdate catalyst. The differential curve displays a peak at 440°C, accompanied by an exothermic transition, which is due to the decomposition of the CO_2 forming groups [24]. The large exothermic weight loss of 51 % between 618°C and 801°C is attributed to the decomposition of CO and CO_2 forming groups as well as the decomposition of the CNTs. The supported catalyst displays a significant decrease in weight loss and temperature range at which the weight loss occurs as compared to the CNT. It can be concluded that the supported catalyst is less thermally stable than the CNTs alone. This could be due to the fact that functionalisation of CNTs introduces surface defects and kinks which act as anchoring sites for the metal particle (in the case of metal supported CNTs). Furthermore the introduction of a large number of functionalities can reduce the mechanical and electronic properties of the material and prolonged sonication may lead to fragmentation and mechanical damage of the tubes [27] (discussed in section 3.4). This deformation in structure of the CNTs could possibly be the reason for the decrease in thermal stability of the supported catalyst.

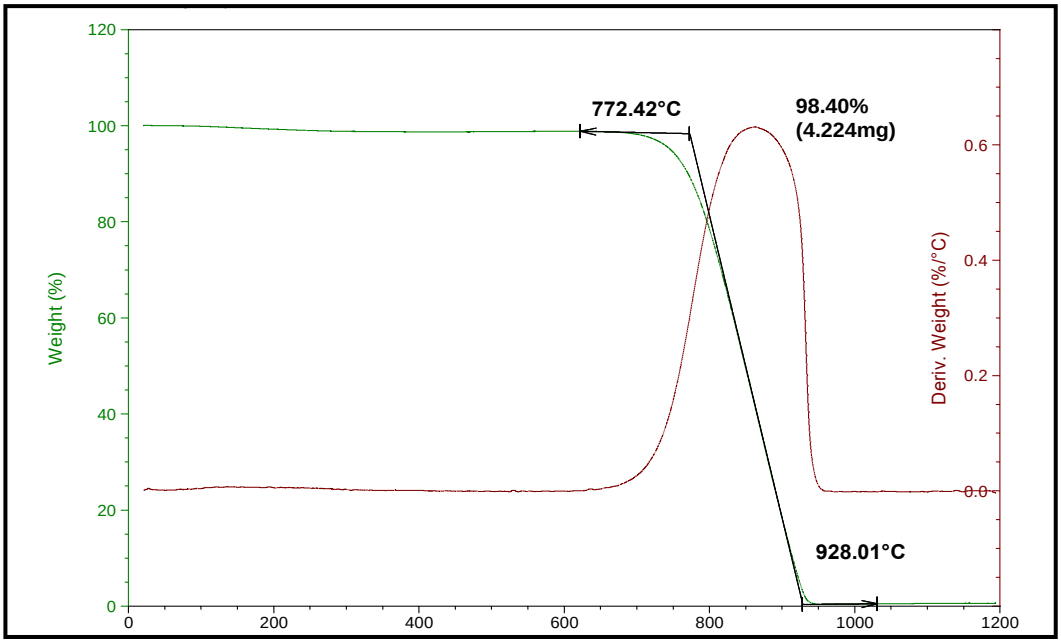

Figure 5.27: TGA-DSC curve of CNT

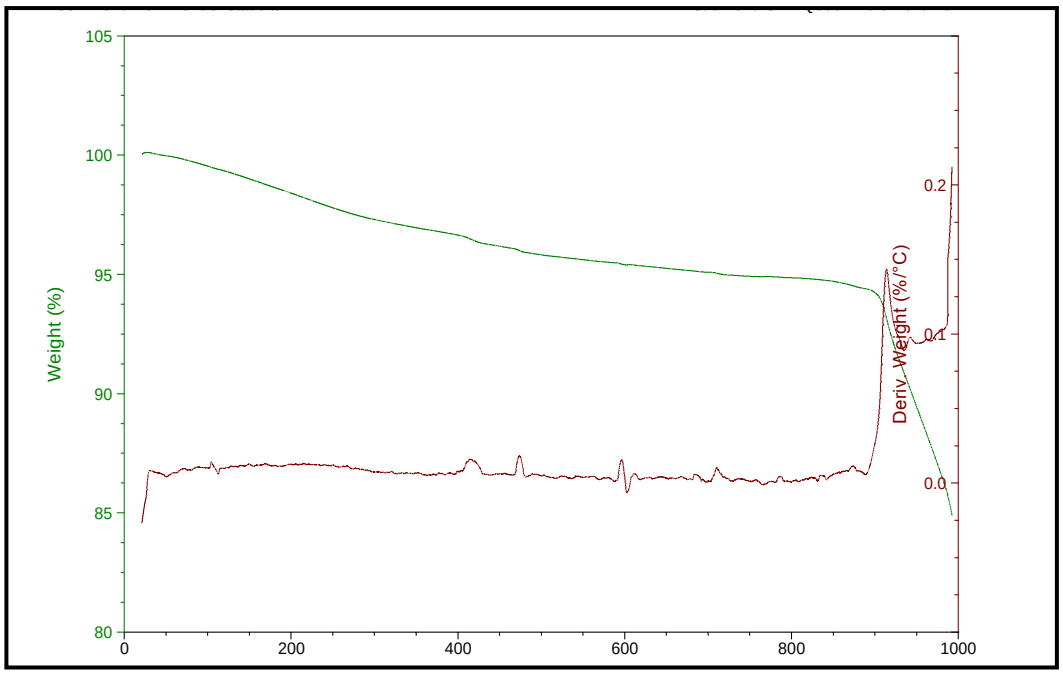

Figure 5.28: TGA-DSC curve of functionalised CNT

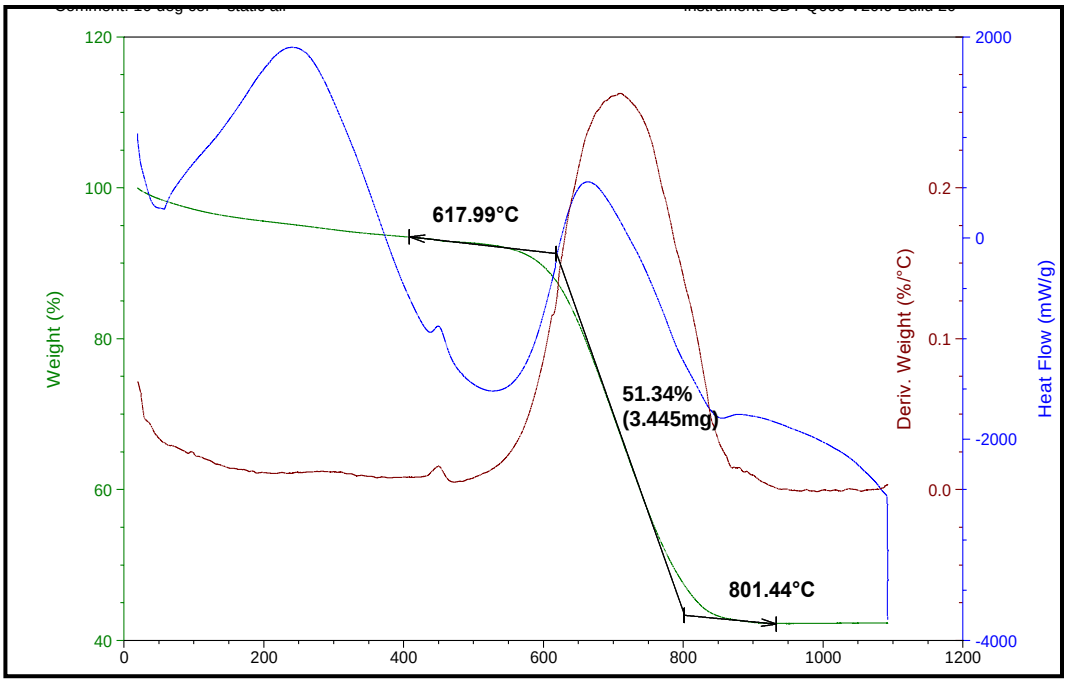

Figure 5.29: TGA-DSC curve of uncalcined NM-CNT

5.3.9 Temperature Programmed Reduction (TPR)

The TPR profile of NM-CNT is deconvoluted to four peaks. The first peak at 400°C (peak 1) is possibly due to the decomposition of more temperature stable surface oxygen functional groups which are more difficult to reduce [18]. Peak 4 at 520 °C is allocated to the catalysed hydrogasification of CNTs at this temperature [28-29]. Peaks 2 and 3 are due to the reduction of nickel molybdate (see section 5.2.9).

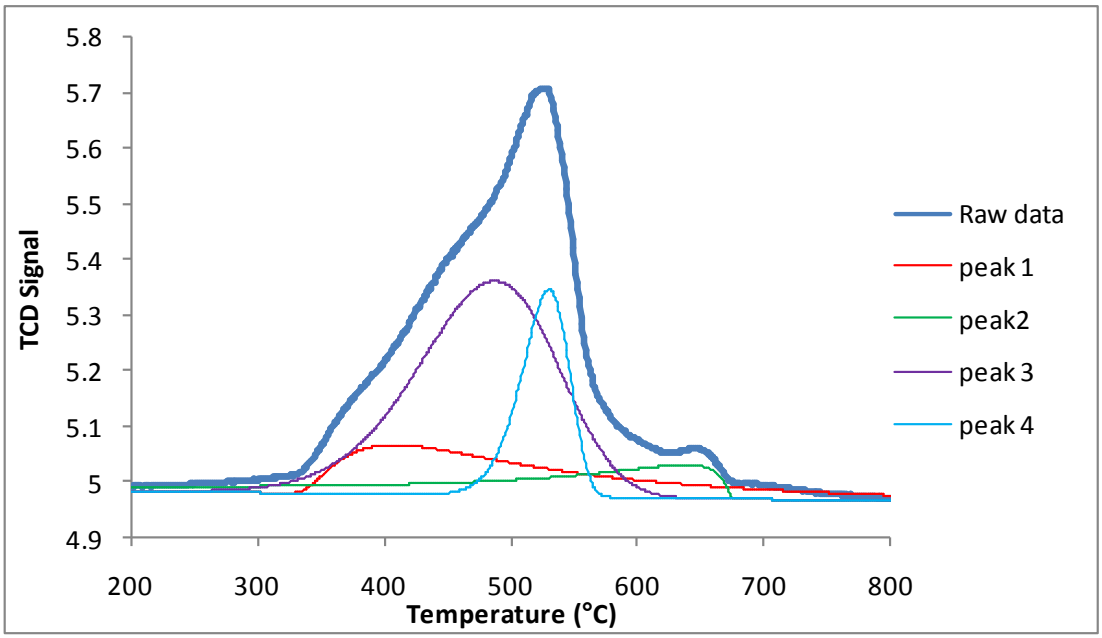

Figure 5.30: TPR profile of NM-CNT post calcination

5.4 Conclusion

Nickel molybdate precursors were synthesised by co-precipitation and calcined in air to yield the catalysts. The chemical composition of the catalysts were analysed by ICP and three catalysts were compared; stoichiometric nickel molybdate (Ni:Mo = 1), nickel molybdate containing excess nickel (Ni:Mo > 1) and nickel molybdate containing excess Mo (Ni:Mo < 1). The textural properties and phase composition of these catalysts were analysed using a range of characterisation techniques. Powder XRD and IR spectroscopy were used to study the phase composition of the catalysts. *In situ* XRD showed the high temperature transition of the α-molybdate to the metastable β-phase which was achieved by first reducing the catalyst in hydrogen and then re-oxidising it in air. The intermediate phases present after the reduction were allocated to MoO_2 and metallic nickel. This result corresponds to the first reduction peak in the TPR analyses (Mo^{4+} and metallic nickel). Raman spectroscopy was used to further study the phase composition of the catalysts. SEM and TEM were used to analyse the surface morphology which displayed the porous nature of the nickel molybdates which was further confirmed by BET surface area and pore volume measurements.

Three different approaches were explored for the synthesis of carbon nanotube supported nickel molybdate, namely; homogeneous deposition precipitation (HDP), wet impregnation and co-precipitation with the latter resulting in the successful synthesis of the α-molybdate supported CNT. Heat treatment was found to result in a stronger interaction of metal catalyst to the support. SEM and TEM microscopy showed the distribution of molybdate particles agglomerated as clusters on the CNT surface.

5.5 References

[1] Mazzocchia, C., Anouchinsky, R., Kaddouri, A., Sautel, M., Thomas, G., *Journal of Thermal Analysis*, 1993, **40**, 1253.

[2] Andrushkevich, M.M., Buyanov, R.A., Sitnikov, V.G., Khramova, G.A., *Kinetics Catalysis*, 1973, **14**.

[3] Niemantsverdriet, J.W. *Spectroscopy in Catalysis*, 3rd ed.; Wiley-VCH: Weinheim, 2007.

[4] Madeira, L.M., Martín-Aranda, R.M., Maldonado-Hódar, F.J., Fierro, J.L.G., Portela, M. F., *Journal of Catalysis*, 1997, **169**, 469.

[5] Nyquist, R.A., Kagel, R.O., *Infrared spectra of inorganic compounds*, Academic Press: New York, 1971.

[6] Lezla, O., Bordes, E., Courtine, P., Hecquet, G., *Journal of Catalysis*, 1997, **170**, 346.

[7] Maldonado-Hódar, F.J., Madeira, L. M., Portela, M. F., Martín-Aranda, R.M., Freire, F., *Journal of Molecular Catalysis A: Chemical*, 1996, **111**, 313.

[8] Kaddouri, A., Del Rosso, R., Mazzochia, C., Fumagalli, D., *Journal of Thermal Analysis*, 2001, **63**, 267.

[9] Ozkan, U., Schrader, G.L., *Journal of Catalysis*, 1985, **95**, 120.

[10] Zãvoianu, R., Dias, C. R., Farinha Portela, M., *Catalysis Communications*, 2001, **2**, 37.

[11] Morena-Castilla, C., López-Ramón, M.V., Maldonado-Hódar,F.J., Rivera-Utrilla, J, *Carbon*, 1998, **36**.

[12] Socrates, G. *Infrared characteristic group frequencies*; John Wiley & Sons: New York, 1980.

[13] Morena-Castilla, C., López-Ramón, M.V., Carrasco-Marín, F, *Carbon*, 2000, **38**.

[14] Alciatari, C. E., Escobar, M.E., Vallejo, R., *Fuel*, 2000, **75**.

[15] Otake, Y., Jenkins, R.G., *Carbon*, 1993, **31**.

[16] Wang, J., Yin, G., Shao, Y., Wang, Z., Gao, Y., *Journal of Physical Chemistry*, 2008.

[17] AbdelDayem, H. M., Sadek, S. A., *Thermochimica Acta*, 2008, **473**, 96.

[18] Keyser, M.M., Prinsloo, F.F., *Studies in Surface Science and Catalysis*, 2007, **163**, 45.

[19] Endo, M., Kim, Y.A., Hayashi, T., Yanagisawa, T., Muramatsu, H., Ezaka, M., Terrones, H., Terrones, M., Dresselhaus, M.S, *Carbon*, 2003, **41**, 1941.

[20] Andrews, R., Jaques, D., Qian, D., Dickey, E.C., *Carbon*, 2001, **39**, 1941.

[21] Geus, J.W., Van Dillen, A.J., Hoogenraad, M.S., *Materials Research Society Symposium Proceedings*, 1995, **368**, 87.

[22] Prado-Burguette, C., Linares-Solano, A., Rodriguez-Reinoso, F., Salinas-Martinez de Lecea, C., *Journal of Catalysis*, 1991, **128**.

[23] Prado-Burguette, C., Linares-Solano, A., Rodriguez-Reinoso, F., Salinas-Martinez de Lecea, C., *Journal of Catalysis*, 1989, **115**.

[24] Haydar, S., Moreno-Castilla, C., Ferro-Garcia, M.A., Carrasco-Marín, F., Rivera-Utrilla, J., Perrard, A., Joly, J.P., *Carbon*, 2000, **38**.

[25] Kruse, C. W., Lizzio, A.A., DeBarr, J.A., Feizoulof, C.A., *Energy & Fuels*, 1997, **11**.

[26] Mochida, I., Kuroda, K., Miyamoto, S., Sotowa, C., Korai,Y., Kawano,S., Sakanishi, K., Yasutake, A., Yoshikawa, M., *Energy & Fuels*, 1997, **11**.

[27] Bitter, J. H., Murzin, D.Y., *Nanocatalysis*, Research Signpost: Kerela, India, 2006.

[28] Prinsloo, F. F., van Steen, E., *Catalysis Today*, 2002, **71**, 372.

[29] De Jong, K. P., *Current Opinion in Solid State & Materials Science*, 1999, **4**, 55.

Chapter 6: Catalytic Testing

This chapter presents and discusses the catalytic results obtained for the activation of *n*-octane over four catalysts; α-nickel molybdate (α-NM), β-nickel molybdate (β-NM), carbon nanotubes (CNT) and α-nickel molybdate supported on carbon nanotubes (α-NM-CNT). Results from the blank studies are also discussed where a carborandum packed reactor was used in the absence of catalyst. The C_8H_{18}/O_2 ratio was kept constant at two for all reactions. The gas hourly space velocities tested were 2500 h^{-1}, 4000 h^{-1}, 5000 h^{-1} and 7500 h^{-1} within the temperature range of 250°C-500°C.

6.1 *n*-octane activation in a carborandum packed reactor

The chemical inertness of paraffins demands a high energy input to break the stable C-H bond, which as a result proceeds at high temperatures. The activation of *n*-octane, for the purpose of this study, was carried out in a plug-flow fixed bed stainless steel reactor. Such metal surfaces when heated generate sufficient energy to initiate free radical reactions which occur in the homogeneous gas phase [1]. These free radical reactions may play a vital role in the formation of the desired products or may result in non-selective partial oxidation [2]. In order to determine the effect of such reactions, blank studies were carried out where the feed was activated in a carborandum packed reactor.

The feed was composed of 30 % octane in air and diluted with nitrogen to make up a flow rate of 4000 h^{-1}. The graph (Figure 6.1) shows that carborandum effectively suppresses conversion up to 450°C where conversion reaches a maximum at 4.2 %. The product profile (Figure 6.2) shows the selectivity of the cracked products (C_1-C_4 alkanes and alkenes – cracking refers to the formation of lower molecular weight alkanes and alkenes), oxygenates and C_8 olefins, decreases with an increase in temperature, whilst the selectivity to the carbon oxides, grouped as CO_x increases (Figure 6.3). The increase in selectivity to CO_x is expected due to combustion which occurs at higher temperatures. There is no CO formed at temperatures below 450°C.

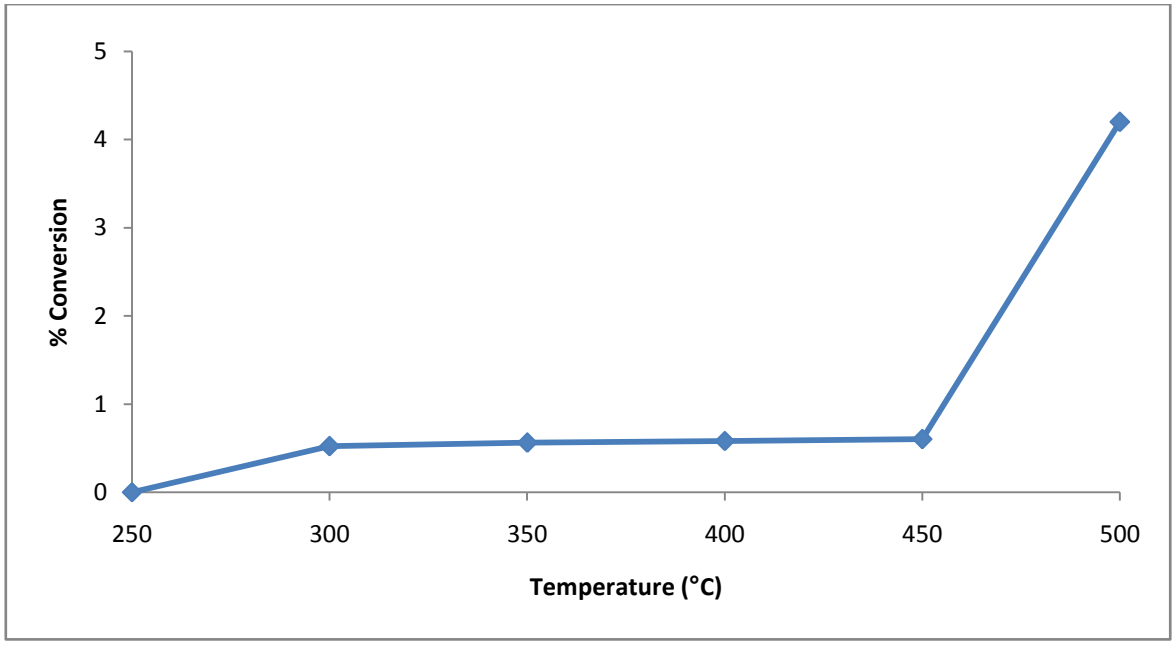

Figure 6.1: Conversion of *n*-octane as a function of temperature for the blank reactor experiment

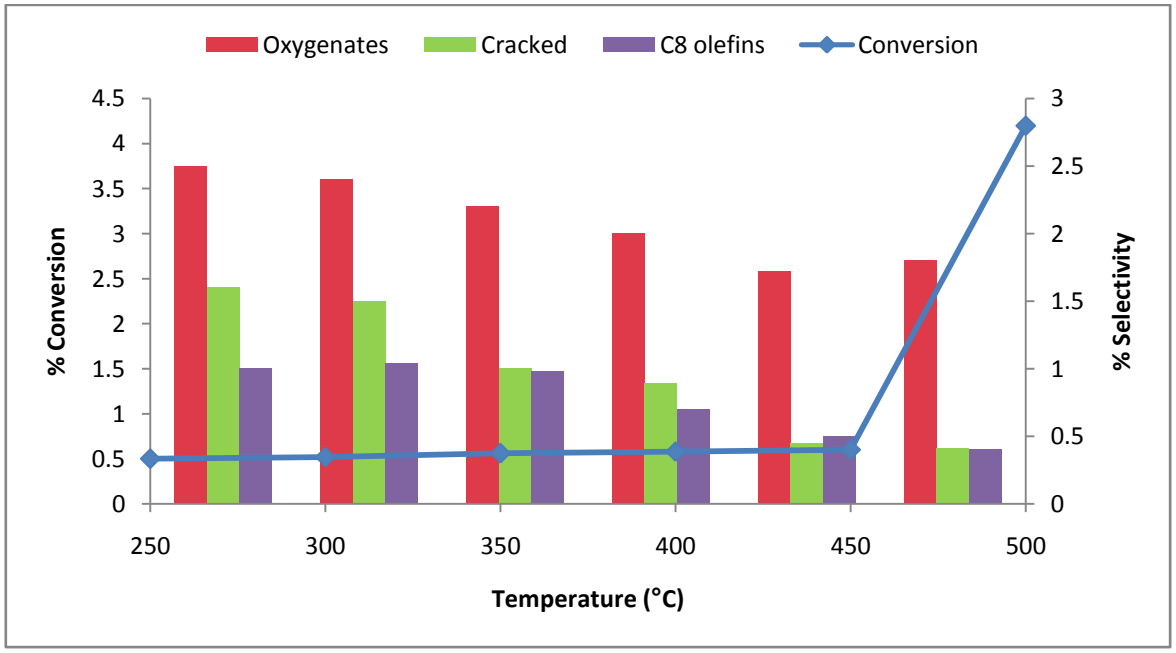

Figure 6.2: Product profile obtained for the blank reactor experiment

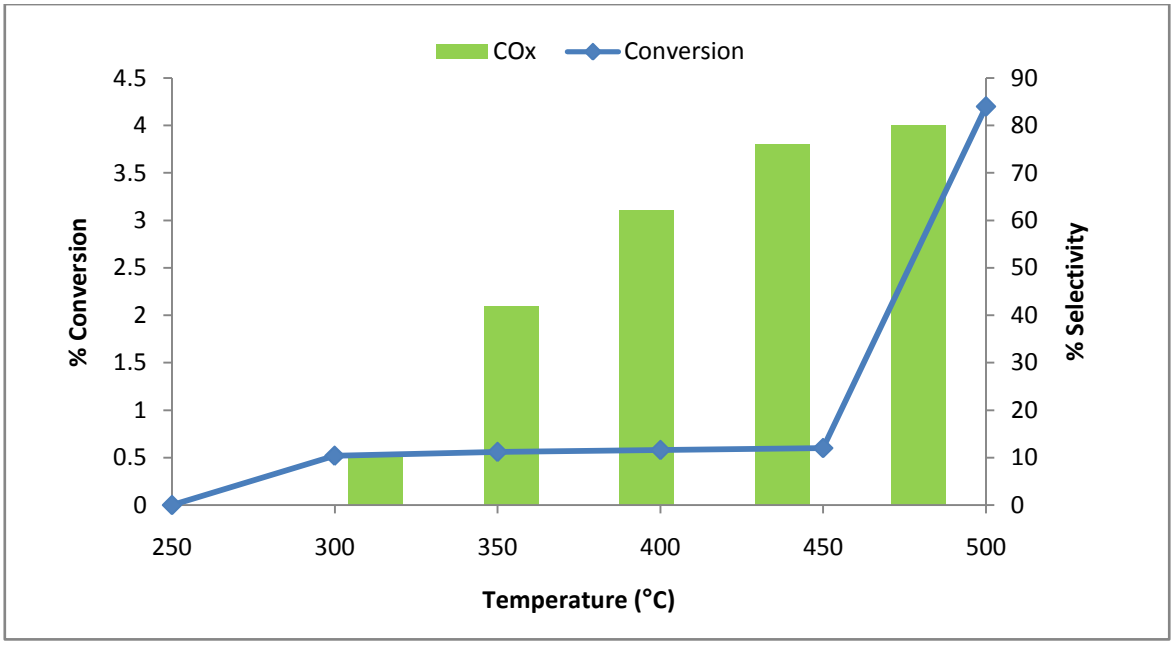

Figure 6.3: Selectivity to CO_x for the blank reactor experiment

6.2 *n*-octane activation over the nickel molybdate catalyst

6.2.1 Activation over α-nickel molybdate

The α-NM catalyst used in all reactions is the NM-A catalyst which was characterised and discussed in chapter 5. The effect of gas hourly space velocity (GHSV) on the conversion of *n*-octane and selectivity to the products obtained was investigated by varying the GHSV in a series of experiments. The fuel–air ratio was maintained constant at 30 % octane in air for each of the experiments. The general trend observed in Figure 6.4 is that the conversion of *n*-octane increases as temperature increases. Furthermore, there is a higher conversion of *n*-octane at the lower GHSVs which is clearly evident from 350°C onwards. This can be explained by the residence time spent by the feed on the catalyst. A lower GHSV (i.e. slower flow rate) results in a greater interaction between the feed and the surface of the catalyst which promotes a higher conversion as compared to that observed for higher GHSVs [3]. The conversion levels off between 450°C and 500°C. This behaviour is attributed to the reaction being conducted under fuel-rich conditions. The O_2:hydrocarbon ratio required for total combustion is 12.5 and only a 0.5 ratio was supplied. Initially an O_2:hydrocarbon ratio of 1 was tested for the above GHSVs which resulted in very high conversions (~95 %) and high

yields of CO_x. Therefore it was decided to limit the amount of oxygen entering the reaction. At higher temperatures (450°C-500°C) the liming reactant, oxygen, is exhausted and as the demand for this gas increases, the conversion remains constant [4-5]. For all reactions, the catalyst was stable within the temperature range tested.

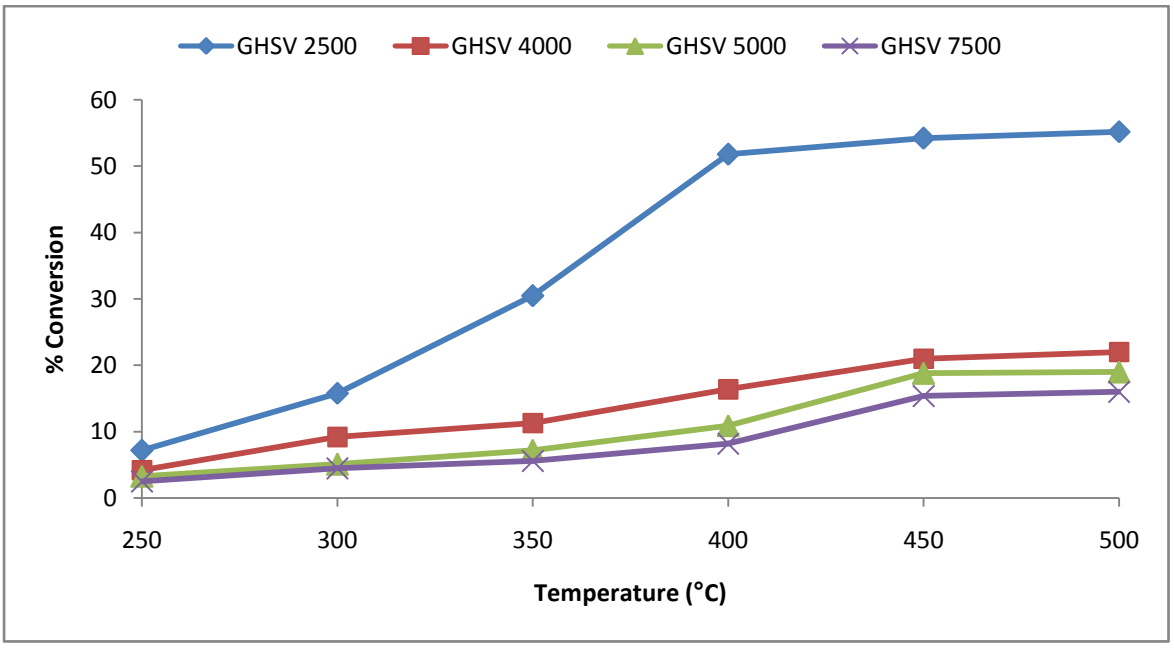

Figure 6.4: Effect of GHSV on conversion as a function of temperature

Figure 6.5 shows the selectivity to the cracked products and it can be seen that the lower reaction temperatures favour a higher selectivity. The general trend observed is the higher the GHSV the greater the selectivity to the cracked products with the exception being 4000 h^{-1} which has a significantly lower selectivity to cracked products than the other flow rates tested.

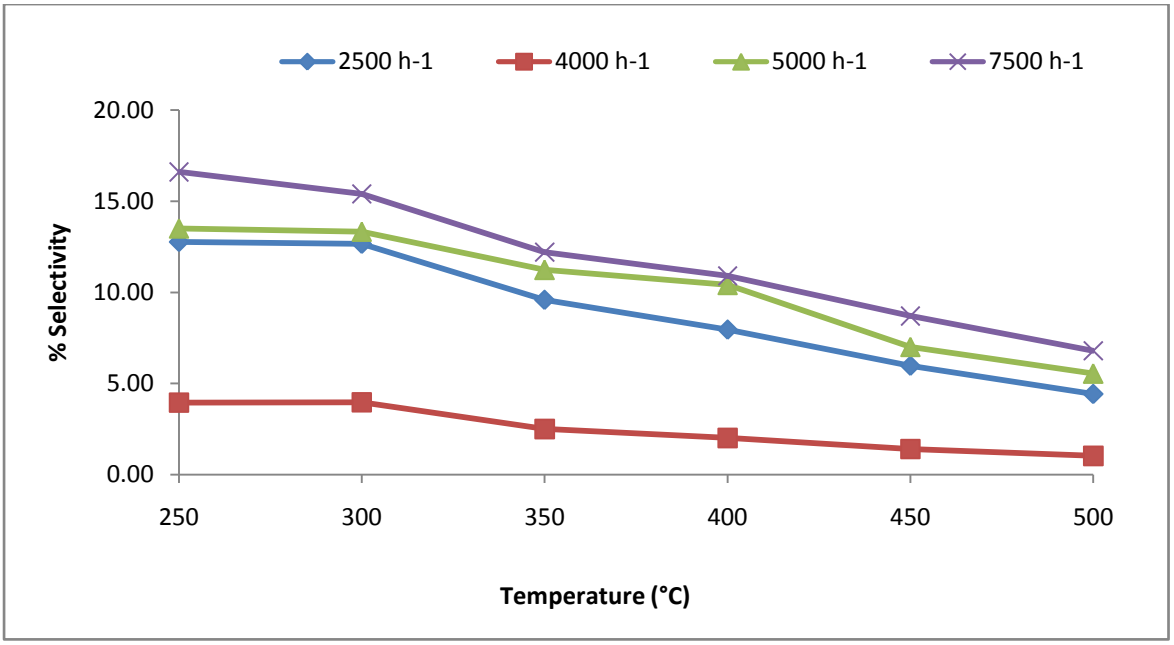

Figure 6.5: Selectivity to the total cracked products obtained at various GHSVs

The carbon oxides were significantly affected by variation in GHSV and temperature as shown in Figure 6.6. Higher temperatures tend to favour combustion and thus the formation of CO_x, as is known to be the case with nickel molybdate catalysts [6]. At all reaction temperatures CO_2 was found to be dominant over CO. It is well known that CO_2 is produced as a result of heterogeneous combustion [7]. There was no formation of CO at temperatures below 400°C for all GHSVs therefore from 250°C to 350°C there is a steady increase in production and selectivity to CO_2. The production of CO starts at 400°C and gradually increases up to 500°C whilst the CO_2 production slightly decreases at 400°C and thereafter remains approximately constant as temperature increases to 500°C. The exception to this trend is seen at the higher GHSV of 7500 h^{-1} where there is a decrease in production of CO_2 between 400°C to 500°C as the CO production steadily increases, leading to an overall decrease of CO_x production and a 10 % drop in selectivity. This ties in with the increase in selectivity to the total oxygenated products (Figure 6.7) between 400°C and 500°C (6.4 % to 16.5 % respectively).

Therefore it can be concluded that at a higher GHSV, as the flow of the reactants speeds up, there exists a shorter residence time of the reactants over the catalyst surface and there is a synergistic decrease in production and selectivity to combustion products with an increase in

selectivity to oxygenates. The selectivities to oxygenates, at the lower GHSVs, decrease with an increase in temperature. The selectivity to aromatics and C_8 hydrocarbons was, in all cases, minimal and always less than 2% (Table 6.1). The unidentified cyclics, aromatics and dienes were grouped together as 'others'.

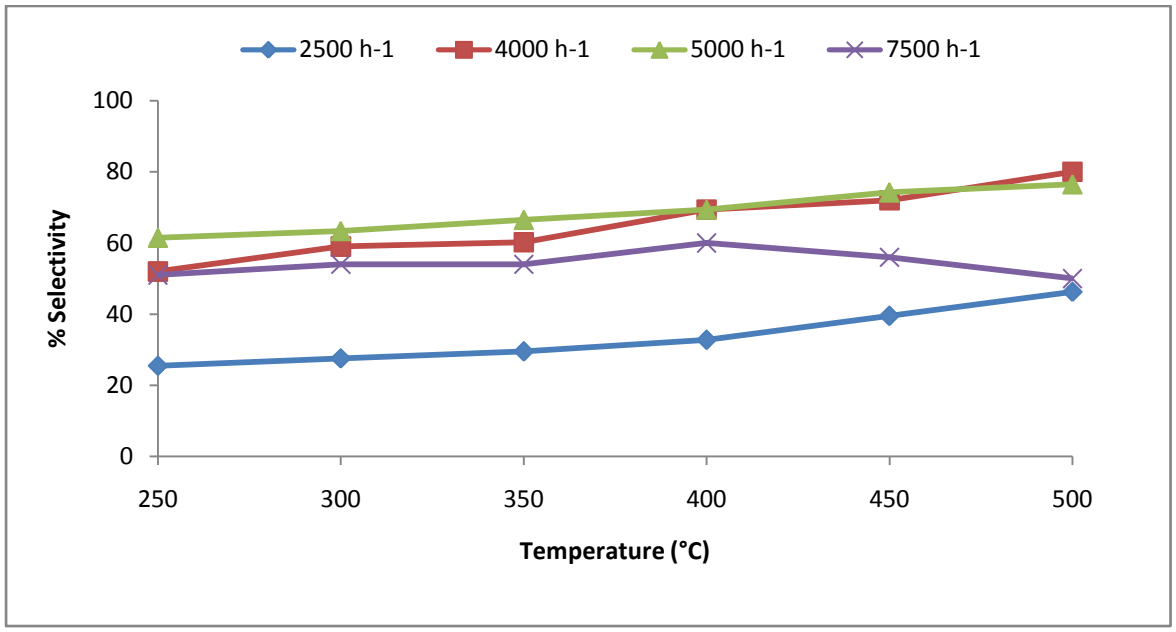

Figure 6.6: Effect of GHSV on selectivity to total CO_x as a function of temperature

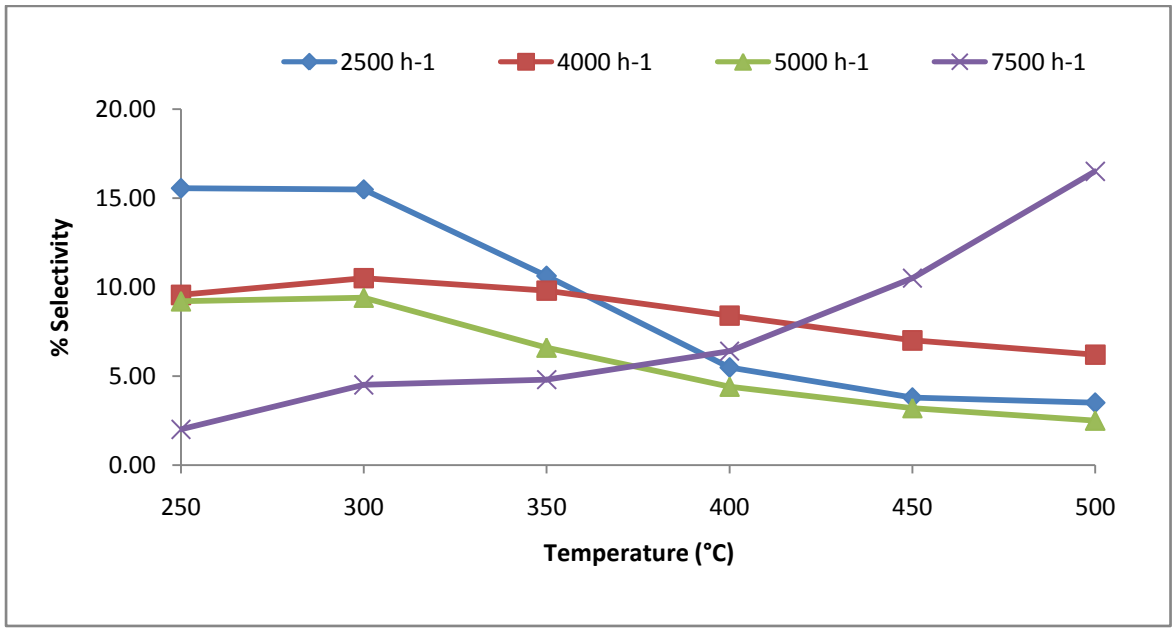

Figure 6.7: Effect of GHSV on selectivity to total oxygenates as a function of temperature

Table 6.1: [a]Selectivity to products at various GHSVs at 300°C

GHSV (h^{-1})	% Selectivity		
	Aromatics	**[b]Other C_8 hydrocarbons**	**[c]Others**
2500	2.44	0.29	37.31
4000	0.60	0.86	13.20
5000	0.47	1.69	14.50
7500	0.24	2.00	18.50

[a]*Excluding CO_2, oxygenates and C_8 olefins which are presented in Figures 6.5 – 6.8*

[b]*Excluding C_8 olefins which are grouped by themselves*

[c]*Unidentified cyclics, aromatics and dienes*

Figure 6.8 shows the highest selectivity to C_8 olefins, which are the major products of interest, was achieved at 300°C at a GHSV of 4000 h^{-1} (7.1 % selectivity at 9.5 % conversion). Table 6.1 shows the selectivity to aromatics and other C_8 hydrocarbons to be minimal at this temperature and flow rate. In addition, the selectivity to the unidentified products, grouped as 'others' were found, in comparison to the other flow rates, to be minimal at 13.2%.

Figure 6.9 compares the product profiles at the various flow rates at 300°C. The selectivity to the cracked products at 4000 h^{-1} is minimal, at 3.7 % in comparison to the other flow rates. There is, in addition to the C_8 olefins, a significant selectivity to oxygenates (10.5 %) at this flow rate. Therefore, it was decided to carry out the comparative study of the catalytic activity of the molybdate, CNT and the supported catalyst at 300°C, as this was found to be the optimum temperature for the selectivity to C_8 olefins in addition to a significant amount of oxygenates.

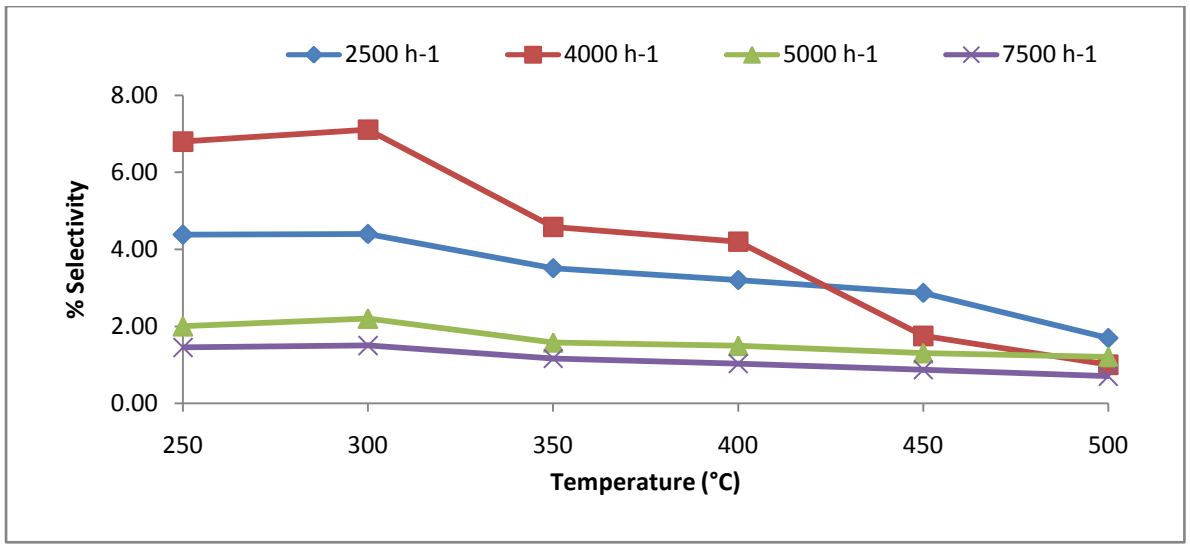

Figure 6.8: Effect of GHSV on total selectivity to C_8 olefins as a function of temperature

Steady state conditions were maintained for 12 hours on stream and isoconversion of 10 % was obtained. After 24 hours on stream (refer to Table 6.2) the conversion dropped to 5.6 % and the selectivity to all major products decreased whilst that of CO_2 increases from 67.5 % to 94.5 %. It can therefore be deduced that the α-phase starts to deactivate after 12 hours. The reason for this is catalyst coking which is discussed in detail in the spent catalyst characterisation section further on in the chapter (refer to Table 6.3).

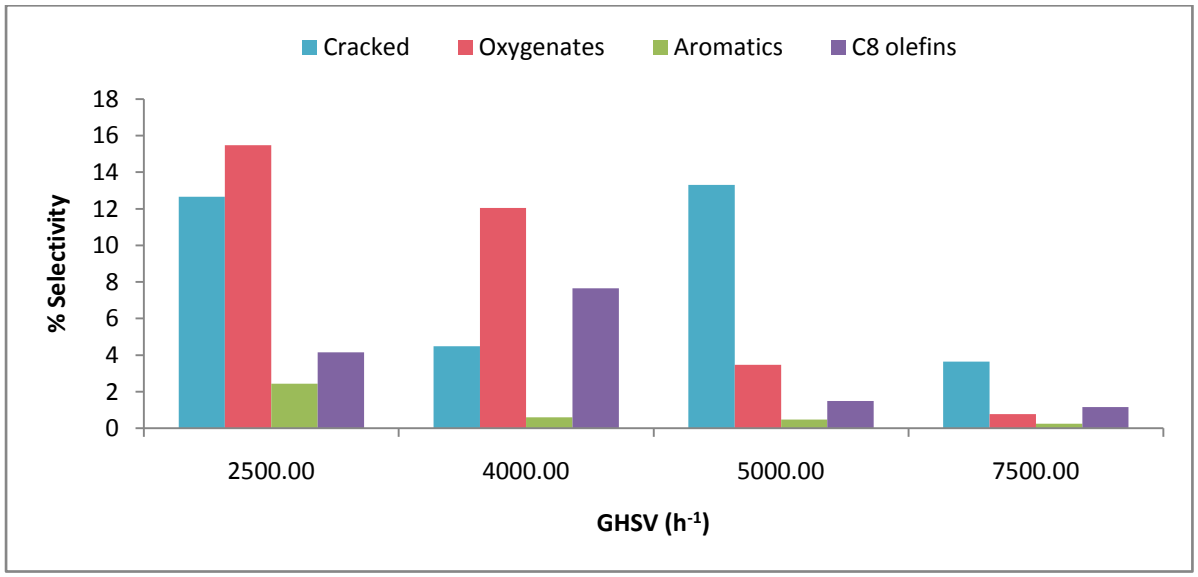

Figure 6.9: Product profile at various GHSVs at 300°C

Table 6.2: Selectivity to products at 4000 h^{-1} at 300°C as a function of time on stream

Catalyst	Time (h)	% X	% Selectivity					
			Cracked	**Oxygenates**	**Aromatics**	**C_8 olefins**	**CO_2**	**Others**
α-NM	12	10.0	4.70	13.0	0.50	7.00	67.5	6.90
	24	5.60	1.20	2.30	0	1.20	94.5	0.80

The x-ray diffractograms of the spent catalysts shown in Figure 6.10 show the α-$NiMoO_4$ phase to be preserved from 300°C to 400°C and a phase change occurs at both 450°C and 500°C. The phases present at 450°C are MoO_2 (2θ = 26.11° and 51.1°) JCPDS 32-671, nickel (2θ = 44.63° and 79.34°) JCPDS 4-850 and NiO (2θ = 62.72° and 74.61°) JCPDS 4-835, in addition to α-$NiMoO_4$ JCPDS 33-948. The phases present at 500°C are MoO_2 (2θ = 25.89° and 29.37°) and Ni (2θ = 44.76°, 52.13° and 76.40°). The diffractograms of these spent catalysts correspond to that of the nickel molybdate reduced under hydrogen at 450°C and 500°C discussed in Chapter 5, Figure 5.6. Therefore the active phase of the catalyst changes between 450°C and 500°C and is no longer purely α-$NiMoO_4$.

It can be deduced that at 450°C the gaseous *n*-octane passing over the catalyst surface reduces part of the catalyst to a mixed phase of MoO_2, NiO and Ni. A further increase in temperature to 500°C reduces the catalyst to only the MoO_2 and Ni phases. These higher temperature phases are not selective to C_8 olefins and oxygenates, produce small amounts of cracking products and display an increase in selectivity to CO_x. The exception is found at a flow rate of 7500 h^{-1} where there exists an increase in selectivity to oxygenates and a drop in selectivity to CO_x between 400°C and 500°C.

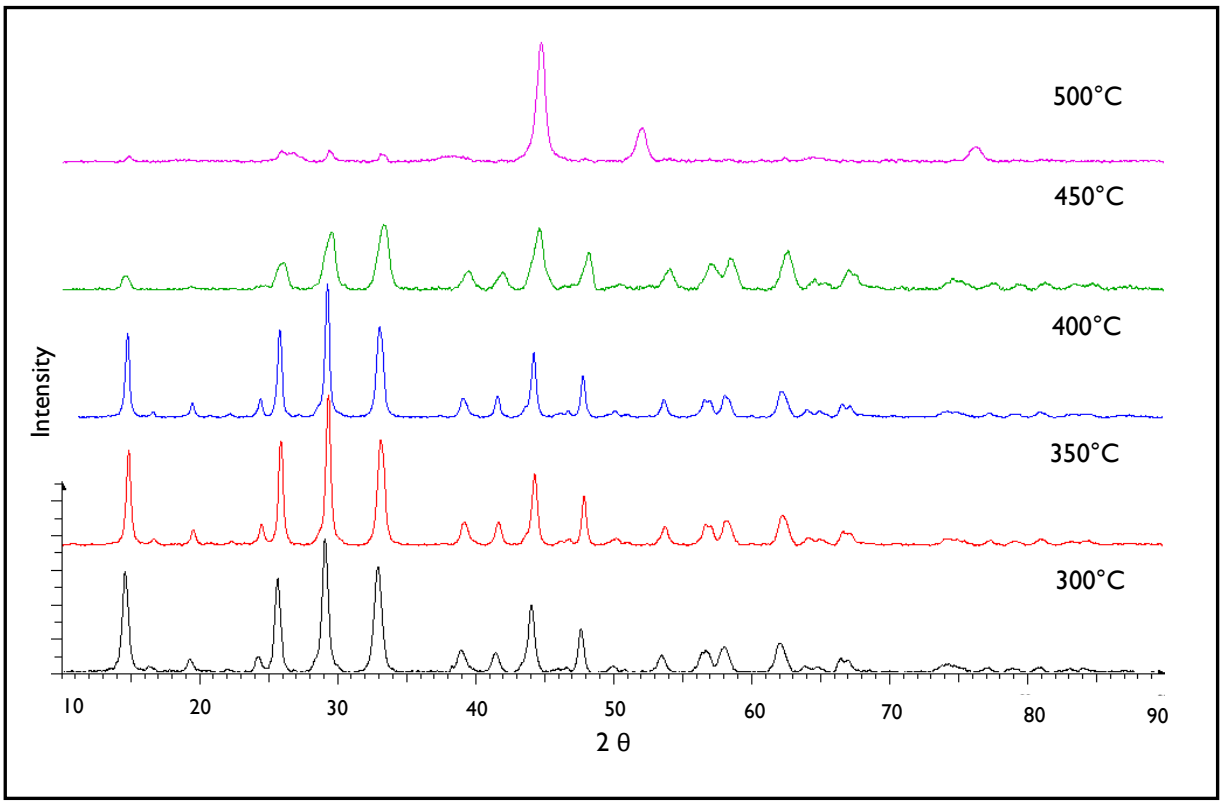

Figure 6.10: Powder XRD of spent α-NM catalysts isolated at temperatures from 300°C-500°C at GHSV 4000 h^{-1}

The BET surface areas and pore volumes of the spent catalysts, together with their calculated crystallite size, are shown in Table 6.3. It can be seen that at 300°C the surface area, pore volume and crystallite size of the spent catalyst is unchanged from the fresh catalyst. It can be concluded that at 300°C the active sites of the catalysts arise from a pure α-$NiMoO_4$ phase which results in the optimal selectivity to C_8 olefins. The crystallite size increases between 350°C and 400°C as the surface area and pore volume correspondingly decrease. This is expected as smaller crystallites will have a larger surface area as compared to a larger single crystallite.

Coking can block access of the reactant to the interior pores of the catalyst. Coke is hydrogen deficient carbonaceous residue on the catalyst surface having an empirical formula of CH. The decrease in surface area and pore volume of spent α-NM between 300°C and 400°C is attributed to the deposition of coke on the catalyst surface which blocks access to the active sites and clogs the pores (refer to Table 6.4). As the reaction temperature increases the

limiting reactant, oxygen is depleted. Coking of a catalyst most often occurs when no oxygen is available [8]. Thus it follows that there is a decrease in selectivity to C_8 olefins and oxygenates as temperature increases. The onset of phase change at 450°C is accompanied by an increase in surface area and pore volume and a corresponding decrease in crystallite size. A possible reason for this is this is the reduced extent of coke deposition on the catalyst at this temperature.

Table 6.3: Surface area, pore volume and crystallite size of spent α-NM

Temperature (°C)	BET Surface area (m^2/g)	BET Pore volume (cm^3/g)	[a] XRD Crystallite size (nm)
25	45.7	0.30	193.0
300	45.7	0.30	193.0
350	43.4	0.23	200.4
400	35.8	0.20	226.7
450	38.3	0.25	92.0
500	42.4	0.26	129.5

[a]*Calculated using the Scherrer equation from FWHM of highest intensity peak*

The TGA curve in Figure 6.11 shows a 5 % weight loss in the temperature range of 377°C-462°C and a 0.2 % loss between 597°C-623°C which are attributed to coke. The loss of coke within the temperature range of 377°C-462°C suggests that at higher temperatures there is a lesser degree of coke deposition as it is burned off. Furthermore, the increase in surface area and pore volume of the spent catalysts between 450°C-500°C as compared to that between 350°C-400°C supports this argument. Note that even though the crystallite size of the catalysts between 450°C-500°C is significantly smaller than that between 350°C-400°C a comparison between the surface areas and respective pore volumes cannot be drawn as the

phases of the catalysts are different. In all experiments carried out there was no leaching of the metal species as the ratios of Ni:Mo are preserved at one as determined by ICP-OES.

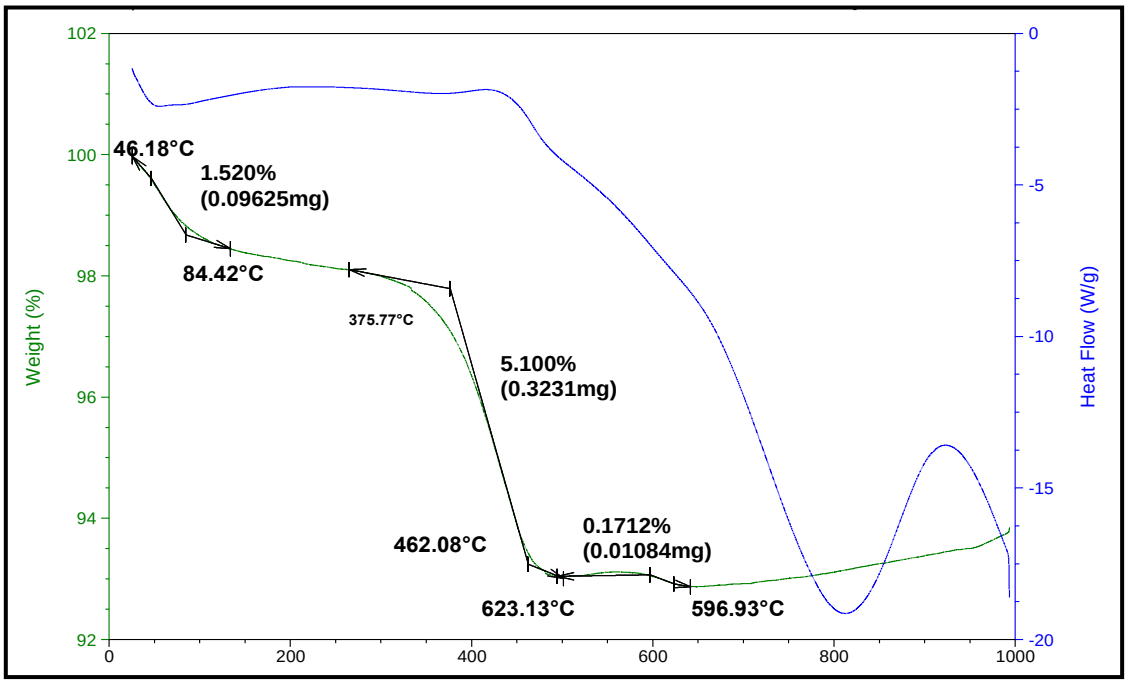

Figure 6.11: TGA-DSC curve of spent α-NM at 300°C

Table 6.4: Metal distribution and extent of coke deposition of α-NM

Catalyst	Temperature (°C)	ICP	
		% C	Ni:Mo
Spent	300	5.2	1
Spent	350	6.1	1
Spent	400	6.8	1
Spent	450	0.8	1
Spent	500	0.6	1

The SEM and TEM images of the spent nickel molybdate, represented in Figure 6.12 a and b respectively, show the surface structure of the spent catalyst to remain unchanged as shown by the rounded porous morphology of the SEM image and the elongated rod-like structure seen in the TEM image (refer to Figures 5.10 and 5.11 for pre-reaction images).

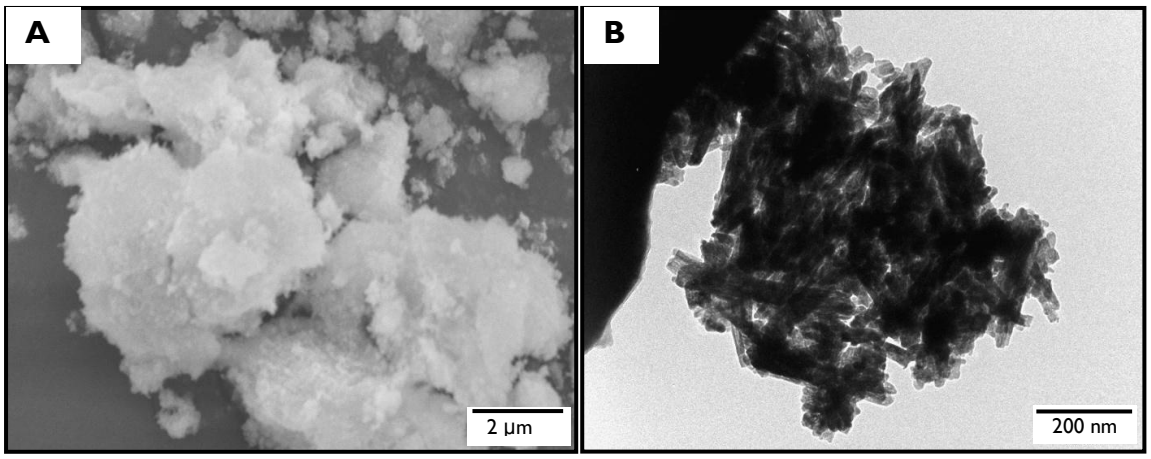

Figure 6.12: SEM (a) and TEM (b) images of spent α-NM at 300°C

6.2.2 Activation over β-nickel molybdate

The high temperature β-phase, which was generated *in situ* from the α-phase (section 4.2.2), was found to be more selective to C_8 olefins, oxygenates and other hydrocarbons than the α-phase when tested at the same conditions (4000 h^{-1} and 300°C). The increase in selectivity to oxygenates and C_8 olefins obtained over the β-phase (Table 6.5) is accounted for by the lower CO_2 selectivity. There is a 3 % increase in selectivity to 1-octene and to methanol at 9 % conversion when comparing the β-phase to the α-phase. The catalyst is stable on stream for 24 hours and steady state is maintained for this duration. There was no sign of deactivation as in the case of the less selective α-phase. The high temperature β-phase, once generated *in situ*, is only stable at temperatures above 250°C and reverts back to the α-phase on cooling [9]. Therefore the spent catalyst characterisation (IR-ATR, powder XRD, SEM and TEM) display the same results as that of the α-phase. The ODH of paraffins is governed by the Mars-van Krevelen mechanism, discussed in Section 1.5, which states that lattice oxygen plays a crucial role in the oxidation of alkanes [10]. The higher selectivity obtained over the β-phase is related to the molybdenum oxygen coordination (section 2.6). The β-phase has a

higher rate at which lattice oxygen is consumed (or reduction rate) relative to the α-phase [6]. Results based on isothermal reduction data show that small amounts of oxygen can be removed from the β-phase catalyst and restored in less time as compared to the α-phase, resulting in a faster redox cycle and a more selective catalyst [6]. Not that the β-phase of the supported catalyst could not be generated as the CNTs decompose at higher temperatures, especially when implemented as a support (refer to section 5.3.8).

Table 6.5: Selectivity to products at 4000h^{-1} at 300°C over α and β-nickel molybdate

Catalyst	**Time (h)**	**% X**	**% Selectivity**					
			Cracked	**Oxygenates**	**Aromatics**	**C_8 olefins**	**CO_2**	**Others**
α-NM	12	10.0	4.70	13.0	0.50	7.00	67.5	6.90
	24	5.60	1.20	2.30	0.00	1.20	94.5	0.80
β-NM	12	9.00	4.98	15.7	1.00	12.2	59.4	5.98
	24	9.00	4.98	15.7	1.00	12.2	59.4	5.98

6.3 *n*-octane activation over carbon nanotubes and carbon nanotube supported nickel molybdate

The catalytic activation of *n*-octane over carbon nanotubes at 300°C and GHSV 4000h^{-1}, represented in Figure 6.13, resulted in a steady state being obtained for 16 hours on stream. The conversion of *n*-octane achieved was 10.3 %. The highest selectivity was that to CO_x at 43.4 % and there was a good selectivity to the desired C_8 olefins and oxygenates at 11.3 % and 27.7 % respectively. There was a minimal selectivity to cracking products, aromatics and C_8 hydrocarbons and 11 % of the product distribution is attributed to others (unidentified cyclics, dienes and aromatics).

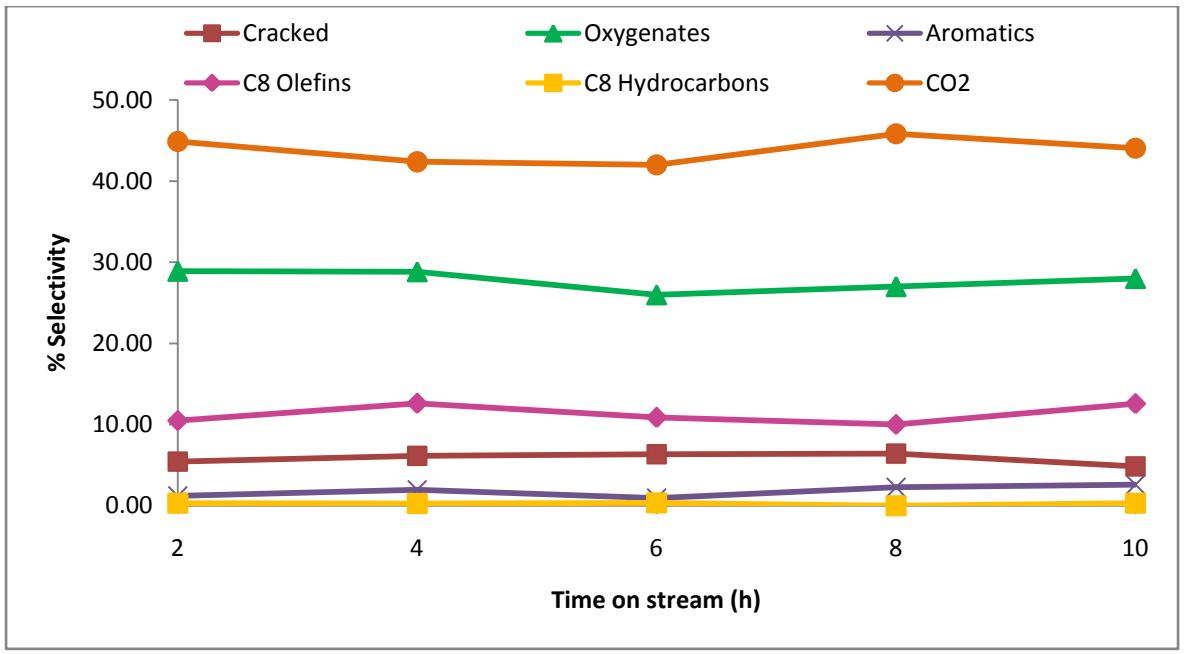

Figure 6.13: Product distribution over the CNT catalyst obtained at 300°C as a function of time on stream

Table 6.6 shows that after 24 hours on stream the conversion dropped to 6.4 % with a 97 % selectivity to CO_2 and a 1.6 % selectivity to oxygenates. The selectivities to C_8 olefins, aromatics, cracked products and others were less than 1%.

Table 6.6: Selectivity to products at 4000h^{-1} at 300°C after 24 hours on stream

Catalyst	Time (h)	% X	% Selectivity					
			Cracked	Oxygenates	Aromatics	C_8 olefins	CO_x	Others
CNT	12	10.3	5.80	28.0	0.45	11.3	42.8	11.0
	24	6.40	0.41	1.61	0.02	0.42	97.0	0.55
α-NM-CNT	12	10.0	6.40	21.0	2.00	15.6	51.0	4.00
	24	8.90	6.30	20.9	1.80	6.90	50	11.2

It is possible that the CNTs had coked and it was this deposition of coke on the surface of the catalyst which blocked the active sites. Figure 6.14 (a) and (b) are the TEM images of the spent CNT. Amorphous material deposited on the CNT surface can be seen (Figure 6.14 a) and this material is most possibly amorphous carbon produced as a result of the catalyst coking. The material can also be seen to exist as clusters, some displaying a hexagonal shape (Figure 6.14 b). The TEM image of spent α-NM-CNT Figure 6.15 is similar to the fresh catalyst but the CNTs display some mechanical damage which is most probably as a result of crushing during pelletizing and sieving.

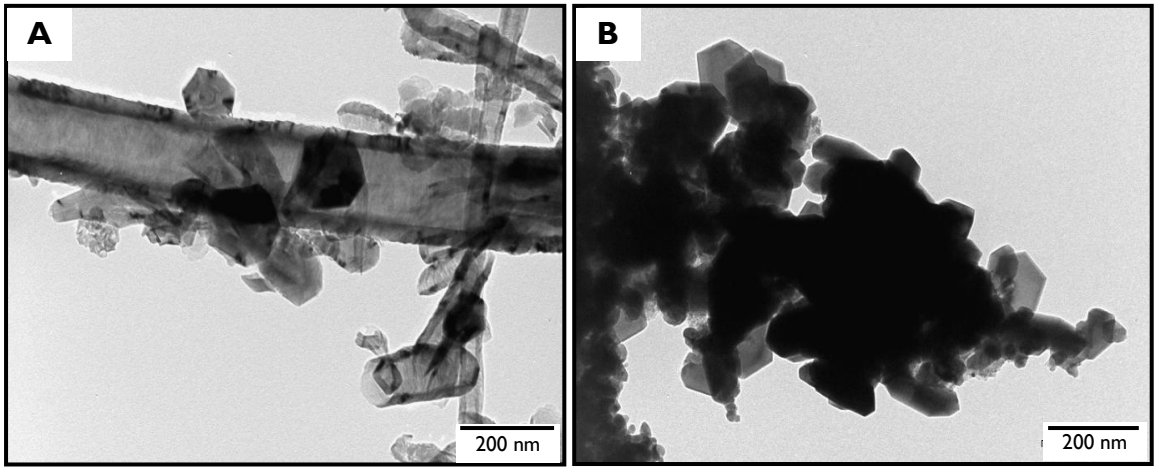

Figure 6.14: TEM images of spent CNT

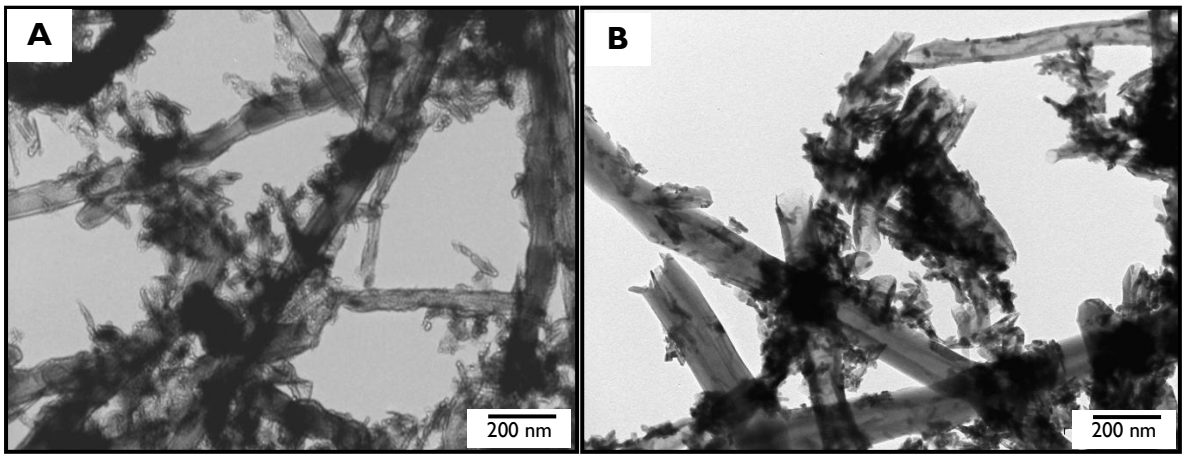

Figure 6.15: TEM images of (a) fresh and (b) spent α-NM-CNT

The powder XRD of the spent CNT, seen in Figure 6.16, shows a change in structure as the doublet which represents the 100 plane between 42.5° and 44° and the peak at 50° are no longer present. This indicates a loss in crystallinity of the material. The decrease in surface area and pore volume represented in Table 6.7 support the fact that coking has occurred and the pores of the active sites are blocked as a result.

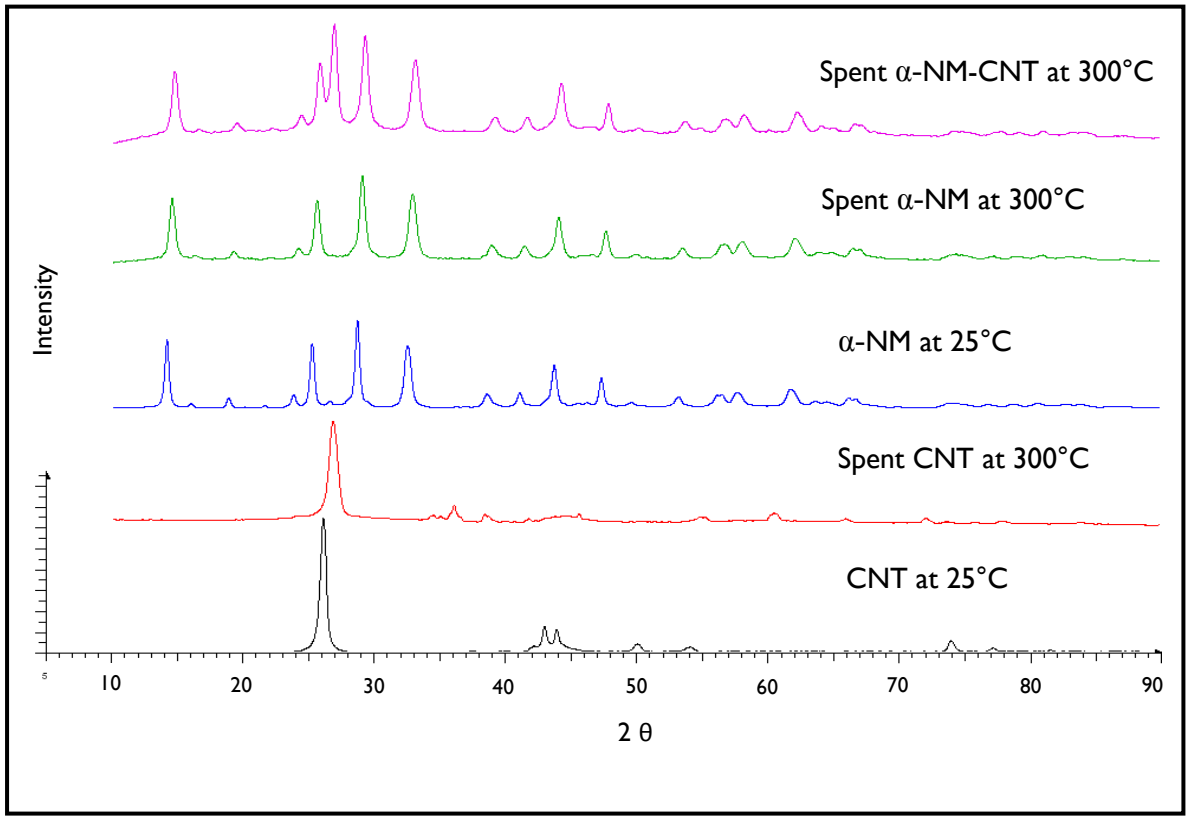

Figure 6.16: Powder x-ray diffractograms comparing fresh and spent catalysts

Table 6.7: Metal distribution and extent of coke deposition of CNT and α-NM-CNT

Catalyst	Temperature (°C)	Surface area (m^2/g)	Pore volume (cm^3/g)	Crystallite size (nm)
Fresh CNT	25	72.5	0.32	143.3
Spent CNT	300	24.2	0.08	104.4
Fresh α-NM-CNT	25	52.0	0.29	174.2
Spent α-NM-CNT	300	38.5	0.18	167.0

Figure 6.17 shows the selectivity to the products obtained, as a function of time on stream, via catalytic activation using the supported catalyst α-NM-CNT. A further comparison between the catalysts is made in Section 6.4. The catalyst is steady on stream for 24 hours, maintaining the conversion at 9.6 %. This is a noteworthy result as the α-NM catalyst is stable on stream for 12 hours before it deactivates and the CNT catalyst is stable for 16 hours before deactivating under the same conditions. Furthermore, the selectivity to cracked products, oxygenates, aromatics and C_8 hydrocarbons remains constant, however, the selectivity to 1-octene decreases from 4.6 % at 12 hours on stream to 0.5 % after 24 hours on stream. Similarly the selectivity to CO_2 increases from 50 % at 12 hours on stream to 55.1 % after 24 hours on stream. Previous studies have found that the interaction of the feed with the catalyst surface is weaker for a more basic surface, which reduces complete oxidation of the desired products to CO_x [11]. The nickel molybdate catalyst, which is only slightly basic, favours a limited desorption of the olefin products from the catalyst surface. The residence time spent by the olefins on the catalyst surface dictates whether oxygen insertion or complete oxidation occurs. It is well known that the ODH of paraffins over nickel molybdate catalysts occur via the Mars-van Krevelen mechanism as discussed in Chapter 1 [12]. It can therefore be concluded that 1-octene undergoes complete oxidation to CO_2 after 24 hours on stream.

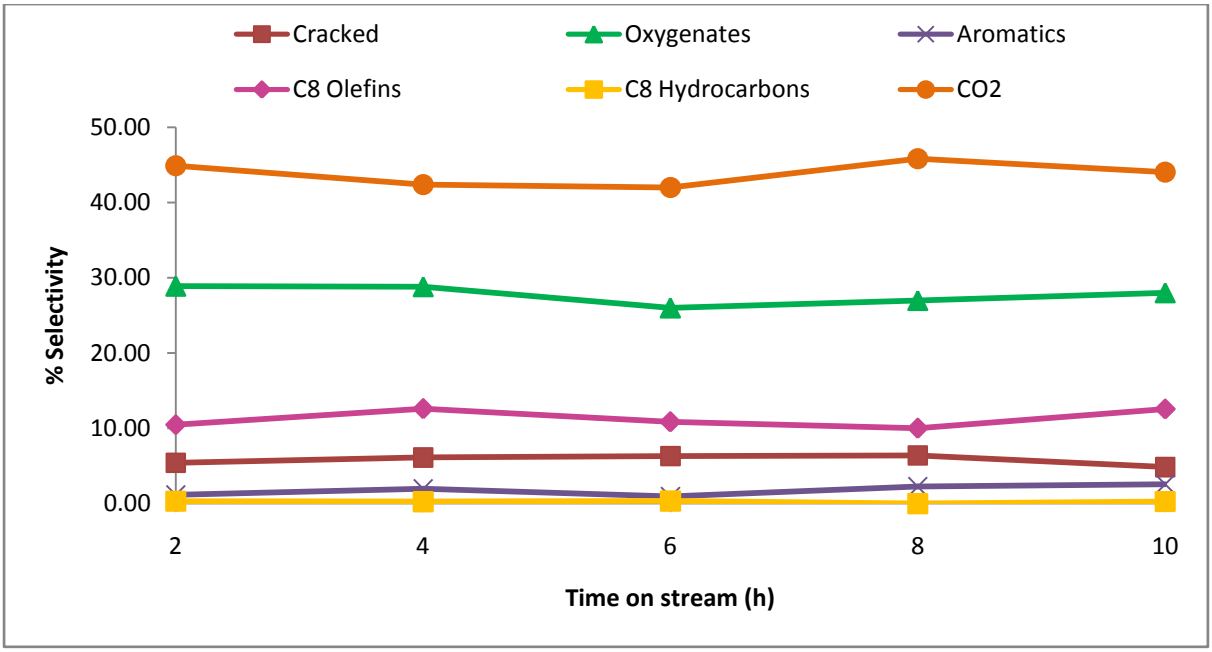

Figure 6.17: Product distribution over α-NM-CNT catalyst obtained at 300°C as a function of time on stream

6.4 Comparison at isoconversion

Comparison of the catalysts at isoconversion and under isothermal conditions (10 % conversion at 300°C) is represented in Figures 6.18 and 6.19. The reactions catalysed by carbon nanotubes result in a decrease in selectivity to CO_2 and cracked products and increase in selectivity to oxygenates and C_8 olefins when compared to the nickel molybdate catalyst. Furthermore there is a significant increase in the selectivity to certain products of interest represented in Figure 6.25: 12 % selectivity to methanol, 4.85 % to 2-propanol, 2.4 % to butanone and 7 % to 1,7 octadiene. The supported catalyst α-NM-CNT shows a decrease in selectivity to CO_2 at 51.6 % as compared to the α-NM catalysts alone which has a selectivity of 67.5 %. The CNT catalyst yielded 43.4 % selectivity to CO_2.

Since the nickel molybdate was found to produce a large amount of CO_2 it follows that the supported α-NM-CNT catalyst produces more CO_2 than the CNT alone. The supported catalyst gives the highest selectivity to the C_8 olefins as represented in Figure 6.25: 8.1 % to

1,7 octadiene, 4.6 % to 1-octene and 3.0 % to cis-2-octene. The selectivity to the cracked products for all three catalysts are approximately constant at 4.0 %.

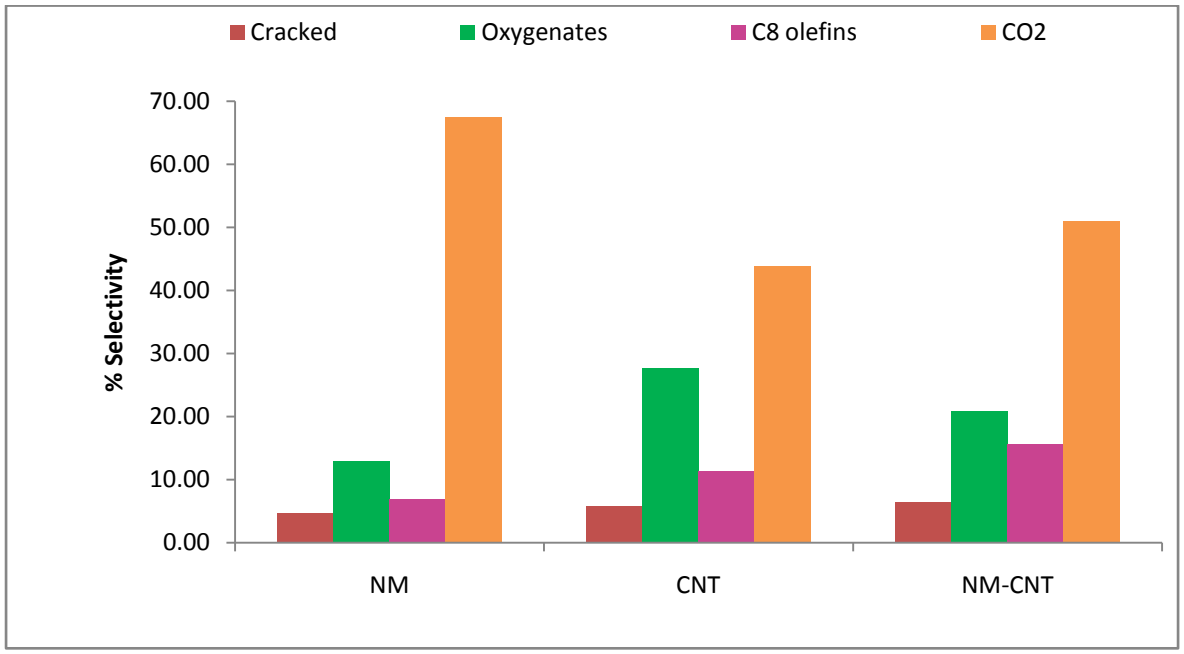

Figure 6.18: Comparison of selectivity at 10 % isoconversion

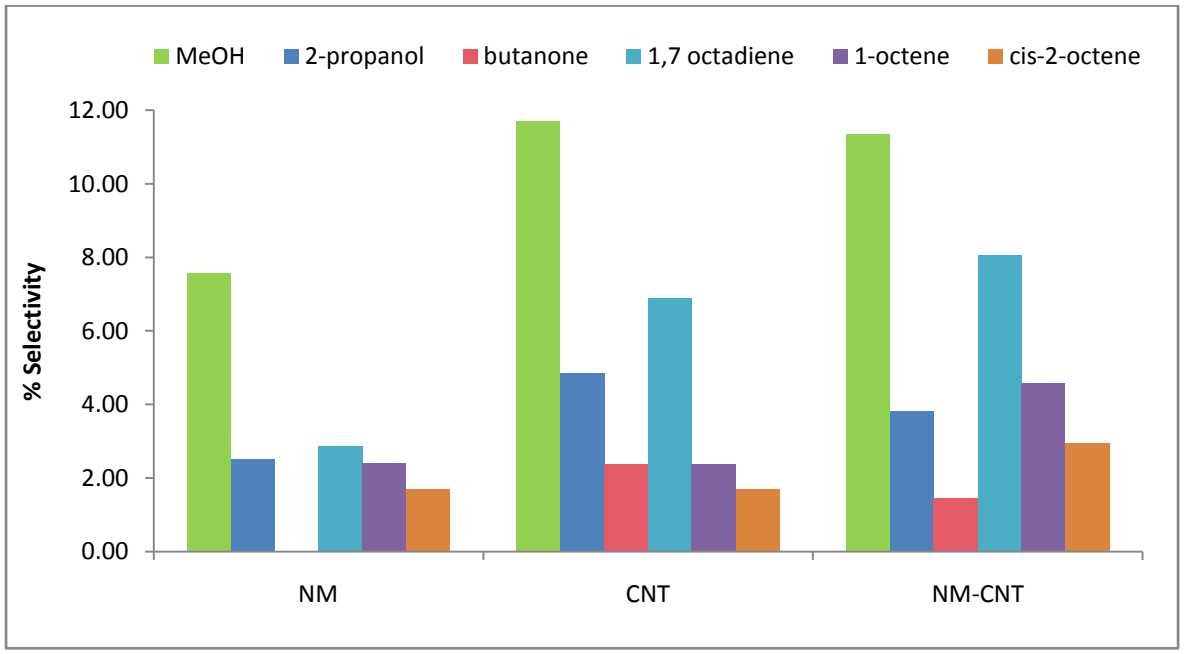

Figure 6.19: Comparison of selectivity to major products at 10 % isoconversion

It can be concluded that, at isoconversion and under isothermal conditions, carbon nanotubes were found to be the more active catalysts and they were more selective towards the oxygenates: methanol, 2-propanol and butanone and the C_8 olefins: 1,7 octadiene, 1-octene and cis-2-octene. Furthermore, CNTs were found to be 16 % less selective to CO_2 than nickel molybdate. The supported catalyst, α-NM-CNT, is 9 % more selective to the C_8 olefins than nickel molybdate and 4.3 % more selective than the carbon nanotubes. In addition to this the supported catalyst produces 17 % less CO_2 than nickel molybdate alone.

6.6 References

[1] Marengo, S., Comotti, P., Galli, G., *Catalysis Today*, 2003, **81**, 205.

[2] Vislovskiy, V.P., Suleimanov, T.E., Sinev, M.Y., Tulenin, Y.P., Margolis, L.Y., Corberan, V.C., *Catalysis Today*, 2000, **61**, 287.

[3] Friedrich, H.B., Mahomed, A.S., *Applied Catalysis A: General*, 2008, **347**, 11.

[4] Burch, R., Crabb, E., *Applied Catalysis A: General*, 1993, **100**, 111.

[5] Friedrich, H.B., Govender, N., Mathebula, M.R., *Applied Catalysis A: General*, 2006, **297**, 81.

[6] Kaddouri, A., Del Rosso, R., Mazzochia, C., Fumagalli, D., *Journal of Thermal Analysis and Calorimetry*, 2001, **63**, 267.

[7] O'Connor, R. P., Schmidt, L.D., *Chemical Engineering Science*, 2000, **55**, 5693.

[8] Maldonado-Hódar, F.J., Madeira, L.M., Portela, M.F., Martín-Aranda, R.M., Freire, F., *Journal of Molecular Catalysis A: Chemical*, 1996, **111**, 313.

[9] Madeira, L. M., Portela, M.F., *Catalysis Reviews Science and Engineering*, 2002, **44**, 247.

[10] Vedrine, J.C., Coudurier, G., Millet, J.M.M., *Catalysis Today*, 1997, **33**, 3.

[11] Pillay, B., *A study of nickel molybdenum oxide catalysts for the oxidative dehydrogenation of n-hexane*, Ph.D. Thesis, University of KwaZulu -Natal, 2009.

[12] Zou, J.Y., Schrader, G.L., *Thin Solid Films*, 1998, **324**, 52.

Chapter 7: Summary and Conclusion

This project involved the synthesis and characterisation of nickel molybdate catalysts. The potential of commercially available multi walled carbon nanotubes were investigated as a catalytic support for nickel molybdate and as a catalyst for the ODH of *n*-octane in a plug-flow fixed-bed reactor. The successful supporting of a stoichiometric α-$NiMoO_4$ catalyst on carbon nanotubes is to our knowledge novel.

Stoichiometric nickel molybdate was successfully synthesised by co-precipitation and contained a Ni:Mo ratio of 1. The pH, as well as precipitation and filtration temperatures were found to be crucial parameters which need to be finely controlled in order to obtain the α-phase. The phase transition from an octahedrally coordinated α-phase to the tetrahedrally coordinated β-phase was observed by reducing the α-phase in air and re-oxidising the intermediate phase by means of *in situ* XRD. Reduction of the catalyst by hydrogen gas produced a phase transition at 500°C which is allocated to MoO_2 and metallic nickel. Re-oxidation of the reduced catalyst in air resulted in an onset of change in phase at 300°C and at 600°C pure β-phase was present.

The MWCNTs were functionalised in order to introduce hydrophilicity to the material and provide anchoring sites for the metal catalyst. As this was a novel attempt of supporting stoichiometric α-$NiMoO_4$ on MWCNTs three different approaches were taken. Homogeneous deposition precipitation (HDP), wet impregnation and co-precipitation were investigated as methods of preparing the supported catalyst. Both HDP and wet impregnation were unsuccessful as the catalyst stoichiometry was lost. Co-precipitation, however, resulted in the $NiMoO_4$ catalyst being successfully supported on the CNTs and SEM showed the particle distribution on the CNT surface to be clustered.

The catalytic testing showed that both the $NiMoO_4$ and CNTs (unsupported) were catalytically active for the ODH of *n*-octane. A range of flow rates (2500 h^{-1} – 7000 h^{-1}) and temperatures (250°C-500°C) were tested using the α-$NiMoO_4$ catalyst and the optimal conditions for the production of oxygenates (MeOH, 2-propanol and butanone) and C_8 olefins (1,7 octadiene, 1-octene and cis-2-octene) were obtained at 4000 h^{-1} and 300°C. At isoconversion and under isothermal conditions α-$NiMoO_4$ yielded a 13.0 % selectivity to total

oxygenates, 7.0 % selectivity to total C_8 olefins and 67.5 % selectivity to COx. Steady state was maintained for 12 hours on stream and after 24 hours the conversion dropped to 5.6 %, while the selectivity to COx increased to 94.5 % due to the catalyst coking. This was observed by the spent catalyst becoming hard and black accompanied by a significant decrease in surface area and pore volume. The β-phase was generated *in situ* and found to be catalytically more active and selective than its lower temperature counterpart with steady state being maintained for 24 hours on stream at 9.0 % conversion. The total selectivity to oxygenates, C_8 olefins and COx obtained was 15.7 %, 12.2 % and 63.8 % respectively.

The reactions catalysed by carbon nanotubes resulted in a decrease in selectivity to CO_2 (43.4 %) and cracked products and increase in selectivity to oxygenates (18.92 %) and C_8 olefins (10.65 %) when compared to the nickel molybdate catalyst.

The supported catalyst NM-CNT showed a decrease in selectivity to CO_2 of 51.6 % as compared to the NM catalysts alone and yields the highest selectivity to the total C_8 olefins at 15.6 %.

Appendix 1: List of chemicals

Reagents

A 1.1: Chemicals used to prepare the nickel molybdate catalyst

Chemical Name	Chemical Formula	Purity	Supplier
Nickel nitrate hexahydrate	$Ni(NO_3)_2.6H_2O$	≥ 98.0%	Merck
Ammonium heptamolybdate	$(NH_4)Mo_7O_{24}.4H_2O$	≥ 99.5%	Merck
Nitric acid	HNO_3	70%	Riedel-de Häen
Ammonium hydroxide	NH_4OH	≥ 99.5%	Merck
Hydrochloric acid	HCl	37 %	Merck
Urea	$CO(NH_2)_2$	≥ 98 %	Merck
Carbon nanotubes	CNT	-	Sasol

A 1.2: ICP-OES calibration standards

Chemical Name	Element	Concentration	Supplier
Molybdenum	Mo	1000 ppm	PolyChem
Nickel	Ni	1000 ppm	PolyChem

A 1.3: Chemicals and gases used for catalytic testing

Chemical Name	Chemical Formula	Purity or Composition	Supplier
n-octane	C_8H_{18}	≥ 99.0 %	Merck
Air IG Zero	$O_2 + N_2$	19.0 – 22 % O_2	Afrox
Nitrogen	N_2	baseline	Afrox

A 1.4: GC liquid calibration standards

Chemical	% Purity	Supplier
1-hexene	97.5	Acros
Hexane	99	Merck
Methylcyclopentane	98	Aldrich
Heptane	99	Merck
2,4-dimethylhexane	98	Fluka
Toluene	99	Aldrich
4-methylheptane	97	Aldrich
1,7-octadiene	98	Merck
1-octene	99	Merck
Trans-4-octene	99	Merck
Trans-3-octene	> 98	Merck
Cis-2-octene	99	Merck
Trans-2-octene	99	Merck
Xylene (ortho, meta, para)	> 95	Aldrich
4-octanone	99	Aldrich
Nonane	98	Aldrich
3-octanol	99	Acros
Cyclooctane	98	Aldrich
Octane	99	Merck
Cis,cis-1,5-cyclooctadiene	98	Merck
Benzyl alcohol	97.5	Merck
3-octanone	97	Merck
2-octanone	98	Merck
Octanal	96	Merck
1-octene oxide	98	Merck
1-octanol	95	Merck
2-octanol	95	Merck
Octanoic acid	97	Merck

Ethylbenzene	96	Riedel-de Häen
Styrene	> 98	Merck

Appendix 2: Product Quantification

Calculations

In order to quantify both the organic and aqueous layers of the liquid products from the sampling cylinder, Relative Response Factors (RRF) were obtained.

Based on the assumption that the RRF of octane is one,

$$RRF = \frac{Conc.\ Octane\ \times Peak\ Area\ Compound\ A}{Conc. Compund\ A\ \times Peak\ Area\ Octane}$$

Standards were prepared using Mass/Volume concentration

A 2.1: Mass concentration prepared in standards

	Octane	**1-octene**	**Cis 2-octene**
Concentration / g.L^{-1}	1.5	2.5	2

A 2.2: **Average peak area over three replicates obtained from the GC-FID chromatogram**

	Octane	**1-octene**	**Cis 2-octene**
Peak Area	20421.0	25866.6	20883.9

A 2.3 Relative response factors (RRF)

	Octane	1-octene	Cis 2-octene
RRF	1.0	0.76	0.77

A 2.4: **Calibration curve of *n*-octane**

Calibration equations were obtained in order to quantify gaseous products using both GC-FID and GC-TCD.

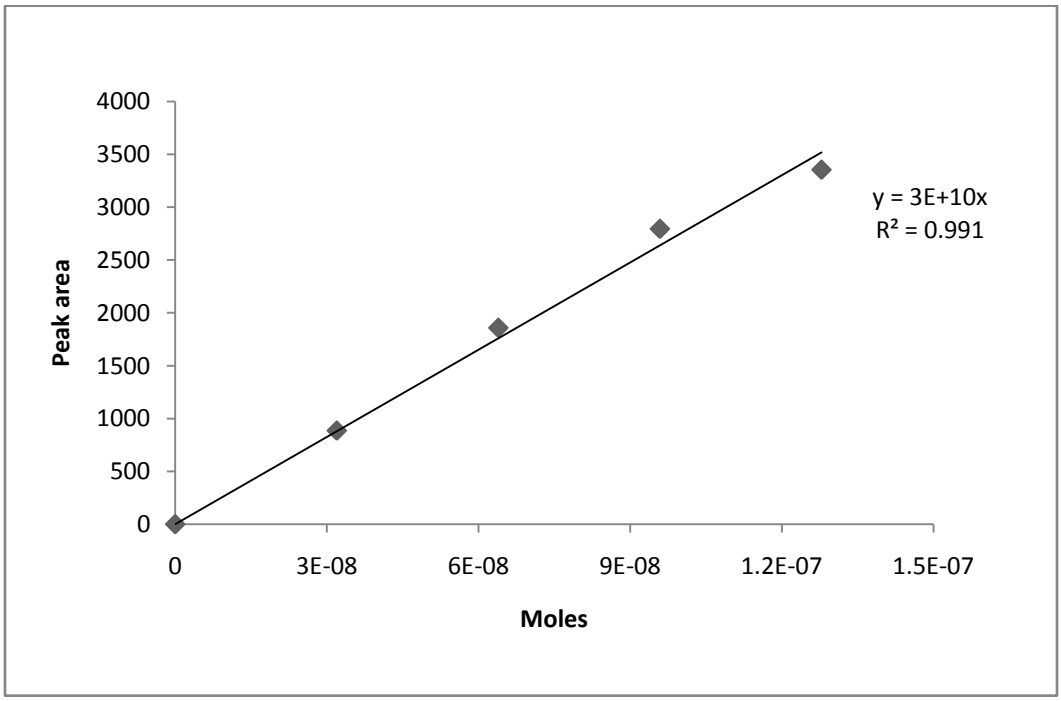

Figure A 2.1: Calibration curve of *n*-octane

A 2.5 Sample calculation

The carbon balance was performed on the basis of the number of moles of carbon entering the reactor (C_{in}) and the number of carbon atoms leaving the reactor (C_{out}). The moles of carbon entering were due to the octane feed and this was quantified using a calibrated High Performance Liquid Chromatography (HPLC) pump. C_{out} was the sum of carbon obtained from the liquid samples after subtracting the H_2O by-product (Karl Fischer titration was used to determine the water content) and the carbon obtained from the gaseous products (the moles of carbon atoms in a 500 µL gas syringe was multiplied by a factor obtained from the total gaseous product volume, measured using a Gas-Flow Meter, to 500 µL).

Example:

At a specific time, 0.124 moles of octane entered the reactor and only 0.110 moles of octane exited, together with 0.00600 moles of 1-octene and 0.0500 of CO_2. The volume of catalyst used was 1 mL and the total flow of gaseous feed was 60 $mL.min^{-1}$.

Required to calculate:

(a) Gas hourly space velocity GHSV (h^{-1})
(b) Carbon balance
(c) % Conversion of octane
(d) % Selectivity to 1-octene
(e) % Yield of 1-octene

$$(a)\ GHSV(h^{-1}) = \frac{Total\ flow\ of\ gaseous\ reactants\ (mL.h^{-1})}{Volume\ of\ catalyst\ (mL)}$$

$$= \frac{60\ mL.min^{-1}\ \times\ 60\ min}{1\ mL\ \times\ 1\ h}$$

$$= 3600\ h^{-1}$$

(b) $Carbon\ balance = \frac{Total\ C_{out}}{Total\ C_{in}} \times 100$

$$= \frac{(8 \times 0.11) + (8 \times 0.006) + (1 \times 0.05)}{8 \times 0.124} \times 100$$

$$= 98.7\%$$

$(c)\%\ Conversion\ of\ octane = \frac{C_{in} - C_{out}}{C_{in}} \times 100$

$$= \frac{(8 \times 0.124) - (8 \times 0.11)}{8 \times 0.124} \times 100$$

$$= 11.3\ \%$$

(d) $\%\ Selectivity\ to\ 1-octene = \frac{C_{1-octene}}{C_{in} - C_{out}} \times 100$

$$= \frac{8 \times 0.006}{(8 \times 0.124) - (8 \times 0.11)} \times 100$$

$$= 42.8\ \%$$

$(e)\ \%\ Yield\ to\ 1-octene = \frac{\%\ Selectivity \times \%\ Conversion}{100}$

$$= \frac{42.8 \times 11.3}{100}$$

$$= 4.84\ \%$$

A 2.6 GC temperature programs

GC-MS:

Injector: 250°C

1:70 split

1.0 mL min^{-1} flow rate

Initial temperature: 50°C, hold time 15 min

Ramp 1: 10°C min^{-1} to 120°C, hold time 10 min

Ramp 2: 20°C min^{-1} to 200°C, hold time 13 min

GC-TCD:

Injector: 250°C

1:70 split

2.0 mL min^{-1} flow rate

Initial temperature: 36°C, hold time 1.5 min

Ramp 1: 25°C min^{-1} to 65°C, hold time 3 min

GC-FID:

Injector: 220°C

1:20 split

1.86 mL min^{-1} flow rate

Initial temperature: 40°C, hold time 15 min

Ramp 1: 10°C min^{-1} to 120°C, hold time 2 min

Ramp 2: 20°C min^{-1} to 200°C, hold time 1 min

Appendix 3: IR spectra

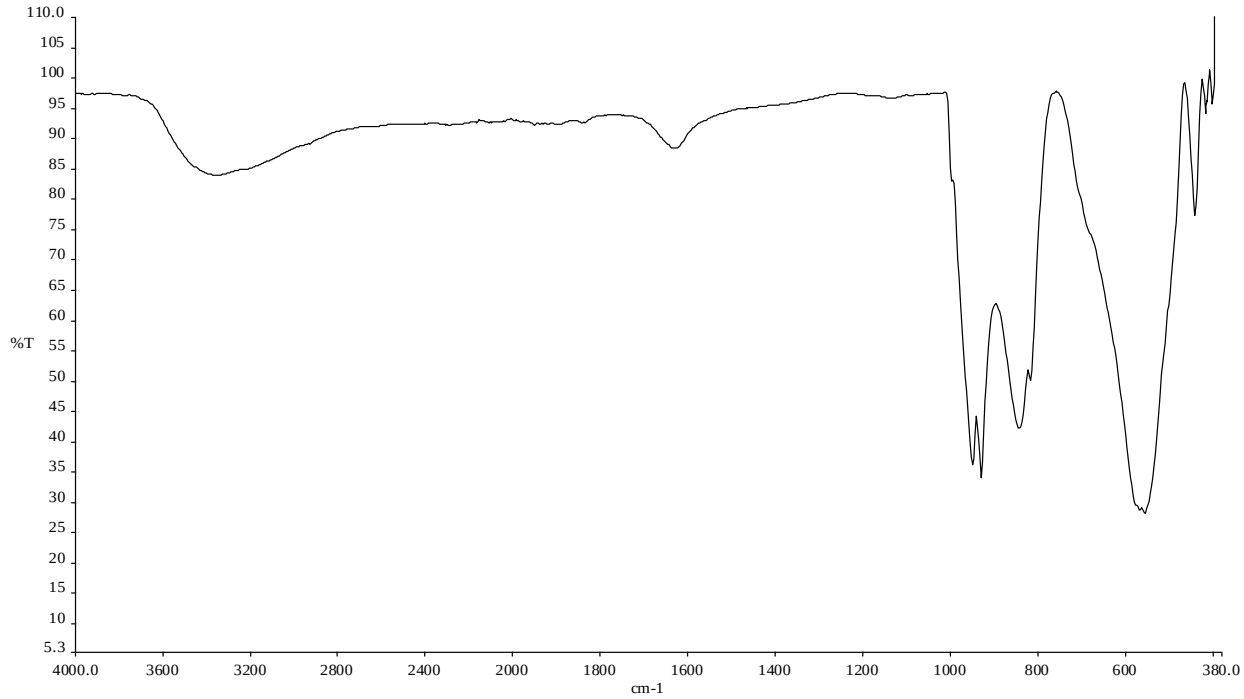

Figure A 3.1: IR spectrum of NM-B

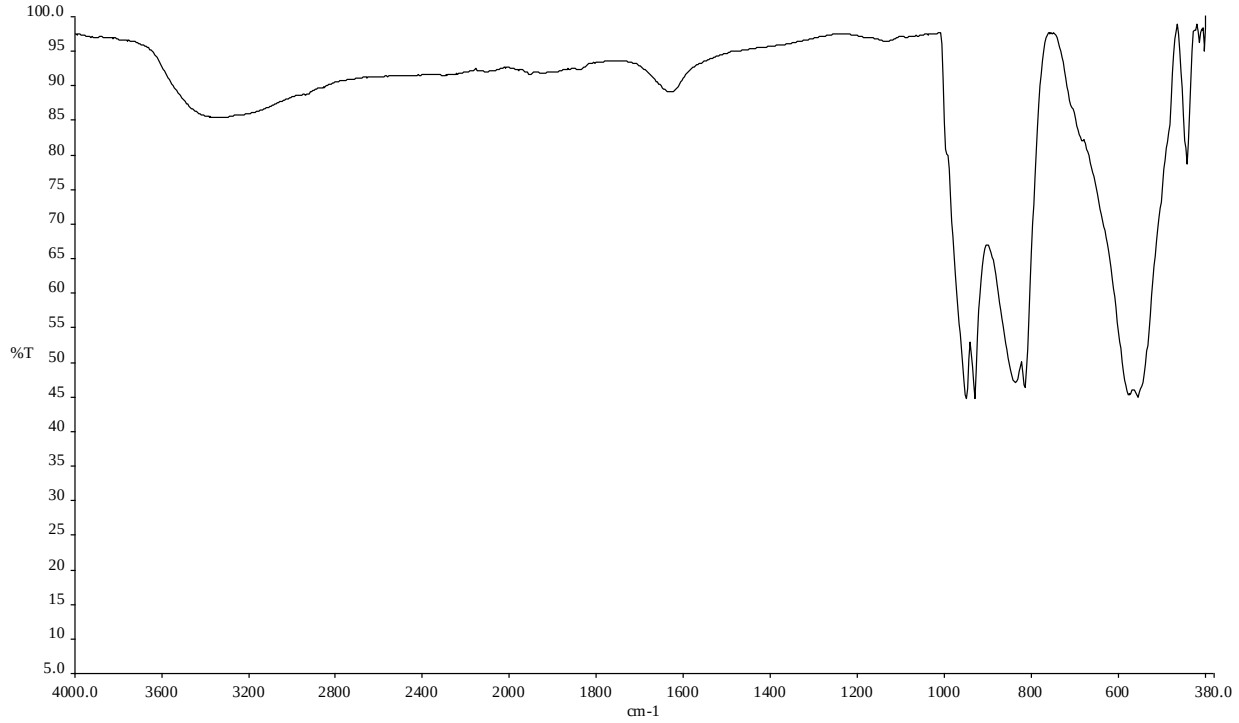

Figure A 3.1: IR spectrum of NM-C